A Programmable Optical Angle Clamp For Rotary Molecular Motors

TEUTA PILIZOTA

A thesis submitted in partial fulfillment of
the requirements for the degree of
Doctor of Philosophy at the University of Oxford

Wolfson College
University of Oxford
Trinity Term 2006

A PROGRAMMABLE OPTICAL ANGLE CLAMP FOR ROTARY MOLECULAR MOTORS

Teuta Pilizota, The Wolfson College

Thesis submitted for the degree of Doctor of Philosophy
at the Univeristy of Oxford, 2006

ABSTRACT

This thesis describes the design of a programmable optical 'angle clamp', a novel technique for the study of rotary molecular motors. The 'angle clamp' is based on a home-made laser trap and uses a bead-pair as a novel handle to apply torque to the motor proteins. The resolution achieved with this system is: 1° angular resolution, and 20 μs temporal resolution. The bead-pair was controlled using a feedback algorithm with a precision of up to 2° and a bandwidth of up to 1.6 kHz.

The 'angle clamp' was applied to two rotary molecular motors of interest: F_1-ATPase and the bacterial flagellar motor. Preliminary data showing angular and speed control of the bacterial flagellar motor are presented. *Escherichia coli* F_1-ATPase purification and a rotation assay was developed based on the protocols learned and obtained from collaborators at Osaka University, Japan. Yeast mitochondrial F_1-ATPase was provided by the members of The Chicago Medical School, USA for collaborative work. The rotation of yeast mitochondrial F_1-ATPase was observed for the first time. The control of the angle of the *Escherichia coli* as well as the yeast mitochondrial F_1-ATPase was achieved and is presented. The encountered problems with motor's attachment to the surface are explained and discussed.

The temporal and angular resolution of the system presented in this thesis was used by other members of Dr. R.M. Berry's group for detection of small polystyrene beads attached to the bacterial flagellar motor. This allowed insight into the behavior of the chimeric sodium driven *Escherichia coli* flagellar motor in the low-load regime as well as observation of steps in the motor rotation in the low-load and low-speed regime. It has also allowed investigation of the switching behavior of a wild type *Escherichia coli* flagellar motor.

ACKNOWLEDGEMENTS

The biggest thank you goes to my supervisor, Dr. Richard Berry. The last four years have been both challenging and rewarding. For your support through out those years, your enthusiasm and love for science, your excellent scientific insight, your patience during discussions, you willingness to consider even the craziest ideas, and for your guidance through all the stages of my research: thank you. You have without a doubt taught me a lot.

To all the current and former members of my lab: Thomas Bilyard, Mark Leake, Chien-Jung Lo, Yoshiyuki Sowa, Jennifer Chandler, Tania Saxl, Fan Bai, Stuart Reid, Richard Branch, Wei-Ming Ho and Alex Rowe. Thank you for the interesting scientific discussions, for all I learned about different cultures, and foremost for the great deal of support and understanding I received. Special thanks goes to Thomas Bilyard for being on the F_1 team.

I am very grateful to Jelena Baranovic and Maja Petkovic, for helping me push forward the F_1 work during a wonderful and very hard working three months, and to Prof. Judy Armitage and members of her lab for having Maja, Jelena and me in their lab and helping us with the biochemistry. For the help with biochemistry and for welcoming me in their lab I also thank Prof. Masamitsu Futai, Hiroyuki Hosokawa and Mayumi Nakanishi.

To Dr. Sonia Contera and Dr. Maurits Deplanque I thank for their outstanding support, help and advice. And to Dr. Russell Goodman and Tania Saxl for proof reading my thesis.

To the staff of the Main Workshop, Research Workshop and Central Electronics Workshop for manufacturing different parts of the setup, as well as for helping me manufacture some of the parts on my own. To Janet Andrews for her patient help with all the official procedures, paper work matters and any questions that I have come to ask her during the years.

For being the most fantastic friends one could ever whish for I thank Branimir Lukic, Mario Juric, Shelley Cook, Maoko Naganuma, Elaine Snell and Julian Summers. And my mum, dad and grandmother I thank for always being there when I needed them most.

In the end I whish to thank Prof. John Ryan and his IRC for their support.

To my parents

CONTENTS

Chapter 1

INTRODUCION

1.1 Overview

Ushered by the technological developments of recent years, sub-disciplines of biology studying basic structures of living systems have made and continue to make great progress. The fields of bioinformatics, genetics, biochemistry, developmental biology and biophysics all have a role in exciting new research that offers more and more information on living systems.

Specifically, in the field of single molecule biophysics, optical and mechanical probes, sensitive enough to measure forces with piconewton precision and nanometer accuracy, enable individual studies of molecules previously well characterized by bulk experiments.

Initial questions that drove scientific research on the single molecule level include; how do certain proteins move, how do they change their conformation, how do they generate force or respond to it?

This thesis aims to answer similar questions for two rotary molecular motors: the bacterial flagellar motor and F_1F_o-ATPase. Thus, a system designed to probe the energy profiles of rotary molecular motors was constructed and is described. Its application to the bacterial flagellar motor and F_1-ATPase is subsequently presented and results discussed. Further ideas and an outline of future research is given at the very end of the thesis.

1.2 Molecular Motors

A motor is a device that converts any given form of energy into mechanical energy. Biological molecular motors are complexes that transform chemical energy directly into mechanical work thereby ensuring suitable energy storage, force production and directional motion on both microscopic and macroscopic scales.

Macroscopic motors as well as their surrounding are made of a large number of small molecules. Although these molecules move according to Newton's laws, on time scales relevant for operation of macroscopic motors, information on their deterministic trajectories is lost, and their behaviour can be described statistically. The most likely configurations of the system are very similar to each other, and on macroscopic scales, differences between these configurations, i.e. thermodynamic fluctuations, are negligible. As a result, joint behaviour of large number of molecules that the macroscopic motor and its surrounding are made of, can be described through the thermodynamical properties and laws of thermodynamics.

The number of molecules in a microscopic motor is still large, but microscopic motors are so small that they do 'feel' thermodynamic fluctuations. These fluctuations are an essential component of the molecular motor and must be taken into account. To describe the way a molecular motor works it is useful to define the so-called bath and system variables [1]. Bath variables are taken into account implicitly; they are extra degrees of freedom in the protein and in the solvent, which on experimental time scale fluctuate fast enough to be in equilibrium. System variables define an n-dimensional space, and each point in that space has a corresponding free energy value. A potential energy surface thus defined, spanning an n-dimensional state space in which the motor moves, arises primarily from three sources; *(1)* interactions within the motor, as well as interactions with the track along which the motor moves (if one is present), *(2)* interactions with the molecules that serve as fuel (source of chemical energy), and *(3)* interactions with the solvent. To illustrate the point clearly, a case in which a motor can be described with one chemical and one mechanical system variable is shown in Figure 1.1 [1].

The description of a molecular motor moving along an energy surface is usually mechanical and stochastic, kinetic, or a combination of the two. A mechanical picture is illustrated in Figure 1.1 A. Since the motor is microscopic its motion is

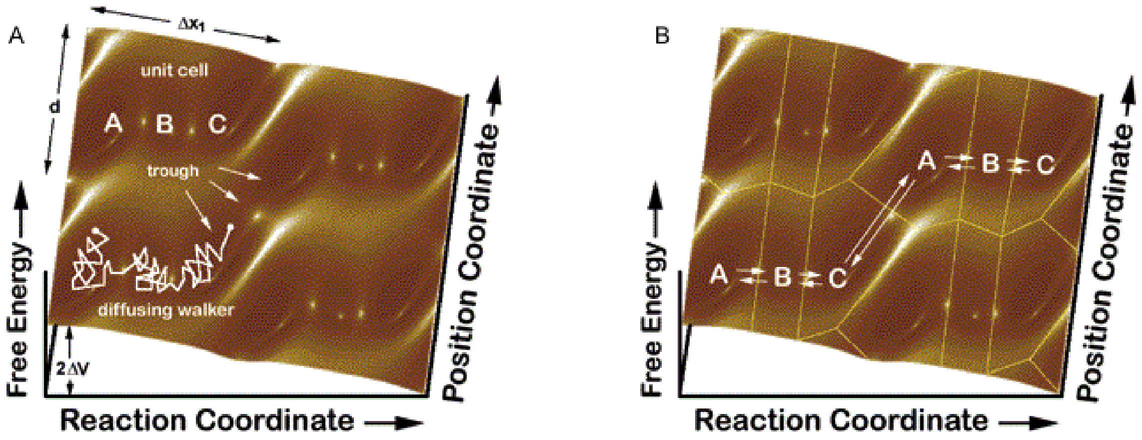

Figure 1.1: (A) Minimal potential energy surface for a molecular motor. The surface is periodic in both reaction and position coordinate, and has three local minima (A, B, C). These are connected by low-energy passes and the surface is tilted along the chemical axis, representing the free energy of the reaction. The long trough in the centre couples chemical energy to mechanical motion. The system point moves by random walk over this surface. (B) Correspondence between the potential energy surface and kinetic mechanism of the motor. The regions around the local minima represent the intermediate species. Diffusion between minima is equivalent to chemical transitions, which can be described by kinetic rate constants. Figure and the legend are taken from reference [1].

not given as a deterministic trajectory defined by the energy surface but it is better described by the Smoluchowski equation as the diffusion of the system along the potential energy surface.

The Smoluchovski equation for probability distribution $w(x_1, x_2, t)$ where x_1 and x_2 represent chemical and mechanical coordinates is given as

$$\frac{\partial w}{\partial t} + [\sum_{i=1}^{2}(-\frac{k_B \cdot T}{\gamma_i}\frac{\partial^2}{\partial x_i^2} + \frac{1}{\gamma_i}\frac{\partial}{\partial x_i} f_i)]w = 0 \tag{1.1}$$

where i is the number of system variables (one mechanical and one chemical in Figure 1.1), f_i are external mechanical forces acting on the motor, γ_i are friction coefficients, k_B is Boltzmann's constant and T is the temperature [1].

The kinetic picture is illustrated in Figure 1.1 B. Minima in the energy surface are recognized as intermediate states (A, B, C). Kinetic rate constants give statistical rate at which transitions will occur between the minima. They will depend on external forces acting on the motor, f_i, and on the spatial position of the motor. The mechanical motions in this description are thermally excited. The Smoluchowski equation becomes a set of first-order or pseudo-first-order rate equations governing the populations of the discrete states.

$$\frac{\partial \rho}{\partial t} = \mathbf{K}\gamma \tag{1.2}$$

where $\rho = (\rho_1, \rho_2, ..., \rho_n)$ is a vector of populations and $\mathbf{K}$ is a matrix of rate constants or step transition probabilities:

$$\mathbf{K} = \begin{pmatrix} k_{11} & k_{12} & . & . & . & k_{1n} \\ k_{21} & k_{22} & . & . & . & k_{2n} \\ . & . & . & & & \\ . & . & . & & & \\ . & . & . & & & \\ k_{n1} & k_{n2} & . & . & . & k_{nn} \end{pmatrix} \tag{1.3}$$

Both descriptions are in fact two different forms of an equation that describes a Markov processes [1]. I have started this chapter by introducing them first since they, despite great variety in geometry of different molecular motors, represent a general framework for understanding them.

In addition, establishing this frame work facilitates the understanding of the motivation that lies behind building the system presented in this thesis.

The description given above includes two commonly used models for explaining force or torque generation by molecular motors, ‘power stroke’ and ‘thermal ratchet’. In the ‘power stroke’ model the free energy supplied either by influx of ions or by the ATP molecule is directly coupled to the torque/force-generating state. Thus thermal fluctuations are not necessary for torque or force generation. ‘Thermal ratchet’ model on the other hand uses the free energy stored in the flux of ions or ATP molecule to bias thermal fluctuations in a certain direction. Models for different motors in which the difference between the two is not as clear are also possible and were proposed [2]. If one looks more closely at the different geometries of molecular motors, their separation into two groups, depending on the nature of movement they undergo, is obvious; linear and rotary. Both types of mechanical movement require energy input.

There are two sources of free energy used by molecular motors: (1) A protonmotive (*pmf*) or sodium-motive force (*smf*), i.e. electrical potential and concentration gradient, storing ∼6 kT per ion at ∼100 mV *pmf.* (2) An ATP molecule, each storing ∼18 kT.

Members of the myosin, dynein and kinesin families represent linear molecular motors which move in a specific direction along asymmetric actin filaments or microtubules.

In the bacterial flagellar motor (bfm), F_1F_o-ATPase (F_1F_o) and V-ATPase, steps of the mechanical cycle are represented by the circular motion of certain units around a static part of the motor.

It is detailed information about the energy profile (see the imaginery motor given in Figure 1.1) of the two rotary molecular motors of interest (the bfm and primarily F_1-ATPase) that one should gain with the system presented in this thesis. Below I give a brief introduction to linear motors and a more extensive one of the two rotary molecular motors, F_1F_o and the bfm. At the very end I briefly mention other molecular motors, for example DNA related motors. My aim is to create a broad picture of the field of molecular motors (especially rotary motors), starting with the general framework above, and finishing by placing my own research into that picture. I believe that both the reader and myself gain a full understanding of the place of my research in the field, with an introduction structured in this way.

Therefore, for each of the motors introduced, I explain what they are and what their role and importance is, followed by a description of their structure. In my view the main purpose of structural information is to help determine the reaction and position coordinates given in Figure 1.1. I then focus on experiments that unravel motors' function. These experiments give information about relevant intermediate states (A, B, C in Figure 1.1) and chemical rate constants (Figure 1.1 B and Equations 1.2 and 1.3) or external forces and friction coeficients, f_i and γ_i in Equation 1.1. For linear motors, I reference the most important experiments and give a current model of the motors' chemomechanical cycle. I describe a few of these experiments, as an example of the kind of work my system should enable us to do on rotary molecular motors. When introducing F_1F_o and the bfm I describe the experiments more extensively. This extensive description will help me to outline current unanswered questions and explain how the system, built as part of my D.Phil. research, does and will help in answering them.

1.2.1 Linear molecular motors

Myosin

Myosins are molecular motor proteins that use the energy from ATP to generate force for direct movement along actin filaments [3]. Each member of the myosin family will move exclusively towards the plus or minus end of actin. Some myosins are long-range transport motors, and spend a large fraction of the ATP hydrolysis cycle bound to the actin filament (high-duty ratio), while others have a low duty-ratio and show cooperativity (some myosins move along actin filament as a result of involvment of multiple units, i.e. myosin heads). There are more than 20 different myosin classes, with varied functional roles. These include: contributing to cell motility and adhesion, organelle/cellular component transport, maintenance of actin-rich extensions and formation of non-muscle contractile structures, membrane trafficking and signal transduction [3]. Myosins are composed of one or two heavy chains and one or more light chains. The heavy chains consist of several domains and sub-domains: (i) The conserved N-terminal 'head' domain contains binding sites for ATP and actin, (ii) a short region ('converter' domain) joining the head and the neck is believed to be responsible for producing the force required for movement, (iii) a neck domain with light chain binding regions, (iv) the C-terminal globular 'tail' believed to be involved in binding cargo and targeting the myosin to its proper location in the cell [3].

Based on experimental results several models for processive movement of myosin V emerge as given in a recent review [4]. For a start, a two headed structure is necessary [5, 6, 7, 8].(i) At saturating [ATP] and low load the molecule dwells mostly with two heads strongly bound to actin and ADP bound to the two heads [5, 6, 9, 10]. (ii) ADP release is slightly accelerated in the trailing head and strongly reduced in the leading head, due to intramolecular strain. (iii) The leading head binds ATP resulting in detachment of that head [9, 10, 11, 12]. (iv) The leading head re-binds strongly to actin before the trailing head releases ADP [10, 11]. Alternatively, it is possible that (i') the molecule dwells with the strongly bound rear head with ADP, and weakly bound leading head with ADP.P_i before continuing with the step (ii) [10, 11], or (ii') the trailing head releases ADP while the leading head is still weakly bound before going to the step (iii) [10, 11]. Of the experimental results referenced above, the level of detail obtained with an optical-tweezers-based transducer is of special interest [9, 13]. The system described in this thesis was designed and constructed with similar goals in mind for two rotary molecular motors, bfm and F_1-ATPase. The optical-tweezers-based transducer used in experiments [9, 13] consists of two optical tweezers, each trapping a polystyrene bead attached to either ends of actin filament. The filament was positioned over a third bead, attached to the surface and covered with myosin V. The movement of the two actin attached beads was monitored with two quadrant photo diodes and sudden changes in the stiffness of the system, corresponding to myosin V binding to actin, were identified by the changes in the Brownian noise. This revealed that the working stroke of a single-headed, as well as a double-headed, myosin V happens in two substeps, ∼16 nm and ∼5 nm, of which the first substep is [ATP] independent while the second substep became shorter at higher [ATP] [9]. By applying a sinusoidal motion to one of the beads attached to the actin, the existence of prefered myosin binding positions was identified, each separated 36 nm from the other. Thus it was proposed that the single 36 nm step of a double-headed myosin V is a combination of a 25 nm long working stroke and a 11 nm thermally driven diffusive movement [9]. A later experiment with the same system, further developed, identified the load dependant steps of the working stroke [13].

Kinesin

Kinesins are motor proteins that use the energy from ATP to transport cargoes along microtubule rails [14]. Microtubules are well organized in cells and have a polarity with a fast-growing (plus) end and a slow-growing (minus) end. Different members of the kinesin family will move either towards the plus or minus end, and will show either proccessivity (high-duty ratio) or cooperativity (low-duty ratio). The functional roles of kinesin are as broad as with myosin. The entire family is divided into 14 classes, members of which transport different kinds of cargo: organelles and macromolecules in the cell, mitochondria, lysosomes, endotic vesicles, tubulin oligomers, intermediate filament proteins, and mRNA complexes. They also have a role in cytoplasmic viral transport [14]. Kinesin typically consists of two heavy chains (KHCs) and light chains (KLCs). ‘Conventional kinesin’ (the kinesin discovered first), has a rod-like structure composed of two heads (10 nm in diameter), a stalk, and a fan-like end with a total length of 80 nm. Kinesins are distinguished based on the position of the motor domain (head) into N-terminal, C-terminal, and middle domain type. The C-terminal type kinesins studied thus far are minus-end motors, the N-terminal types are plus-end motors [14].

Kinesin's function has been extensively studied. As with myosin, I will mention only a few experiments, in which the systems used and the knowledge aquired illustrates well the kind of detailed information my system should yield for rotary molecular motors [15, 16, 17]. A 1-D [16] and a 2-D [15, 17] optical force clamp was used to apply force to kinesin molecules in different directions. The motor turnover rate, k_{cat}, and substrate binding constant, k_b, were monitored in responce to the applied force and its direction. Sideways loads had an asymmetric effect on k_{cat} [15], backwards loads reduced both k_{cat} and k_b [15, 16], while forward loads had no significant effect on kinesin [15]. These findings indicate a strongly load dependent transition (power stroke) early in the cycle and a further smaller motion later in the cycle. Since the effect of sideways loads was comparatively weak an (essentially) single-stroke mechanism is still proposed by the authors as the best explanation for the available data [15]. A recent review [18] combines many other experimental results (mostly done on double headed processive Kif5b kinesin) into a model as follows: (i) ATP binds to the trailing head bound to microtubule [19, 20]. The leading head, detached from microtubule, has ADP bound. (ii) The leading head attaches to microtubule and ADP is released [19, 20, 21, 22, 23]. Upon ADP release an 8 nm kinesin step is completed [24]. ATP binding to the leading head is strain inhibited [25, 26, 27]. (iii) Hydrolysis occurs in the trailing head and P_i is released [21, 26]. (iv) A pull by the leading head enables detachment of ADP bound trailing head [28, 23]. Trailing head crosses over the leading head and becomes the new leading head ready to repeat the cycle [28, 29, 30, 24].

Dynein

Dyneins are large motor proteins that carry their cargo towards the minus end of microtubules [31]. Unlike kinesin dynein is not restricted to walking along the same microtubule protofilament [32, 33, 34]. As well as kinesins and myosins, dyneins are involved in wide variety of cellular functions: mitosis, vesicular transport, the assembly and motility of cilia and flagella, and the generation of left-right asymmetry in the developing embryo [31]. Dyneins are composed of one to three heavy chains (HC). Each heavy chain consists of a C-terminal head domain, a stalk composed of two elongated flexible structures and a N-terminal tail domain. The head is the motor domain, the stalk binds to the microtubule and the tail to specific cargo. Dyneins built from two or more HCs also contain two intermediate chains (IC), involved in the binding of specific cargo. They are located at the base of soluble dynein and interact both with the HCs and also with three different classes of light chains (LC). Dyneins are separated into two major classes: cytoplasmic dynein (involved in different cellular processes) and axenomal (producing the bending motions propagating along cilia and flagella). While more than one member of kinesin and myosin families, with their diverse cellular functions, will be present in the cell*, dynein in the cytoplasm has only one HC isoform (a few more are present in cilia and flagella dyneins) and the functional variety comes from different accessory proteins. Expression and function of these ‘helper’ proteins is achieved through a set of different mechanisms [31]. Compared to kinesins and myosins less is known about the way dynein works. Experiments that help build our understanding of the energy potential along which this motor moves and the relevant mechanical and chemical coordinates are summarised in a model from a recent review [35]: (i) Dynein without nucleotide is bound to the microtubule [36, 37]. (ii) Upon ATP binding to the motor head, dynein detaches from the microtubule [36, 37, 38, 39, 40, 41, 42]. (iii) ATP is

---

*each coded by different gene(s)

hydrolysed and dynein changes its conformation in preparation for the power stroke. (iv) The dynein stalk binds to the microtubule and the microtubule is pushed forward by conformational changes in the head ring, and as a result ADP and P_i are released [36, 37, 39, 43, 44, 45, 46, 47].

RNA and DNA Polymerases

Polymerases perform directional mechanical work against disipative forces during the reaction of polymerization. The polymerization of nucleotide triphospates (NTPs) is a process by which DNA polymerases (DNAP) synthesize exact copies of genomic DNA during cell division, and the RNA polymerase (RNAP) initiates the transcription process, thus providing expression of genetic information encoded in DNA. RNAP uses double-stranded DNA as a template (non-polar and in principle permits motion in both directions), where the direction of movement is determined by the orientation of the promoter, while the DNAP direction of movement is determined by polarity of the replication fork. Individual stepping events correspond to the distance between individual base pairs (∼0.34 nm [48]). The velocity of the motor is in some cases comparable to linear molecular motors and in some cases slower. The most significant difference between other molecular motors and polymerases are the larger forces generated by the later (force and velocity measurements done on polymerases are similar to the kind of experiments the system described in this thesis is designed for, for example [49, 50, 51]) The exact significance of such high forces is not understood. Most probably the high force generated enables the polymerase to drive off the ‘road blocks’ (different DNA bound proteins) in the case of RNAP, and in the case of DNAP it could promote efficient duplex unwinding [48]. Chemical energy is provided by the polymerase reaction, i.e. by all four nucleotide triphosphates (NTPs), where each polymerization step is directly coupled to forward motion of the enzyme.

Helicases

Helicases are molecular motor proteins that use the energy of NTP hydrolysis to unidirectionally translocate along a ploymeric nucleic acid (NA) and unwind the complementary strand of the double stranded NA (they can also destabilize the secondary structure of RNA, remove NA associated proteins, and thread NA through various pores). Helicase activity involves NTP binding, hydrolysis and product release, which induces conformational changes in the helicase NA binding site. These conformational changes will change helicase affinity for the NA or drive it to perform a power stroke [52]. The helicase NTPase activity is elevated in the presence of NA.

1.2.2 Rotary molecular motors

F_1F_o-ATPase (Figure 1.2)

F_1F_o is an enzyme that generates roughly 2.0 million kg of ATP from ADP and P_i in the 75-year lifespan of a typical 70 kg human [53]. The ATP molecule is the energy 'currency' of living organisms. The transition to ADP, with one less phosphate bound, and the free phosphate, releases the energy needed for many cellular processes), and it is therefore present in large amounts. In 1997 it was directly proven that the enzyme undergoes rotary motion during ATP hydrolysis [54]. At ~20 nm in size, it is one of the most evolutionary conserved enzymes [55, 56, 57]. It is therefore no wonder that it is considered one of the most exciting and remarkable works of nature.

STRUCTURE

F_1F_o-ATPase has a very similar overall structure whatever the source; prokaryotes, chloroplasts or mitochondria. The part of the enzyme located in the membrane is usually referred to as F_o and the cytoplasmic part is usually referred to as F_1 (Fig-

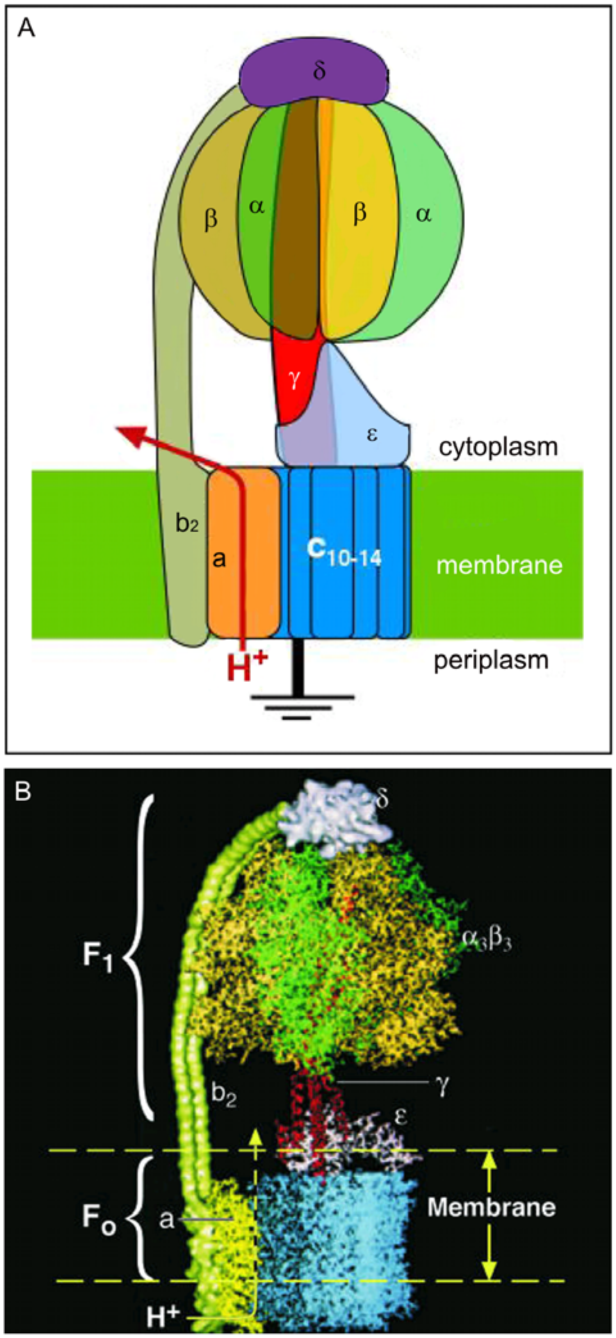

Figure 1.2: (A) Schematic showing *E. coli* F_1F_o-ATPase. (B) Structure of the *E. coli* F_1F_o ATPase. Figure and the legend are taken from references [58] and [59].

ure 1.2 A and B). Synthesis and hydrolysis occur in F_1 (Figure 1.2) which in the prokaryotes (simplest ATP synthase) consists of $\alpha_3\beta_3\gamma\delta\epsilon$ subunits. $\alpha_3\beta_3\gamma$ subunits represent the central part of the enzyme, with ATP synthesis and hydrolysis occurring in the $\alpha_3\beta_3$ hexamer, while the γ subunit rotates, either driving the reaction or driven by it.

F_o, consisting of ab_2c_{10-14} subunits, uses a proton gradient to rotate c subunits, thus supplying necessary energy for γ subunit rotation. While on a single molecule level most of the work has been done on prokaryotic ATP synthase, crystal structures are obtained primarily on the enzyme from bovine heart mitochondria. In 1994, Walker and Leslie obtained a crystal structure of bovine heart mitochondria F_1, with a resolution of 2.8 Å and with a crystal grown in the presence of 250 μM AMP-PNP (an analog of ATP), and 250 μM ADP (protein data bank (PDB) code 1BMF) [60]. The structure consists of three α subunits, three β subunits, and a γ subunit. The non-catalytic sites of all three α subunits have AMP-PNP and Mg^{2+} bound, while one β subunit has ADP and Mg^{2+} bound (referred to as βDP), one AMP-PNP and Mg^{2+} (βTP) and one subunit is empty (βE). This native structure most likely represents the Mg-ADP inhibited form, i.e. the state right after ATP was bound to one of the β subunits, and is inhibited by the failure of Mg-ADP release from another of the catalytic sites [61]. Several more crystal structures were obtained subsequently, of which only a few significantly differ in terms of γ subunit orientation or the number and location of nucleotides, compared to the native structure. One of them, bovine mitochondrial F_1 inhibited by Dicyclohexylcarbodiimide (DCCD), obtained in 2000 with a resolution of 2.40 Å (PDB code 1E79) has ϵ and δ subunits as well as the γ subunit, forming a foot that interacts with the membrane part of the protein (ϵ and δ in mitochondrial F_1 are equivalent of ϵ in bacterial, to avoid confusion in Figure 1.3 the two are compared) [62]. In the other bovine F_1 structure, obtained in 2001 with a resolution of 2.00 Å, the γ subunit orientation is shifted by 15° compared to the native structure (PDB code is 1H8E) [63]. The crystal was formed in the presence of 1 mM $AlCl_3$, 5 mM NaFS and 660 μM ADP, and has ADP, Mg^{2+} and glycerol bound to all α subunits; ADP, Mg and SO_4^{2-} to the βE subunit; ADP, Mg^{2+} and AlF_4^- to βDP and ADP, Mg^{2+}, AlF_4^- and glycerol to the βTP subunit. It is speculated that the structure represents the post-hydrolysis, pre-product release step since the βE subunit now binds ADP and sulphate (mimicking P_i) and adopts a ‘half-closed’ conformation. This interpretation of the 2001 structure implies that the native structure is actually the ATP waiting state. However, in 2004 a BeF_3^- inhibited structure of bovine mitochondrial F_1 was obtained with a resolution of 2.00 Å (PDB code 1W0J) [64]. This BeF_3^- inhibited structure is very similar to the native one, despite the fact that in terms of crystallization conditions it is very similar to the AlF_4^- inhibited one. Why is the βE subunit empty in the BeF_3^- inhibited structure occupied in the AlF_4^- structure is not clear, but it suggests that the small differences could be due to the crystal packing forces. One thus has to be very careful when drawing conclusions about the working mechanism of an intact protein from structures. It is worth noting that four independent inhibition sites of bovine mitochondrial F_1 have been identified while obtaining different crystal structures: the catalytic sites [60, 65, 62, 66, 63], the aurovertin B-binding site [67], the efrapeptin-binding site [68] and the site to which natural inhibitor protein IF_1 binds [69]. Understanding of these inhibitors of bovine mitochondrial F_1 is of importance for the treatment of several disorders linked to the regulation of the ATP synthase, including some cancers [70]. In 1997, the nucleotide-free structure of the $\alpha_3\beta_3$ hexamer from Thermophilic *Bacillus* PS3 was obtained with a resolution of 3.20 Å, showing that the α and β subunits are essentially the same as in the bovine crystals [71]. In this structure only one β subunit was filled with the nucleotide and the γ subunit was twisted counterclockwise compared to the mitochondrial structures suggesting that this structure, rather then the 1994 native structure, represents the ATP waiting step. The structure of *E. coli* F_1 was probed mostly with NMR studies [72] and electron microscopy [73, 72, 74, 75] and the arrangement of the subunits as shown in Figure 1.3 B was thus determined.

In 2005, a crystal structure of the F_o c-ring from Na^+-ATPase from *Ilyobacter*

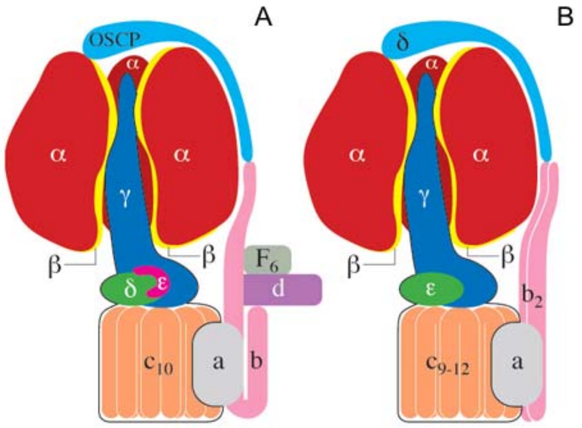

Figure 1.3: (A) Schematic showing the structure of mitochondrial F_1F_o-ATPase. (B) Schematic showing the structure of *E. coli* F_1F_o-ATPase. δ and ϵ subunits in the mitochondrial enzyme are equivalent to the ϵ subunit of the *E. coli* enzyme. The δ subunit of the *E.coli* enzyme is equivalent of the oligomycin sensitivity conferring protein (OSCP) in mitochondrial enzyme. Also, in mitochondria the stator is built of one b subunit and has F_6 and d subunits, while the *E. coli* enzyme has only a b subunit dimer. This figure is taken from the following webpage http://www.rpi.edu/dept/bcbp/molbiochem/MBWeb/mb1/part2/f1fo.htm, where it is stated that it was provided by Prof. J. E. Walker

tartaricus was determined with 2.40 Å resolution (PDB code 1YCE) [76]. Each of the 11 c subunits showed a cylindrical, hourglass shape and had Na^+ bound in the middle and closer to the outer surface of the subunit (the crystal was formed in the presence of 100 mM sodium acetate, which promotes binding of Na^+). The c-ring complex is ∼7 nm in height with an outer ring diameter of ∼4 nm in the middle and ∼5 nm at the top and the bottom. Towards the periplasmic surface from the binding site, a cavity was observed. It is speculated that the Tyr70 side chain could relocate to this cavity and allow ion binding and unbinding from the a subunit.

Structures of the following other $F_1F\ _o$-ATPase subunits are known: the NMR structure of bovine mitochondrial stator unit OSCP (PDB code 2BO5) [77], the NMR structure of F_6 subunit from bovine mitochondrial F_1 (PDB code 1VZS) [78], a crystal structure of bovine mitochondrial peripheral stalk consisting of subunits b, d and F_6 (PDB code 2CLY) [79], the NMR structure of *E.coli* δ subunit (PDB code 1ABV) [80], the NMR structure of the membrane spanning part of the b subunit of *E.coli* F_1 (PDB code 1B9U) [81], the crystal structure of the 'dimerisation domain' of b subunit of *E.coli* F_1 (PDB code 1L2P) [82]. These structures, as well as a recent electron cryomicroscopy structure of bovine heart mitochondrial F_1 [83] and biochemical studies which probed different features of F_1F_o-ATPase structure (for example [84]), contribute to our current understanding of position and orientation of certain subunits as shown in Figure 1.3 A and B.

FUNCTION

F_1 hydrolysis

Although indirect evidence of rotation of some F_1-ATPase subunits had been obtained before, rotation was observed directly in 1997 [54], followed by a series of absolutely beautiful single molecule experiments, from which a great deal was learned about ATP hydrolysis and of which I give a short account below. In a 1997 experiment, a genetically engineered F_1, with His-tags on β subunits and a cys mutation on the γ subunit, was attached to coverslip surface, and a fluorescently labelled actin filament was attached to the γ subunit through a biotin-streptavidin-BSA link. Direct rotation was observed under an optical microscope. A later experiment done in a similar fashion had a fluorescent actin filament attached to the ϵ subunit. Again, rotation was observed and was taken as a direct proof that the ϵ subunit as well as γ forms the F_1 rotor [85]. More conclusive proof came in 2005 in an experiment in which rotation of the ϵ subunit was observed in an F_1F_o system incorporated into liposomes. Rotation of the ϵ subunit (labelled with a fluorescent donor) was observed relative to the b subunit (labelled with a fluorescent acceptor) by fluorescence resonance energy transfer (FRET) [86]. In 1998 an experiment similar to the one in 1997 revealed discrete 120° steps in motor rotation [87]. The steps were observed in nanomolar [ATP] with actin filaments of $\sim$1 μm length. The rate of ATP hydrolysis without the actin filament was measured in solution at low [ATP] and was roughly equal to the measured rotational rate times three. Average motor torque was estimated from continuous rotation by calculating the rotational drag coefficient of the filament, ζ, according to $\zeta = \frac{(\frac{4\pi}{3})\eta L^3}{[ln(L/2r)-0.447]}$ [87], where η is the viscosity of the medium, r the radius and L the length of the filament. Torque from discrete stepping traces (which I will call 'transient' torque) was estimated by analyzing the temporal length of the step τ_{step}, where torque is given as $T = \frac{2\pi}{3}\frac{\zeta}{\tau_{step}}$. Both discrete and continuous rotation gave $T\sim$40 pNnmrad^{-1} motor torque. In one third of a revolution the work done by the motor is $\frac{2\pi}{3}T$, i.e. $\sim$ 80 pNnm, and the energy released by one ATP molecule, ΔG_{ATP}, is $\sim$80 pNnm under physiological conditions [88]. Thus one ATP is hydrolysed per 120° revolution and the motor operates at $\sim$100% efficiency (in 2 mM to 60 nM range). Later on, stepping rotation was visualized through angle-resolved single-fluorophore imaging to confirm that it is not an artefact of previous experiment (steps could have been the consequence of the imposed load on the rotor, rather then the signature of motor mechanics) [89] and the average motor torque in saturating [ATP] as well as 'transient' torque in [ATP] down to 2 nM was estimated to be $\sim$40 pNnmrad^{-1} [90]. Recently the motor rotation was investigated below 1 nM [ATP], at 200 pM and 600 pM [ATP] [90]. Based on these results at submillimolar [ATP] a different mechanism for motor rotation compared to the higher [ATP] cannot be ruled out. In 2001 rotational substeps were resolved with a slightly modified rotational assay, compared to the 1997 experiment [91]. Instead of an actin filament, a 40 nm gold bead was attached to F_1 (Figure 1.4 A). It was shown that an actin filament acts as an impeding load on the motor, while with a 40 nm gold bead, F_1 rotates at full speed as if free (at 2 mM ATP concentrations and 23 °C).

[ATP] dependence of rotational steps was also studied and the results are given

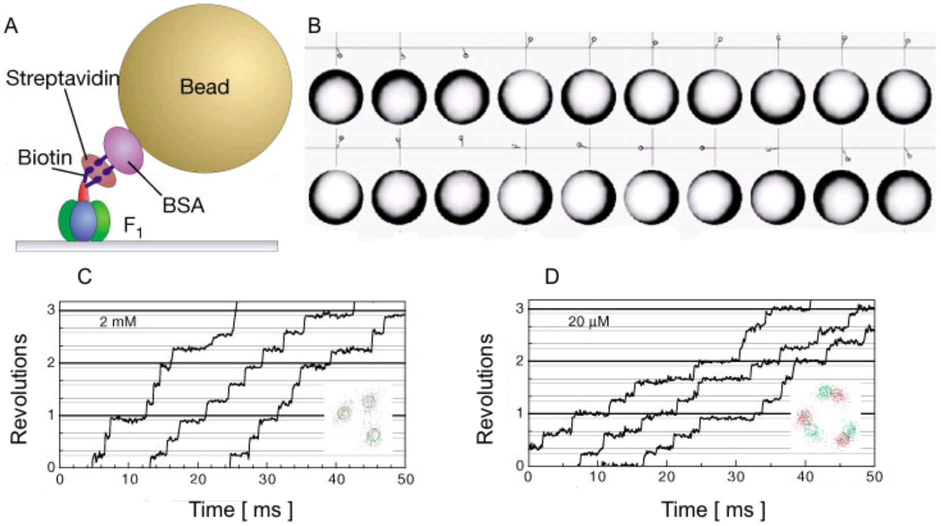

Figure 1.4: (A) Side view of the observation system. The 40-nm bead gave a large enough optical signal that allowed a submillisecond resolution; but the bead was small enough not to impede the rotation. (B) Sequential images of a rotating bead at 2 mM ATP. Images are trimmed in circles (diameter 370 nm) to aid identification of the bead position; centroid positions are shown above the images at 3x magnification. The interval between images is 0.5 ms. (C) [ATP]=2 mM (D) [ATP]=20 μM. Grey horizontal lines are placed 30° below black lines. Insets, positions of a bead within 0.25-0.5 ms before (red) and after (green) the main (90° or 120°) steps; runs lasting 0.5 s (2 mM) or 2 s (20 μM) were analysed. Circles indicate projection of ∼0° and ∼90° dwell points on an obliquely situated circular trajectory that best fit the data. Angles in the time courses are those on the oblique circle. Figure and the legend are taken from reference [91].

in Figure 1.4 C and D. At high [ATP] only 120 ° steps were seen, while at low [ATP] 90 ° and 30 ° substeps could be distinguished. The duration of the 120 ° step at saturating [ATP] was roughly equal to that of the 30 ° substeps at low concentrations showing that the 90 ° substep is ATP dependent. Since the 90 ° substep gets longer as the ATP concentration decreases it is sensible to assume that it corresponds to a step in which the ATP molecule binds to the enzyme. To confirm this conclusion histograms of dwell times between two main steps for different ATP concentrations were plotted and the following rate constants obtained from exponential fits: k_{on}=(3.0±0.1)$\cdot 10^7$ $M^{-1}s^{-1}$ from a single exponential fit to the histogram at low [ATP] and k_1=(1.64±0.06) ms^{-1} and k_2=(0.71±0.02) ms^{-1} from a double exponential fit to the histogram at saturating [ATP]. The calculated k_{on} is in agreement with the rate constant for ATP binding to the enzyme obtained from bulk experiments, therefore it is clear that 90 ° substep is an ATP waiting step. The 30° and 90° steps were later corrected to be 80° and 40° steps (bead-pairs were used instead of single beads giving better angle resolution) [92]. It was not clear, however, from the 2001 experiment that ATP binding immediately leads to the rotational 90° step. This was investigated in a later experiment where a fluorescently labelled ATP was used simultaneously as the bead-pair rotation was monitored [93]. It was found that: *(1)* ATP (or ADP) stays bound to the F_1 during two 120° steps, *(2)* the 80° substep happens immediately after the fluorescently labelled ATP binds to the motor, and *(3)* that the bead angle and polarization of the fluorescent dye were correlated, implying that the orientation of γ subunit towards β subunits dictates which β subunit will bind the ATP next. From the two reactions with almost equal rate constants occurring during the 40 ° substep, one was identified as the ATP cleavage in a later experiment, in which a mutant that slowly hydrolyses ATP and a slowly hydrolyzable substrate ATPγS were used [92].

Regarding the torque generation question: *(1)* It was proven that the so called 'DELSEED' region, a conserved acidic region on the β subunit in contact with the γ subunit, does not have a direct role [94]. *(2)* Torque generated by mutants with one, two or three altered catalytic sites that bind ATP slowly stayed the same despite the fact that the binding affinity (k_{on} rate) was reduced [95]. The torque generated by the wild type F_1 when using GTP or ITP whose k_{on} rate is lower then that of ATP [96] also stayed the same. This can be explained with the 'binding zipper' model proposed by Oster et al. [97] which divides the ATP binding process into docking of ATP (described by k_{on}) and the torque generation as a result of zipping of hydrogen bounds between P_i moiety of ATP and residues of the catalytic site. *(3)* The rotor tip inside the $\alpha_3\beta_3$ hexamer of thermophilic *Bacillus* is not necessary for torque generation [98, 99, 100, 101].

It is worth mentioning that the rotation of wild type F_1 is accompanied by frequent pausing; on average every 22 s F_1 will lapse into a pause (on average 32 s long) [102]. The pausing, caused by the Mg-ADP inhibited state, represents a regulatory mechanism, and the inhibition can be reversed by ATP binding to one of the non-catalytic α subunits [103, 104, 105, 106], presence of P_i at one of the catalytic sites [107] or by mechanical activation of F_1 (indicating that pushing the γ subunit forwards weakens the affinity of its catalytic side for ADP) [108]. In terms of the scheme that emerges for ATP hydrolysis of F_1, it is worth noting that a few experiments suggest a bi-site model of catalysis (a maximum of two β subunits are occupied with a nucleotide at some point during a 120° rotation), while others favour a tri-site model (three sites are occupied at some point during a 120° step). I will describe briefly a recently presented model given in reference [93] which describes known as well as unknown steps well (Figure 1.5). In the tri-site model it shows four successive ATP-waiting states (Figure 1.5 A, top), with the first 120° step driven by binding of Cy3-ATP (a fluorescently labelled, slowly hydrolyzable ATP analog used in the experiment). A detailed account of 120° to 240° step is given in Figure 1.5 B as follows: *(1)* ATP binds to the remaining empty site of the β subunit of F_1 (marked as site 0). *(2)* An 80° step occurs, driven by ATP binding. *(3)* At the site marked as -1, two reactions with equal rate constants need to occur (the rate limiting reaction must take place on site -1 based on the results of [93]). Possible candidates are P_i release and ATP hydrolysis, since ATP and later ADP stays bound for two steps. *(4)* A 40° step occurs, after which F_1 waits for the next step. ADP release needs to happen at some point between events *(1)* to *(4)* but is not yet clear when. Figure 1.5 C shows an alternative bi-site model. Even though this model incorporates most of the known facts about the F_1 hydrolysis cycle, more complicated scenarios cannot yet be dismissed (for example the existence of smaller shorter substeps). It is worth noting that a recent model [59] suggests that there is no single ‘main kinetic pathway’

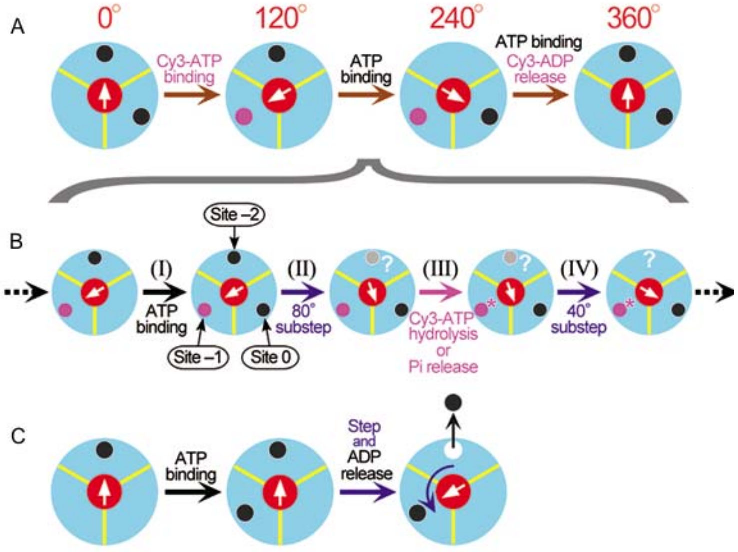

Figure 1.5: (A) Rotation scheme consistent with Figure 2. Four successive ATP-waiting states are shown. (B) Events between 120° and 240°. Nucleotide occupancy in schemes (A) and (B) alternates between two and three. (C) An alternative scheme in which the occupancy alternates between one and two. Figure and the legend are taken from reference [93].

(except under very low substrate). In total there are 64 possible reaction pathways (corresponding to the 64 occupancy states of the F_1 hexamer) and the substrate and product concentrations affect the overall potentials of F_1. Thus under experimental conditions multiple pathways exist. The authors of the paper conclude their work by saying: 'Attempting to fit data with an *a priori* selected biochemical path will likely prove fruitless or misleading'.

F_1 synthesis

Direct evidence for the chemical synthesis of ATP by mechanically driven F_1-ATPase was demonstrated in 2004 [109]. F_1 was attached to the coverslip surface by engineered His tags on β subunits as before, and the γ subunit was labelled with a magnetic bead attached via a biotin-streptavidin link. The magnetic bead was rotated using magnetic tweezers (see section 1.3). Rotation in the synthesis direction resulted in production of ATP, detected by the luciferase-luciferin reaction. Detecting the ATP proved to be the most difficult problem, due to the background ATP in buffers nominally containing only ADP. Thus sample droplets (3 μm in height and 30 μm in diameter) on a patterned area coated with Ni^{2+}-NTA were used to reduce the volume of the sample. A later experiment used a silicone device presenting a large array of micrometer-sized cavities enclosing F_1 in femtolitre chambers, over long periods of time [110]. F_1 was attached to the surface via His tags on α and β subunits and with a magnetic bead linked to the γ subunit as in the previous experiment [109]. The magnetic bead on the F_1 in the femtolitre chambers lacking ATP was rotated in the synthesis direction with magnetic tweezers. When the magnetic field was switched off the F_1 protein rotated in the hydrolysis direction, with the speed proportional to the amount of synthesized ATP. The mechanochemical efficiency was proven to be low for the $\alpha_3\beta_3\gamma$ subcomplex but was estimated to be around 77% when $\alpha_3\beta_3\gamma\epsilon$ was used. This result suggests that catalytic reactions on F_1 are tightly coupled to mechanical rotation, as well as that the ϵ subunit has an essential function during synthesis [111]. An illustration of the experiment and the number of revolutions with magnetic fieled switched on and off is given in Figure 1.6.

F_o

Investigating the membrane bound F_o part of the enzyme is difficult. A substantial effort has gone into proving and investigating F_o proton powered rotation from several laboratories around the world. Progress is slow and experimental data are noisy. The first observation of F_1F_o rotation during ATP synthesis or hydrolysis came in 2002 [112]. Na^+-translocating ATP-synthase of *Propionigenium modestum* specially labelled with a single fluorophore on one c subunit was used. The enzyme was immo-

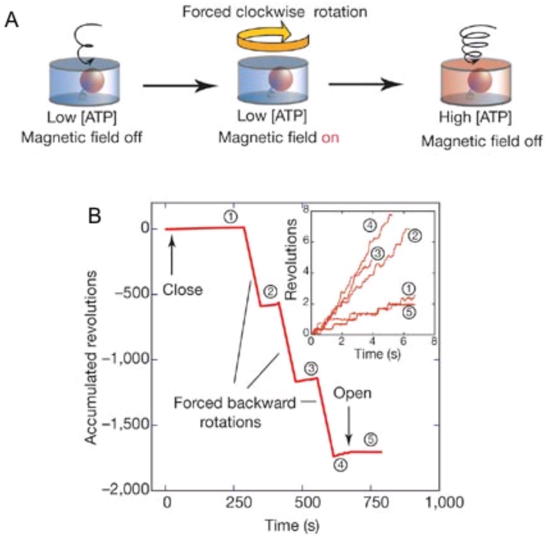

Figure 1.6: (A) An F_1 enzyme bound to a magnetic bead was rotated in a backward (clockwise) direction with magnetic tweezers within a microchamber in the presence of ADP, P_i and a small amount of ATP. Synthesized ATP accumulated in the chamber. (B) Before and after a forced clockwise rotation, spontaneous anticlockwise rotation was recorded as a means of detecting ATP synthesis through the increased rotational speed (see inset). The figure and figure legend are taken from [111].

bilized via His tags on β subunits and reconstituted into proteoliposomes. Rotation was observed with polarization-resolved confocal microscopy during synthesis, upon applying a diffusion potential, but not with a Na^+ concentration gradient alone, and during hydrolysis, in the presence of Na^+ but not without the addition of Na^+ ions. Rotation was sensitive to DCCD, a known F_o rotation inhibitor. In a later experiment F_1F_o from *E.coli* was engineered for FRET, with a donor on the γ subunit and acceptor on b subunit, and incorporated into liposomes and the synthesis and hydrolysis rotation observed [113]. The γ subunit rotated stepwise during proton transport-powered ATP synthesis, showing three distances with regards to the b subunit. Step dwell times were found to correspond to the catalytic turnover times.

Having introduced the known, here is my attempt at summarising the unknown aspects of the F_1 and F_1F_o chemomechanical cycle:

- Orientation of the γ subunit governs the affinity of ATP for a given β subunit: Upon binding of nucleotide β subunit changes conformation, however the question of how the motor torque is generated during hydrolysis still remains open. Some of the models for F_1-ATPase hydrolysis are quite explicit about motor torque generation, proposing a binding zipper model [59]. It would be interesting to confirm this experimentally.
- Three rate constants are known, which tell us about ΔG for three particular states each with a corresponding γ-angle, but can we map the energy profile for all angles?
- A recent model suggests that the energy profiles of the F_1 are dependent on the substrate/product concentrations [59]. Can this be confirmed experimentally?
- F_1 hydrolysis seems to be insensitive, while F_1 synthesis coupling efficiency is sensitive to the presence of ϵ subunit. How does the energy profile of these two subcomplexes $\alpha_3\beta_3\gamma$ and $\alpha_3\beta_3\gamma\epsilon$ vary with angle? Is it different to the hydrolysis direction, and if so, in what way?
- Is the second catalytic reaction during the ATP independent 40° step ADP release?
- Are there any smaller unseen substeps?
- The entire rotational cycle of F_o, as well as coupling between F_1 and F_o is unknown and poses a big challenge.

The system built was primarily designed to tackle the first four questions listed above. In fact, the detailed information about the motors' mechanochemical cycles and working mechanisms provided with the 'force clamps' and 'position clamps' experiments which combine optical traps with controllable feedback systems in the case of linear and DNA related molecular motors [15, 16, 17, 114] served as the motivation for building this system. It was designed as an 'angle clamp' with high temporal and angular resolution for the study of rotary molecular motors, the bacterial flagellar motor (bfm) and F_1F_o-ATPase. The 'angle clamp' feedback, as well as using a polystyrene bead duplex (bead pair) as a handle to apply external torque to rotary molecular motors, allows detail investigation of the motor energy profile at any chosen angle. At low [ATP], for example, with probes which present an impeding load (hence allowing only three 120° steps to be visualized) one expects interesting behaviour in the feedback signal while motor is held at the ATP waiting step. At smaller loads interesting behaviour should be seen at 6 different angles. The feedback signal would carry the signature of the motor energy profile. The temporal and angular requirements of such a system are further discussed in the section 2.1.1 and its design and performance in subsequent chapters of this thesis.

V-ATPase

V-ATPase is another rotary molecular motor [115]. It is an ATP dependent H^+ pump that transforms the energy from ATP hydrolysis to electrochemical potential differences of protons across different biological membranes. It is located within many intracellular compartments (endosomes, lysosomes, secretory vesicles) and has also been identified in the plasma membrane of certain cells [115, 116]. Since it regulates pH, a carefully controlled parameter affecting many cellular processes (for example, receptor-mediated endocytosis, protein processing and degradation, acid secretion, bone degradation [115, 116]), understanding of the structure and function of V-ATPase is of great importance.

Structurally V-ATPase resembles F_1F_o-ATPase, Figure 1.7. The main differences in

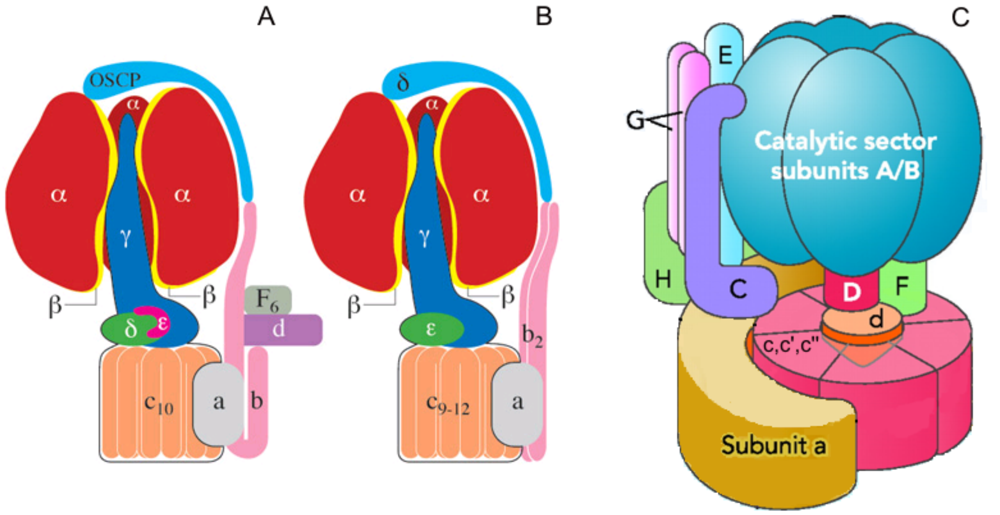

Figure 1.7: (A) and (B) F_1F_o-ATPase structure from Figure 1.3. is given for comparison. (C) Schematic model of yeast V-ATPase. Rotor subunits are colored in red; stator subunits are shown in blue. Figure (C) is taken from the reference [117]

function, compared to F_1F_o-ATPase, are due to the membrane embedded V_o part of the enzyme. F_o contains approximately twice as many central subunits in its rotor. A smaller number of membrane embedded rotor subunits allows V-ATPase to pump proteins even against large proton gradients, i.e. in conditions were F_1F_o-ATPase could not act efficiently as a proton pump. Since V-ATPase controls pH (or pNa) and membrane voltage, a very important question for understanding its function, is that of its regulatory pathways. These include the reversible dissociation of V_1 and V_o complexes (widely conserved from yeast to animal cells) [118, 119, 120], as well as other mechanisms such as subunit-subunit interactions [121], or interactions of the V-ATPase with other proteins that serve physiological regulation [122, 123]. The great interest in understanding these processes is further amplified by findings which attribute some diseases to genetic alterations of specific subunits of the V-ATPase. In terms of proposed models for the V-ATPase mechanochemical cycle, these are based on the models of F_1F_o-ATPase and suggest that cytoplasmic ions bind to the rotor subunits of V_o by passing through half channels in the stator subunits of V_o. The rotation of the rotor subunits of V_o is achieved using the energy stored in ATP, hydrolysed on stator subunits of V_1 [124, 125].

Bacterial flagellar motor (Figure 1.8)

The bacterial flagellar motor (bfm) is a rotary machine about 50 nm in diameter, embedded in the cell envelope and connected to an extracellular helical filament. The motor converts chemical energy to the rotational mechanical motion of some of its units (rotor). Chemical energy is supplied by the flow of ions down an electrochemical gradient across the cytoplasmic membrane into the cell (the protonmotive force (*pmf*), or sodium-motive force (*smf*)). Motor rotation is coupled to rotation of the flagellum thus enabling the cell to swim. Different species of bacteria use flagella to swim in different ways (there are exceptions: some bacterial species do not base their motility on rotation of flagella). Most of the work on the bfm so far has been on the closely related *E.coli* and *Salmonella enterica*. Both use several flagella that form a bundle and propel the cell forward, and H^+ ions are used to generate the rotary motion. Several interesting studies that have explored the similarities and differences between proton and sodium driven motors involve *Vibrio Alginolyticus*, which uses a single polar flagellum contained in a membrane sheath to swim and Na^+ ions to generate mechanical motion. Since bacteria swim to find places with favourable conditions, they actively direct their motion by changing the direction of the motor rotation, or by starting and stopping. These events are based on the information received from their sensory system. The bfm is a remarkably powerful motor achieving speeds of several 100 revolutions per second (rps), and up to 1700 rps in sodium driven motors [129].

STRUCTURE

The bacterial flagellum has a complex structure (Figure 1.8) composed of ∼20 different proteins with 40-50 genes involved in its expression, assembly and control. It spans the cell membrane extending into the cytoplasm and the cell exterior. It consists of a hook and a flagellar filament, hook-filament junction proteins, periplasmic

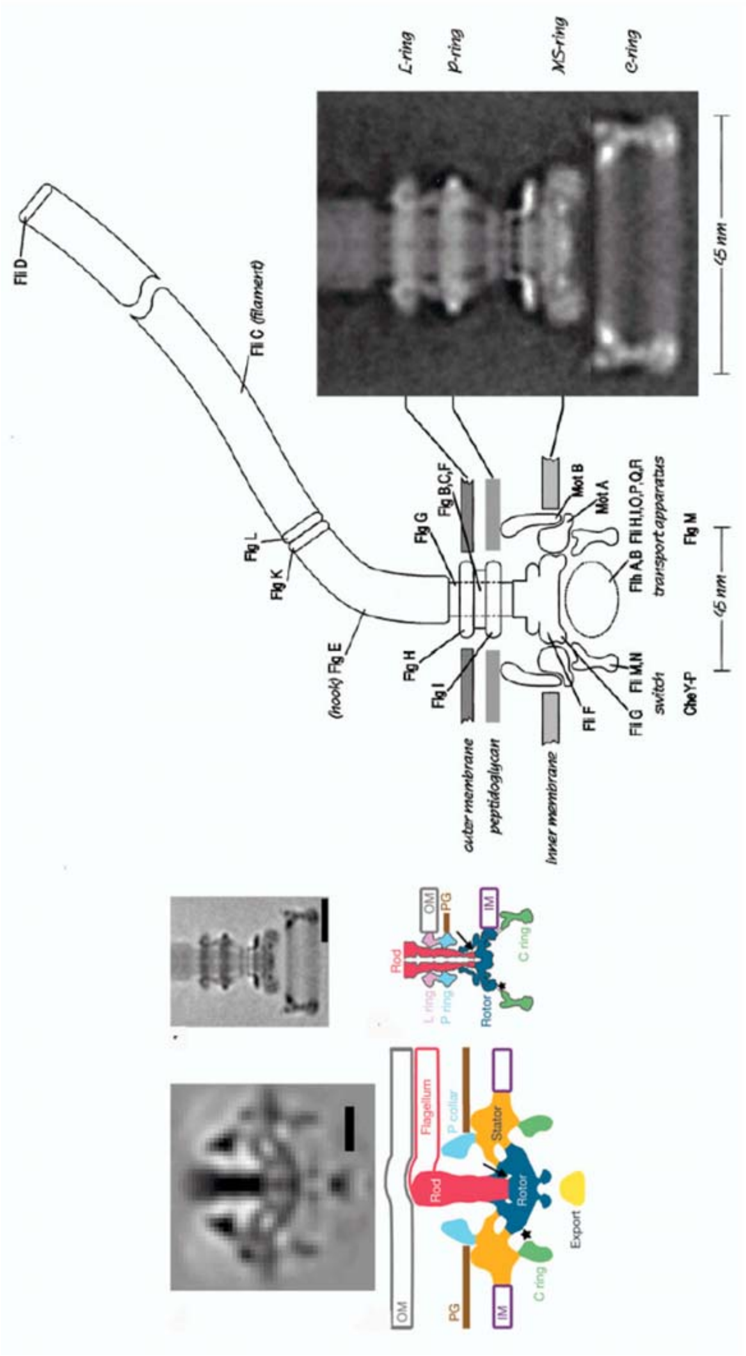

Figure 1.8: (right) A schematic diagram of Salmonella bfm based on an electron micrograph [126]. (left) Axial slice of the Treponema flagellar motor and the electron micrograph of Salmonella motor as well cartoon interpretation of both motors. Scale bars are 20 nm. Figures are taken from references [127] and [128].

P and outer-membrane L ring, rod, MS-ring, C-ring, stator units, capping proteins and an export apparatus [127, 130].

The flagellar filament is composed of the FliC protein (flagellin) present in up to 20 000 copies. The length of the filament can vary (usually 5-10 μm) and it can be re-grown when needed. It is composed of 11 protofilaments, each of which can be found in a short or long shape (depending on how many filaments are in each shape several helical forms of the filament are possible). Protofilaments are arranged in a cylinder with a slight tilt with respect to the cylinder axis [127, 130].

The hook is a flexible structure 55±6 nm in length [131], connected to the filament via hook-filament junction proteins FlgK and FlgL and composed of $\sim$120 copies of a single protein FlgE. FlgE proteins are arranged in 11 protofilaments which continuously switch from short to long during rotation [127, 130]. The hook displays a great flexibility but enough torsional stiffness to transfer torque to the filament.

The compliance of the bacterial flagella was measured by rotating tethered bacterial cells with optical tweezers. The compliance was nonlinear, showing a torsionally soft phase up to 180° and a rigid phase for larger angles [132]. It was suggested and later confirmed that the soft phase corresponds to the wind-up of the flagellar hook [133]. The compliance of the bacterial hook was measured with an *E.coli* strain that produces long hooks and no filaments. It was found, from the relaxation time after wind-up of the tethered cells with optical tweezers, that the compliance of the hook is similar to the compliance of the filament in the torsionally soft phase from previous experiment.

The periplasmic P ring and outermembrane L ring are composed of FlgI and FlgH proteins, and form either a part of the rotor or are fixed to the cell wall [134]. Rod proteins FlgB, FlgC, FlgF, FlgG share common structural motifs and are of similar lengths (so called axial proteins), thus forming a continuous, mechanically stable structure [135]. FliE does not resemble the axial proteins and is located at the distal end of the MS-ring probably serving as the junction protein between the components with axial and rotational symmetry.

The MS-ring is formed from the FliF protein [136, 137]. FliM and FliN comprise the C-ring, and together with FliG form the rotor and the ‘switch complex’ (mutations in FliG, FliM and FliN lead to defects in switching) [138, 139]. The ‘Switch complex’ also serves as the housing for the export apparatus of the bacterial flagella. The flagellum is built from the inside out and the export apparatus is used to pass the components of the flagellum through a channel at the center of the MS-ring. The copy number of FliM is 34±6, and FliN 111±13, supporting the idea that FliM and FliN form FliM_1-FliN_4 heteromers [140]. FliG and FliF have 26 fold symmetry [140]. Fusion of the FliM and FliN as well as FliG and FliF proteins does not hinder rotation (the MS-ring is thus considered to be the part of the rotor as well). Fusion of the FliG and FliM produces a non-functional motor and disables flagellar assembly. The C-terminal domain of FliG, with about 100 residues, interacts with one of the stator proteins, called MotA. Other parts of the FliG protein are essential for flagellar assembly and interact with the MS-ring [141, 142, 143, 144] and FliM [145, 142, 146]. FliM binds to the chemotactic signalling protein CheY [147, 148, 145, 149].

MotA and MotB are membrane proteins that form the stator of the H^+ driven motor (PomA, PomB, MotX and MotY are Na^+ driven equivalents). Mot (or Pom) proteins can be inserted into the assembled structure at the later stage by inducing the *mot* genes. Based on Na^+ driven motor studies, PomA and PomB proteins form a complex of four PomA and two PomB (same is likely for MotA and MotB) proteins [150, 151]. Two thirds of the MotA molecule are in the cytoplasm [152, 153] while MotB proteins have one membrane spanning α-helix and the rest of the molecule is in the periplasmic place [154]. MotB has a peptidoglycan domain near the C-terminus which anchors the stator unit to the cell wall [155]. Mutational studies identified Asp32 in MotB protein as the protonation and deprotonation site [156].

The type III export apparatus, as well as hook and filament capping proteins play a significant role in flagallar assembly. The export apparatus is the part of the flagella structure and is composed of FliO, FliP, FliQ, FliR, FlhA, FlhB, FliI, FliJ and FliH proteins forming a complex within the MS-ring as indicated in Figure 1.8 [130].

FUNCTION

Compared to the linear motors and F_1F_o-ATPase, the structure of bacterial flagellar motor is complex, nevertheless a great deal is known about the function of this beautiful motor.

Power source

The flagellar motor is powered by ions (for example: *E.coli*, *S. typhimurium* and *Streptococcus* use protons, while *Vibrio alginolyticus* uses sodium ions) that travel down an electrochemical gradient. The work required for an ion to cross the cytoplasmic membrane is the ion-motive force (*pmf* for protons, or *smf* for sodium ions), comprised from two terms:

$$imf = \Delta\psi + \frac{kT}{q} ln(\frac{C_i}{C_o}) \tag{1.4}$$

where $\Delta\psi$ is the difference in electrical potential between the inside and outside of the cell, i.e. membrane potential, kT is the thermal energy, q the charge of the ion and C_i and C_o are the activities of the ions inside and outside of the cell.

Several experiments, investigating power source of flagellar motors in *E. coli*, have been done. In Fung and Berg's experiment filamentous cells were drawn halfway into micropipettes, the cytoplasmic membrane of the cell fragment inside the pipette was made permeable by exposure to gramicidin, and the cells were subsequently energised with an external voltage source [157]. A high load was imposed on cell motors by markers used for monitoring rotation, and $\Delta\psi$ was found to be proportional to speed. Low load dependence of the *pmf* on speed was investigated in a later experiment. Cells were tethered to clean glass, their filaments were sheared and 0.4 μm beads attached to them. At a certain point the *pmf* was gradually collapsed by adding the ionophore CCCP, and speeds of tethered cell and the beads recorded in the process. Fast motor speeds (from the attached bead) were proportional to the slow motor speeds (tethered cell), and since the rotation speeds of the slow motor were known to be proportional to *pmf*, the slow motor speeds were rescaled to show the *pmf* of the cell. Thus a speed-pmf plot for fast motors was generated and found to be linear with pmf (although the relative contributions of membrane potential and pH gradient were not known) [158]. Each contribution to *imf* given in Equation 1.4 was investigated separately on *Streptococcus* cells, which in the absence of exogenous energy source stop swimming and are sensitive to ionophores and uncouplers. The contributions of pH and the membrane potential to pmf were found to be equivalent in driving the motor [159, 160].

Sodium-driven motors in *Vibrio alginolyticus* have linear dependence in pNa but the *smf* was not measured [161].

The contributions of membrane potential and pNa to *smf* were studied independently and on individual cells in a high-load regime, in a recent work by Chien-Jung Lo [162]. C.H. Lo studied chimeric sodium-driven flagellar motors in *E. coli*, containing rotors from the proton-driven *E.coli* motor and stators that combine proteins from proton-driven *E.coli* and sodium-driven *V. alginolyticus* motors [163, 164, 165]. Membrane voltage was varied by changing external pH and pNa by changing external sodium concentration. Intracellular sodium concentrations and membrane potential in single cells were measure using two different fluorescent dyes [163, 162]. Motor speed was found to be proportional to *smf*, with equivalent contributions from pNa and $\Delta\psi$ in agreement with previous work. The linear dependence of speed and smf in high load regime is consistent with high efficiency and tight coupling. It is important to note, however, that in the high load regime, the load is the limiting factor to rotation, not for example, the arrival of ions. The preliminary results in low load regime suggest that equivalence of $\Delta\psi$ and pNa does not extend into the high-speed regime [162]. The number of ions required for one revolution (with one stator unit present, see discussion about stator units below) is 36±6. Given that the number of directly observed steps in the low load regime is 26 [164], this result indicates that more than one ion is needed per step, or that the tight coupling model as well as proportionality between speed and *smf* does not extend to the stepping experiment conditions.

There is one report that measures the number of ions passing through the motor with maximum number of torque generating units present, on average (1240±240) protons per revolution [166].

Torque generating units

As mentioned before, proton flux in the bacterial flagellar motor passes through torque-generating units (probably consisting of four motB and two motA proteins [151]). Early studies showed that *mot* mutants of *E.coli* do not rotate [167], however they can be 'resurrected' through protein synthesis by lambda transducing phages [168]. This activation has also been studied on the level of single motors. Cells of a *motB* strain carrying plasmids with wild type *motB* genes controlled by the *lac* promoter, as well as cells with *motA* and *motB* point and deletion mutations, carrying plasmids with wild-type *motA* and *motB* genes, were tethered to the surface and resurrected. Step0filled increments in motor rotation were observed upon addition of the inducer, showing that bacterial flagellar motors contain several torque-generating units [169, 170]. The maximum number of units observed, corresponding to number of steps by which the rotational rate increased, was eight in the tethered cell experiments [170]. More recently, using a polystyrene beads attached to the sheared filaments, number of discret steps observed has increased to at least 11 [171], confirmed by counting fluorophores by the stepwise photobleaching of single GFP molecules attached to MotB component of the stator [172].

Torque-speed curve

Up until recently the best way of understanding the mechanism of torque generation and how ion flow is coupled to the motor rotation, was by investigating the torque-speed relationship of the motor. Steps have since been observed that provide the most direct insight into the energy profile of the motor. Future research is likely to use steps as the main biophysical probe to explore the motor's mechanochemical cycle.

Since steps have been observed only recently, measurements of the torque of the bfm have been made at a range of speeds, using several different techniques.

Changing the load attached to the motor (an entire cell, or a bead of different size) will give information in the range of different CCW (looking at the motor from the distal part of the filament) speeds. In these experiments motor torque is balanced by the torque exerted on the object by viscous drag $T = f\omega$, where f is the frictional drag coefficient of a rotating object in viscous medium and ω is its angular velocity [173, 174]. However, in this way the motor speed at zero load as well as information for CW speeds is not accessible. For this, a means of applying external torque to the motor is needed.

The main method for this purpose is electrorotation [175, 176, 177], but an optical trap has also been used [178] (optical traps offer further potential for increasing the range of speeds one can achieve [179]). The torque speed curve of the bfm is given in Figure 1.9 A. At 23°C the motor torque is approximately constant (slowly declining) from ∼-100 Hz to ∼200 Hz. At speeds higher than ∼200 Hz the motor torque declines approximately linearly. The position of the point where the torque changes from constant to linearly declining (called the 'knee') is temperature dependent, however at low speeds the torque is independent of temperature. This is consistent with the assumption that the motor operates near thermodynamic equilibrium and at high efficiency, at low speeds and that the torque decline at high speeds results from limits in the rates of proton transfer. The torque-speed curve given in Figure 1.9 A suggests that the 0-torque line is crossed at speeds of ∼300 Hz at 23°C.

The torque speed curve at different stator numbers was studied as well, and is shown in Figure 1.9 B. Torque is proportional to the stator number at high load, while its shape at the low load suggests that one unit rotates the motor as fast as many. Thus it is likely that the motor has a high duty ratio, i.e. stator units spend most of the time attached to the rotor. In Figure 1.9 B the smallest load studied was 300 nm diameter bead, from which it was concluded that the duty ratio is at least 0.6, but it is likely higher, close to 1.

Steps

Investigating the dependence of variance in the rotation rate over the mean rotation rate of the bfm, for a motor with a known number of torque generating units as well as for a broken motor, lead to expectation that protons passing through stator units of the bfm move the stator unit along the periphery of the rotor by one fixed-increment step [180, 181]. Rotating motors were shown to behave like Poisson steppers, with ∼50 steps per torque generating unit, and appeared to step independently. Broken motors showed free rotational diffusion [180, 181]. Increase in the number of steps per revolution with the number of torque generators suggests that the torque generating units have a high duty ratio. However, it was only recently that the steps in motor rotation have been observed directly. For this a Na^+-driven chimaeric flagellar motor in *E.coli* was constructed. At low sodium-motive force and with controlled expression of a small number of torque-generating units 26 steps per revolution were observed. The number of steps is in agreement with the number of FliG proteins expected to interact with motA proteins in stator units [164]. It ap-

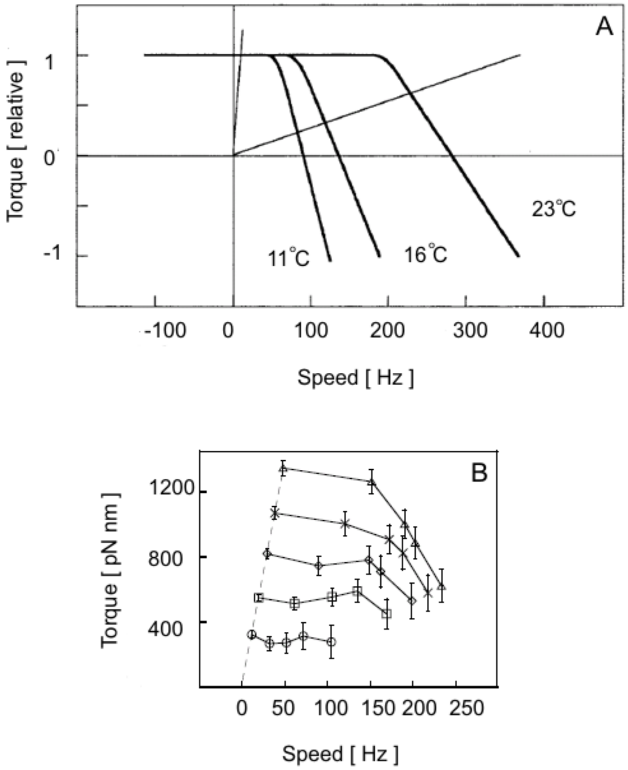

Figure 1.9: Torque speed curve for the flagellar motor of E. coli. (A) Three temperatures are shown (thick lines), together with two load lines (thin lines). One is for the wild type *E.coli* cell, with effective radius about 1 μm, the other for the minicell with an effective radius of about 0.3 μm. In the low-speed regime, torque is some what misrepresented and shown constant, although it declines about 10% between stall and the knee [174]. Figure and the legend are taken from reference [127] (B) Torque speed curves of one (bottom) to five (top) torque-generating units. The points for a given bead size fall on a line (one such line is shown) whose slope is equal to viscous drag coefficient. Reading from left to right the bead sizes used were 1.03 μm, 0.535 μm, 0.41 μm, 0.356 μm, 0.3 μm. Figure and the legend are taken from reference [173].

pears that the number of steps with one or two torque generator units stays 26 [164], however this is still not clear. At a low speed of 1 Hz, a doubling in speed could be due to a random fluctuation as well as a change in number of torque generating units.

Switching

Active control of the direction of motor rotation is essential for responding to stimuli and swimming towards places with favourable conditions. Changing the direction of motor rotation, starting and stopping, is based on the information received from the sensory system. The likelihood of changing the direction of spinning is enhanced by CheY, the chemotactic signalling protein which when phosphorylated (CheY-P) binds to the cytoplasmic face of the bfm (probably to FliM). The phosphorylation of CheY is catalyzed by the kinase CheA, the activity of which is controlled by chemoreceptors (either activating or inhibiting CheA). The dephosphorylation of CheY-P is accelerated by the phosphatase CheZ. Bacterial cells will adapt to the change in the stimuli by returning to the pre-stimulus behaviour in the presence of the stimuli, by the methylation and de-methylation of the receptors (by CheR and CheB, respectively).

How the transition from one direction to the other occurs within the motor when CheY-P binds to FliM is still under question. Early experiments suggest that switching is an all-or-none Poisson process. When the distribution of switch intervals was looked at, to a first approximation, it was exponential [182]. From tethered cell experiments it was concluded that the time it takes for a switch to happen is not longer then 10 ms (this includes unwinding and re-winding of the tether) [127], and from the observation of single filament by laser light scattering, that it is completed in 1 ms [183]. Later, the switching interval distribution was looked at in conditions where the chemotaxtic signalling pathways were not perturbing the measurement. The strain used lacked CheA and CheZ but CheY was replaced by a mutant active without phosphorylation (CheY**) [184]. In another study CheY was expressed in a strain, without CheZ and CheB, in which all of CheY is phosphorylated [185]. Both studies found that the CW bias has sigmoidal dependence on the CheY concentration, and that the distributions of waiting times are exponentials.

Based on these studies it was proposed that switching is a thermal isomerization process, where the system sits in one of two potential wells, jumping from one to the other with exponentially distributed waiting times.

The effect of chemotactic signalling on motor switching was also looked at in an experiment that used CheY-GFP to determine the concentration of CheY protein inside individual cells. Having shown that the CW bias is very sensitive to [CheY-GFP] (the response of the motor to changes in [CheY-GFP] was much steeper than previously thought based on the measurements of proteins concentrations averaged over cell populations) the study concluded that the motor acts as an amplifier [186].

In some of the studies of switching mentioned so far, pauses and slowdowns were observed, but have been attributed to artifacts of the experiment. There are however studies which look at those events, and their relationship with chemotaxis [187]. These events have been included and explained by a general stochastic 1-D Ising model, which proposes a possible mechanism by which the FliM-CheY-P interaction leads to a switch [188, 189]. The model is based on a ring of protomers (FliM), each of which can be in two states (CW or CCW). FliM in each state can also bind a ligand (CheY-P). A change from one state to the other is accompanied with a change in a free energy. Crucial for the model is the assumption of the conformation-dependent cooperative interactions between adjacent FliMs that favour like conformations. Inclusion of this interaction can integrate the activities of FliMs over the cluster*. The model also suggests a physical interpretation for the fluctuations in speed as well as for the experimentally observed pauses. If a given FliM undergoes a conformational change from a CW to CCW state, due to the coupling energy term, the change may spread to the rest of the FliM proteins present in the ring. If all of the FliMs change their conformation, the switch will happen as a

---

*The exact behaviour will depend on the value of the change in the free energy, [CheY-P] and the relationship between the FliM number and the coupling energy. With realistic values used in the model, the sensitivity coefficient obtained is comparable to the one obtained experimentally [188] result. However if only few do so, and the number of FliMs in CCW state returns to zero, as it does so, fluctuations in speed or even pauses will be observed (depending on the number of FliMs that did undergo the transition).

Experiments described so far, which looked at the wild type switching interval distribution and concluded that it is exponential, obtained the distribution by averaging the CCW and the CW series from individual cells (before spectral analysis). In a more recent experiment, Korobkova et al. looked at the distribution of CW and CCW intervals for each wild type cell, and found that, on the scales from 5 to 10^3 seconds, it differs from the population distribution [190]. For the CCW intervals, it looks more like a power law rather than an exponential. They also looked at the interval distribution for a mutant with CheY**. They found that the exponential distribution for the CCW intervals is recovered on long time scales. In a later experiment Korobkova et al. looked at the CW and CCW interval distribution of the same mutant but this time they binned the cells according to the CW or CCW bias [191] (allowing them to study the behaviour of the motors with approximately the same [CheY**]). What they found is that the probability density of CW and CCW intervals for each bias bin behaves like a Gamma distribution rather than an exponential, indicating that there are several independent exponentially distributed events occurring rather than just one. These they call hidden steps (most likely due to their experimental resolution where motors never stop rotating and exhibit only CW or CCW rotation in their experiment, hence hidden). They also speculated that these hidden steps correspond to the conformational changes in several FliMs that do not result with a switch. However, the data obtained by Fan Bai, Richard Branch and I, and analysed by Fan Bai and later Richard Branch, shed some new light on the problem of switching, the switch times and the switch interval distribution. The results obtained are briefly discussed in section 4.3.1.

Model

Having looked at the experiments performed on the bfm, can we answer (or how close can one come to answering) the question of what is the energy profile of this motor? There have been several models giving several possibilities. I will focus on a recent model proposed by Jianhua Xing and Fan Bai [192]. It is the only model that gives torque speed curves in agreement with experiment (Figure 1.10 A) and makes several interesting predictions. Also, the model gives a framework based on four assumptions and the physics of the bfm is not sensitive on the model details and parameters, which can be further elaborated once the new experimental data becomes available. The four assumptions are as follows; *(1)* the rotation of the motor is observed through a soft elastic linkage between the motor and the viscous load, *(2)* motor rotation and ion transport are tightly coupled, *(3)* the power stroke is driven by a conformational transition in the stator that is triggered by the protons hopping onto and off the stator, probably via the MotB residue D32, *(4)* the ion channel through the stator is gated by the motion of the rotor. The first assumption allows the motor and the load to move on different time scales, and as a consequence the bfm torque is constant in the low speed, high load regime. The second and third assumptions are necessary to explain the linear dependence of *imf* and speed in the low speed regime, while the fourth assumption allows the ion conductance to vary with the motor speed, explaining the concave shape of the torque-speed curve. The rotor-stator interaction is shown in Figure 1.10 B. The power stroke is driven by the free energy of two ions binding to the Asp32 sites of the MotB proteins. The cycle is accomplished by two half strokes, one by each MotA loop, alternating in contacting successive FliG proteins on the rotor (Figure 1.10 B, right). The model prediction of constant torque in the low speed regime is due to the time-scale separation between the motor and the load dynamics. In the high load regime the system evolves ‘infinitesimally’ slowly so the probability distribution is always in the region of potential with a negative potential gradient, the rest of the motor potential features are thus masked and the torque is constant. As the load decreases in size the probability distribution moves faster down the potential gradient and is more likely to be found centered in the potential minimum, torque will thus 'feel' the effect of the steep positive potential gradient decreasing its value (Figure 1.10 B, left). If in addition, the chemical rate constant is not modelled with a constant value in the transition window, but instead a triangle function is used, this positive feedback mechanism will contribute further to the sharp decrease in the torque. The model also predicts non-linear *imf* vs. speed dependence in low load regime.

My introduction to the bacterial flagellar motor has covered the structure, known aspects of the motor function, and a recent model for the mechanochemical cycle of the motor. To conclude, I will summarize some of the most interesting questions that remain to be answered and that guide future research:

- Properties of the hook and the importance of hook flexibility in motor rotation. Effect of the hook stiffness on the observed torque-speed curve as well as on the resolution of step observation.
- *Imf* vs. speed relationship in the low load regime
- The shape of the torque-speed curve, with different number of stator units present
- Number of steps in the presence of two or more stator units, together with the step dwell times and backward steps
- Mechanism of switching (switch time, switch interval distribution)

The angular resolution and high sampling rate of my system, can help in answering many of these questions. The option of controlling a bead pair attached to the bfm via the filament stub offers even greater possibilities, for example: increasing the time resolution needed for step detection by holding the bead pair with

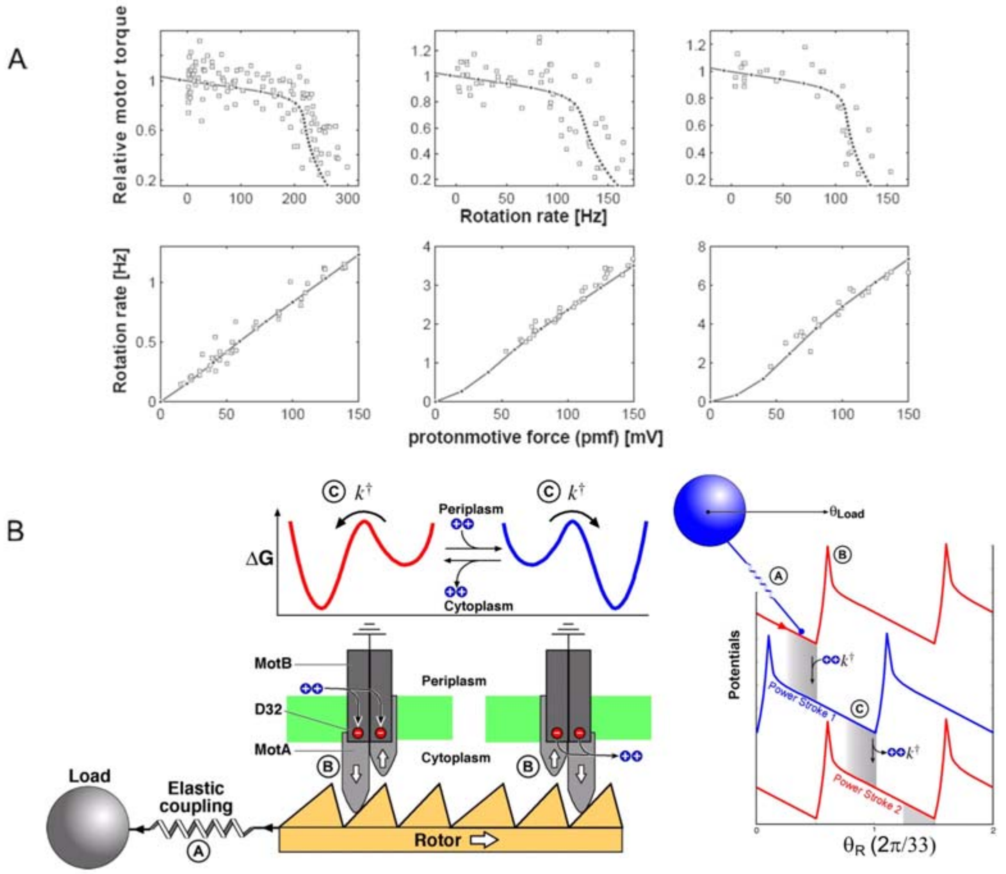

Figure 1.10: Comparison of model calculations and experimental data. (A) Upper: Experimental torque-speed curves at different temperatures (squares). The filled dots are calculated from the model. Lower: The linear dependence of the motor rotation speed with *imf* at three different high loads. The experimental data (squares) are taken from Fung and Berg [157]. (B) Left: Schematic illustration of one motor cycle. Right: The driving potentials of the stator given on the left. A is the soft elastic coupling between the rotor and the load, B the sharp peaks in the potential may be due to steric interactions between FliGs and the MotA cytoplasmic loops that prevent thermal fluctuations from taking the system down the backside of the potential.The (shaded) transition regions specify the positions where the transitions between the potentials can take place. Labels AC correspond to Assumptions 13 in the text. The Figure was obtained from Fan Bai and is essentially the same as in reference [192].

feedback, controlling the speed of the bead pair rotation and gaining information on the torque-speed curve, and investigating the properties of the hook. Finally, if it is possible to increase hook stiffness, controlling the angle of the bead pair with feedback can give information on the energy profile of the motor at a given angle.

1.2.3 Synthetic molecular motors

One direction of work on synthetic motors uses single strand DNA molecules with attached cargo to move along a DNA track. A set of additional complementary single strands is used as the fuel. The main problems with DNA fuelled motors arise from the fuel itself: how can it be used only when it's needed and extracted when it is potentially blocking the motor? Current efforts are directed towards achieving continuously running motors as well as designing a track that will allow the cargo to be transported between two desired points [193, 194]. Another direction is being pushed forward by synthetic chemists. Although the field is in its infancy, using the properties of molecules such as rotaxanes, catenanes, helical-shaped alkenes and trypticene-type propellers, controlled motion on the molecular-level has been demonstrated [195, 196, 197, 198, 199]. This opens the doors for more ambitious rotary and translational motion as well as for coupling of that motion to other functions.

1.3 Single Molecule Techniques

Techniques used for single molecule studies can be broadly divided into **imaging techniques** and techniques where **force or torque is exerted on the molecule** under study (some of the techniques can be used for both). I will briefly mention some of the commonly used techniques and give a broader introduction to optical tweezers, a technique used during my research. By doing so I hope to place the capabilities and restrictions of the optical tweezers in context with other available methods.

The focus of imaging techniques has been largely to overcome the resolution limit of optical microscopes. **Optical microscopes** use visible light passing through the sample to achieve a magnified image of the object in the sample. A lot has been achieved in terms of improving the image quality and magnification of optical microscopes, but the highest resolution is set by the diffraction limit. Resolution limit has been pushed further with **electron microscopes**. Using beams of electrons, having a much smaller wavelength then the visible light, allows much higher resolution. However, the electron beam needs to pass through a vacuum in order not to be scattered by air molecules. This places restrictions on the sample preparation.

One other imaging technique that has had a great impact on the field of single molecules studies is **fluorescence microscopy**. A fluorophore (fluorescent molecule) in its ground state will be excited after exposure to photons. When relaxing to the ground state it will emit a photon of longer wavelength. The excitation and emission wavelengths will differ from system to system. If the fluorescent chemical group is attached to a biological molecule of interest very sensitive detection experiments can be performed. As well as in many other applications the potential of fluorescence microscopes was explored when studying processes localized on the cell surface. However if the excitation is coming from above the specimen all of the fluorophores (the fluorophores bound to the cell surface and the once in the solution are in equilibrium) will get excited and, when observed from above the specimen (epi-fluorescence), give rise to high background noise. Therefore a **total internal reflection fluorescence microscope (TIRFM)** was developed, based on the knowledge that if illuminated at a certain angle the electromagnetic wave will get fully reflected from the surface, with an evanescent wave passing into the solution. Since the wave decays exponentially with the distance from the surface only a small region will get illuminated by the incoming light (and only the fluorophores close to the surface will get excited), avoiding excitation of the fluorophores in the solution. Another technique that will reduce background noise is **confocal fluorescence microscopy**. It relies on focusing the laser light into a small focal volume within the sample, and exciting fluorophores within this volume. The position of the focused laser light within the sample can be changed allowing scanning in z-axis. The fluorescent light emitted from the small volume can be separated from the reflected laser light and detected (usually) by a photodiode.

To obtain fine information about the dynamics of two fluorescent molecules, one can monitor dipole-dipole interactions between them. One of the fluorescent molecules, a fluorescent donor, is excited at its specific wavelength. It then excites, with dipole-dipole interactions, the second fluorescent molecule, a fluorescent acceptor. The donor returns to its ground state. The efficiency of fluorescent transfer (E) depends on the distance between donor and acceptor molecules and is given as:

$$E = \frac{1}{1 + \frac{r^6}{R_0^6}} \tag{1.5}$$

where r is the separation of donor and acceptor and R_0 Förster distance at which the rate of donor radiation equals the rate of acceptor absorbance (the transfer of energy by FRET is 50% efficient). If observed in a certain time interval, **fluorescence resonance energy transfer (FRET)** efficiency will give information about the dynamics of the two molecules.

An **atomic force microscope (AFM)** is another widely used imaging technique. It is based on a different concept. It uses a physical probe, instead of electromagnetic waves or electron beam, to directly probe the surface of the specimen. The probe is brought close to the sample surface, and the forces between the tip and the sample are monitored. A **scanning tunnelling microscope (STM)** uses a physical probe as well. It is based on a quantum mechanical effect of electron tunnelling. A probe is scanned across the specimen surface, while voltage is applied between the probe and the surface. Applied voltage will cause electrons to tunnel, i.e. jump between the probe and the surface resulting in weak currents exponentially dependent on the distance between the probe and the surface.

Apart from being imaging techniques, both the STM and the AFM are used as force transducers. The STM can be used to manipulate individual atoms. It can remove or add individual electrons from atoms. While the AFM is often used to exert force on biological molecules of interest tethered between the tip and a surface.

Magnetic tweezers are often used as a means of exerting torque on particles attached to molecular motors or DNA. A system of electromagnets is usually used to create field gradients, producing a force on a super-paramagnetic object. Adjusting the current running through the coils enables changes in intensity and direction of the resulting force. As described in section 1.2.2 this technique has been used to apply external torque to F_1 by controlling the angle of magnetic beads, 470 nm to 700 nm in diameter, attached to the γ-subunit [108, 109, 111]. The way in which torque is applied with this technique does not enable the high spatial and temporal resolutions that are possible with optical traps. For example, the typical resolutions reported using magnetic beads are several seconds and 5° [108].

Electrorotation is another technique for applying controlled torque. It is used to apply torque to dielectric objects such as bacterial cell, in order to study the mechanical properties of the bacterial flagellar motor. The technique uses microelectrodes arranged in a cross (with a small gap in the middle) to generate a rotating electric field. The field polarizes the object located in the gap between the electrodes. The polarization of the object lags behind the rotating field, thus the dipole is trying to line up with the field thereby exerting torque on the object. In section 1.2.2 experiments in which the torque was applied to the bfm with the cell body as the handle were described. However, the cell body is considerably larger than the polystyrene beads used in typical optical trapping experiments, and therefore requires extremely large torques to attain the high speeds (∼300 Hz) that are characteristic of the flagellar motor. Furthermore, as with magnetical tweezers, high spatial and temporal resolutions that are possible with optical traps cannot be achieved due to the size of the handle and the way in which the torque is applied.

1.3.1 Optical tweezers

Since their invention just over 20 years ago, optical traps [200, 201, 202, 203] have been widely used for research purposes in both physics and biology, ranging from the cooling and trapping of neutral atoms [204] to manipulating live cells and viruses [205, 206]. More recently, optical traps have been extensively employed in the experimental investigations of molecular motors [207, 208]. Their unique ability to apply picoNewton forces to micron-sized particles, while simultaneously measuring displacement with nanometer precision, often makes them the best tool in practice. Optical forces and torques arise from transfer of linear and angular momentum, carried by photons (electromagnetic wave), upon reaching an object. In most cases the resulting force will push the object in the direction of the incoming light, but the configuration in which all the optical forces and torques acting on an object cancel each other can be achieved. Thus, a total force (and torque) acting up on an object is zero and the object is optically trapped. This configuration is usually achieved by tightly focusing the laser light with an objective with high NA. To gain some intuitive understanding on how the total force of zero arises, forces acting upon an object have traditionally been decomposed into two parts: (a) a scattering force and (b) a gradient force. The scattering force is the total force pushing the object forwards, while the gradient force is the total force pushing the object (dielectric) in the direction of the light intensity gradient. Fluctuating dipoles will be induced in a dielectric particle in the laser focus, and it is the interaction of these dipoles with the inhomogeneous electric field that will give raise to a so called gradient force (proportional to the dielectric polarizability and the intensity of the gradient) [209, 210].

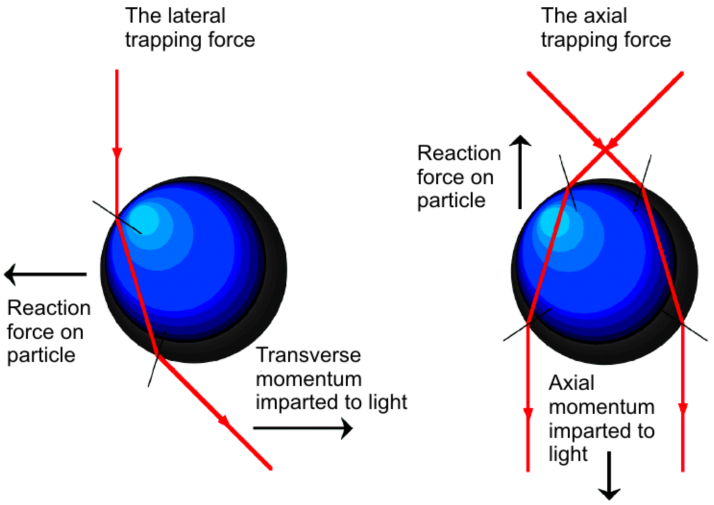

Figure 1.11: The ray optical origin of the lateral and axial trapping force within optical tweezers. Figure and the legend are taken from reference [210].

If the wavelength of the electromagnetic wave is significantly smaller than the object (d$\gg \lambda$), determining the total force and torque acting on an object can be done with a **ray-optics model**. The beam is treated as a superposition of rays and the two refractions when a ray enters and exits the particle are modelled using Snell's law. Each ray undergoes a change in momentum between the incoming and outgoing ray. Due to conservation laws, the momentum in a system remains invariant, so the transfer of momentum between ray and particle can be calculated for each ray that is refracted. Summing the momenta will result in net force, Figure 1.11 [210]. For an object much smaller than the wavelength of the electromagnetic wave (d$\ll \lambda$) conditions of **Rayleigh scattering** are met and the dipole approximation is used for describing properties in a simplified manner. The object is considered an emitting dipole and the force that acts on the particle can be decomposed into a scattering and a gradient force [210], given as

$$F_{scat} = \frac{I_0}{c}\frac{128\pi^5 r^6}{3\lambda^4}(\frac{N^2-1}{N^2+2})^2 n \tag{1.6}$$

and

$$F_{grad} = \frac{-N^3R^3}{2}(\frac{N^2-1}{N^2+2}) \bigtriangledown (\mid E \mid)^2 \tag{1.7}$$

where r is the radius of the object, I_0 is the light beam intensity and N is the ratio of the refractive index of the object to the index n of the surrounding medium.

If the object size is comparable to the laser wavelength (d$\sim \lambda$), and this is usually the case for the objects of interest in biological studies (this thesis included), one has to solve the rigorous diffraction model on case by case basis, by *(1)* calculating the field around the particle and *(2)* by applying Maxwell's stress tensor to determine the force acting on the object [211]

$$\langle \mathbf{F} \rangle = \int_S \{\frac{\epsilon}{2} Re[(\mathbf{E}\cdot\mathbf{n})\mathbf{E^*}] - \frac{\epsilon}{4}(\mathbf{E^*}\cdot\mathbf{E})\mathbf{n} + \frac{\mu}{2} Re[(\mathbf{H}\cdot\mathbf{n})\mathbf{H^*}] - \frac{\mu}{4}(\mathbf{H^*}\cdot\mathbf{H})\mathbf{n}\} dl' \tag{1.8}$$

where S is the surface of the particle and **n** the normal to the surface pointing outward [212]. Calculating the field around the particle involves solving the problem of the representation of the beam. A number of available techniques require that the trapping beam (i.e. the incident field) be represented as a plane wave spectrum in terms of vector spherical wave functions (VSWF) [211]. An optical trap is a strongly focused Gaussian beam, but the problem is that the standard representation of Gaussian beams does not satisfy the Maxwell equations, leading to some difficulty in finding the plane wave of VSWF spectrum. In addition, the trapping beam is not really a Gaussian, it is truncated. However, satisfactory methods exist [213, 214].

Once the incident field has been written there is a wide variety of methods to find the field around the object. Some are semmi-analytical and some numerical, but an adequate method for a particular case can usually be found [211]. To give a 'feeling' for the mentioned variety I give a list of some of the available techniques: (a) A generalized Lorentz-Mie theory (GLMT, describes in its original formulation the interaction of an arbitrary shaped beam with a homogenous sphere, and it has been expanded to other geometries) [215, 216], (b) T-matrix method [217, 218], (c) multiple multipole method (MMD) [219], (d) finite element method (FEM) [220, 221], (e) finite difference time domain method (FDTD) [222], and (f) discrete dipole approximation (DDA) [223]. Since the rigorous model needs to be solved, and given that the force acting upon an optically trapped sphere-like object when displaced from the zero force position by a small amount can be easily calibrated, it comes as no surprise that experimental biophysicists are mostly satisfied with intuitive description of how optical trapping works, and actually seeing it work in practice using dielectric microspheres. For objects of different geometry, anything not as beautifully symmetrical as a sphere, the situation is more complicated. Forces and torques acting on such objects need to be considered more carefully.

The simplest optical trapping is achieved by focusing a laser with a microscope objective of high numerical aperture. The back aperture of the objective is usually slightly overfilled to achieve the smallest possible focal spot, i.e. the steepest gradient. The trapping laser beam can be steered by placing a steering device in the back focal plane of the objective. An angular displacement at this point will produce lateral displacement in the specimen plane without affecting alignment with the objective back focal plane. The simplest steering device is a mirror, and acusto-optic deflectors or electro-optic deflectors are used for fast automated steering. Apart from a single trap multiple tweezers can be achieved as well, either by rapid scanning between trap positions [224, 225], having separate light paths [226] or using holographic methods [227]. However, these approaches, especially in the case of holograpic methods, require more complicated trapping systems. The position detection in an optical tweezers system is usually achieved with the use of one of the following methods: (1) a video camera, (2) by imaging the object directly to quadrant photo diode, (3) polarization interferometry or (4) back-focal-plane (bfp) interferometry [209]. In polarization interferometry, a polarized laser light is split into two paths and recombined after passing through the specimen. The phase shift in the polarized laser light is calibrated against the displacement of the object in the specimen plane. Back-focal-plane interferometry is based on the interference between forward-scattered light from the object in the specimen plane and unscattered light. The interference signal is usually monitored with the quadrant photo diode.

Significant progress has been made in trying to achieve the rotation of objects in optical tweezers, a summary of which is illustrated in Figure 1.12.

If transfer of angular momentum carried by photons is achieved upon scattering by a particle, a torque can be exerted upon that particle. Photon angular momentum is composed of an orbital and spin angular momentum. Torque can be exerted on objects in the trap if exchange of one, the other or both is achieved (Figure 1.12 A and B). Spin angular momentum change can be achieved with the use of birefringent particles [228, 229, 230, 231, 232, 233]. Upon passing through birefringent material, an extraordinary (parallel to the axis of anisotropy of the crystal) and an ordinary (perpendicular to the axis of anisotropy of the crystal) components of the light undergo different phase shifts. If this results in a change in the angular momentum of

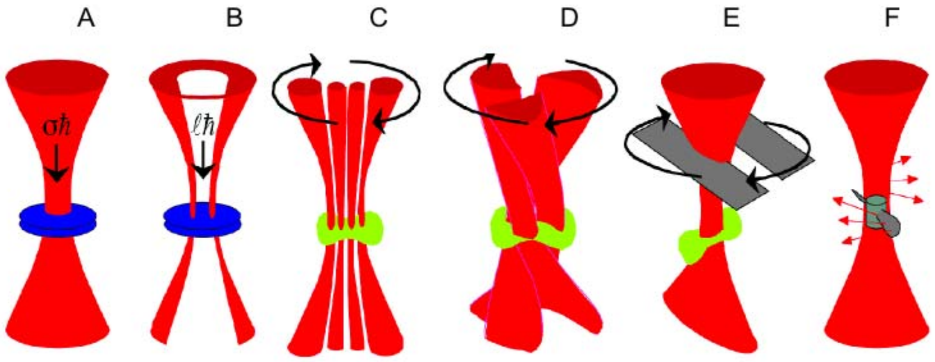

Figure 1.12: The various schemes employed to achieve rotation of a particle within optical tweezers: transfer of (A) spin and (B) orbital angular momentum to the particle, torque generated by the gradient force created by (C) rotation of a high order mode, (D) rotation of an asymmetric interference pattern or (E) rotation of an aperture and finally (F) the radiation pressure acting on propeller-shaped objects. Figure and the legend are taken from reference [210].

the light, the birefringent particle will 'feel' corresponding torque. The magnitude of the torque will depend on the angle describing the ellipticity of the light (α) and the angle between the fast axis of the elliptically polarized light and the optic axis of the birefringent material (β). For linearly polarized light the torque is dependent on β and the birefringent particle will be in stable equilibrium for β=0. If the plane of polarization of the light is rotated, the particle alignment follows the plane of the polarization. For circularly polarized light, torque will depend on α and will be constant for a given laser power, thus the particle will rotate at a constant speed [229]. Spin angular momentum change can also be achieved with asymmetrically shaped particles, also called shape birefringence. The principle is essentially the same except this time the different polarizabilities along the long and short axes of the particle are due to the particle shape rather than its molecular structure [234, 235, 236, 237]. Linear momentum, and orbital and spin angular momentum change, simultaneously, can be achieved with absorbing particles [238, 239]. For particles with high enough absorptivity, gradient forces are small, and they can not cause the trapping of absorbing particles. Instead radiation pressure forces (scattering forces) are dominant pushing the particles in the direction of the propagation of the light. But if the curvature of the light wavefront is such that it can be resolved into the radial inward force and force in the direction of propagation of the beam, then if an absorbing particle is constrained in the direction of the light propagation, it can be trapped two-dimensionally by the inward radial force. For this kind of trapping Gauss-Laguerre LG_{03} mode laser beams are usually used [240, 241, 242]. The LG_{03} mode laser beams carry orbital angular momentum and, if they are polarized, spin angular momentum. These will also be absorbed, and thus transfer of angular momentum from light to the particle allows the absorbing particle not only to be trapped in two dimensions, but also to be rotated [243]. Rotation within optical tweezers have also been reported. This can be achieved by rotating an asymmetric interference pattern or a higher-order laser mode, by the use of an elliptical beam or by rotating an aperture, and requires more complicated laser tweezing systems [244, 245, 246, 247]. The radiation pressure has been 'directed' in such a way as to rotate a particle, with the shape of that particle. These particles are different micro-fabricated chiral scattering particles that act as optical 'windmills' [248]. Despite the fact that torque can readily be exerted on microscopic objects with these methods, important drawbacks exist. The need for special micro-particles, like birefringent particles or a 'windmill' particle, limits the practicality of the method as well as potentially raising problems with attaching particles to rotary molecular motors. The techniques using energy absorption are limited due to heating, and the methods which rely on rotation within optical tweezers require more complicated trapping systems to generate specialized beams. Shaped particles and beams carrying orbital angular momentum have typical dimensions of several microns, thus the viscous drag on trapped particles limits the response time of these particles to changes in torque. Modulation of shaped beams generated by micro-mirror or liquid-crystal technologies also limits the time resolution of these techniques.

So, how does the system built during my DPhil research fit into the overall optical trapping field introduced above? How does it avoid the drawbacks of other techniques listed above? The design and layout of the system are described in details in the next chapter. Basically, the optical trapping system in itself has a few novelties but it is in principle very similar to the reported 'force clamps' and 'position clamps' [17, 15]. The novelties include use of a digital signal processor (DSP) board and a feedback algorithm designed for use on rotary motors ('angle clamp'). The first one is used to achieve required temporal resolution (I will discuss this further in the following chapter) and the second to impose minimal damage on rotary molecular motors (see Chapter 3 for full description). The main novelty is the handle, i.e. use of bead pairs instead of single beads. I will focus on explaining the resulting geometry and, optical torques and forces acting on the motor via a bead-pair, as well as giving a thorough account of the problems, limitations and, of course, capabilities of the system in subsequent chapters.

Chapter 2

MATERIALS AND METHODS

2.1 Optical trap

2.1.1 Requirements of the system

So far there has been one report of the use of optical tweezers to exert torque on a rotary motor, to measure the stall torque of the bfm [178], and two similar reports of the use of tweezers to study the properties of the bfm hook and filament [133, 132]. In these experiments torque was applied to the motor in the form of linear force on the trapped particle. This situation is analogous to tightening a nut with a spanner. The trap is like the hand holding the spanner, the cell body is like the spanner, and the opposing reactive force that completes the couple is generated by the link between the motor and the surface. Apart from these reports, optical tweezers have not been used as the technique of choice when applying external torque to rotary molecular motor. In the introductory chapter I have discussed and introduced both rotary motors of interest in this work. I have also introduced and listed the drawbacks of the methods so far used to apply torque to the rotary molecular motors, as well as the methods that can apply torque to microscopic objects and are yet to be applied on the rotary motors. In this chapter, I will describe the system built as part of this thesis and discuss how it overcomes some of the important drawbacks of other available techniques. Since high temporal and angular resolution is an important motivation for building this system, I will start here by summarising, in brief, experiments that answer the question: what is the temporal and angular resolution one requires when the goal is detailed studies of rotary molecular motors' energy profiles?

In the case of the bfm, previous experiments detected the angle and speed of polystyrene beads attached to the bfm [171, 173, 164] using mainly optical traps. The stepping motion of bfm has thus been resolved [164], with 26 steps per revolution. Beads of diameter 500 nm or 200 nm attached to the bfm via a filament stub rotate with a ∼100 nm radius [164], such that each 14° step corresponds to a linear step of ∼24 nm. To resolve steps in the bfm, motors were slowed to ∼10 Hz or below, corresponding to several milliseconds per step. Under physiological conditions steps in the bfm are likely to be 10 to 100 times faster [173].

In case of F_1, a 40 nm bead attached to the γ subunit rotates with a radius in the range of 25 to 60 nm [91], hence a 120° step corresponds to between 40 nm and 120 nm, and a 40° sub-step to between 13 nm and 40 nm. The larger 80° sub-step in F_1 rotation depends on ATP binding, and has a rate on the order of seconds for [ATP] in the nanomolar range. The smaller sub-step, however, is ATP independent and is separated by a dwell of several milliseconds from the larger [91, 92]. A recent report of rotation rates up to 721 Hz in F_1 from *E.coli* [249] indicates that average dwell times between steps in the enzyme rotation must be ∼0.5 ms.

Thus the temporal and spatial resolutions required to detect features of interest in the rotation of these motors are on the order of milliseconds and tens of nanometres respectively. The stall torques of 40-60 pNnmrad^{-1} generated by F_1 [91, 250], and up to 1000-2000 pNnmrad^{-1} by the bfm [173, 171]), set the scale of torque required to control these motors.

2.1.2 Optical trap layout

The instrument consists of a custom-built inverted microscope and two lasers for detection and trapping (Figure 2.1 and 2.2).

Bright-field imaging uses a high-power light-emitting diode (Luxeon Star LEDs, Alberta, Canada), high N.A. condenser (MEL 30920, Nikon, Japan) and objective (Plan Fluor 100x / 0.5-1.3 oil iris Nikon, Japan) and a high-sensitivity 1/2” Black and White CCD video camera (LCL-902K, Watec America CORP, Japan). The microscope stage was designed to be light and compact to minimize drift and vibra-

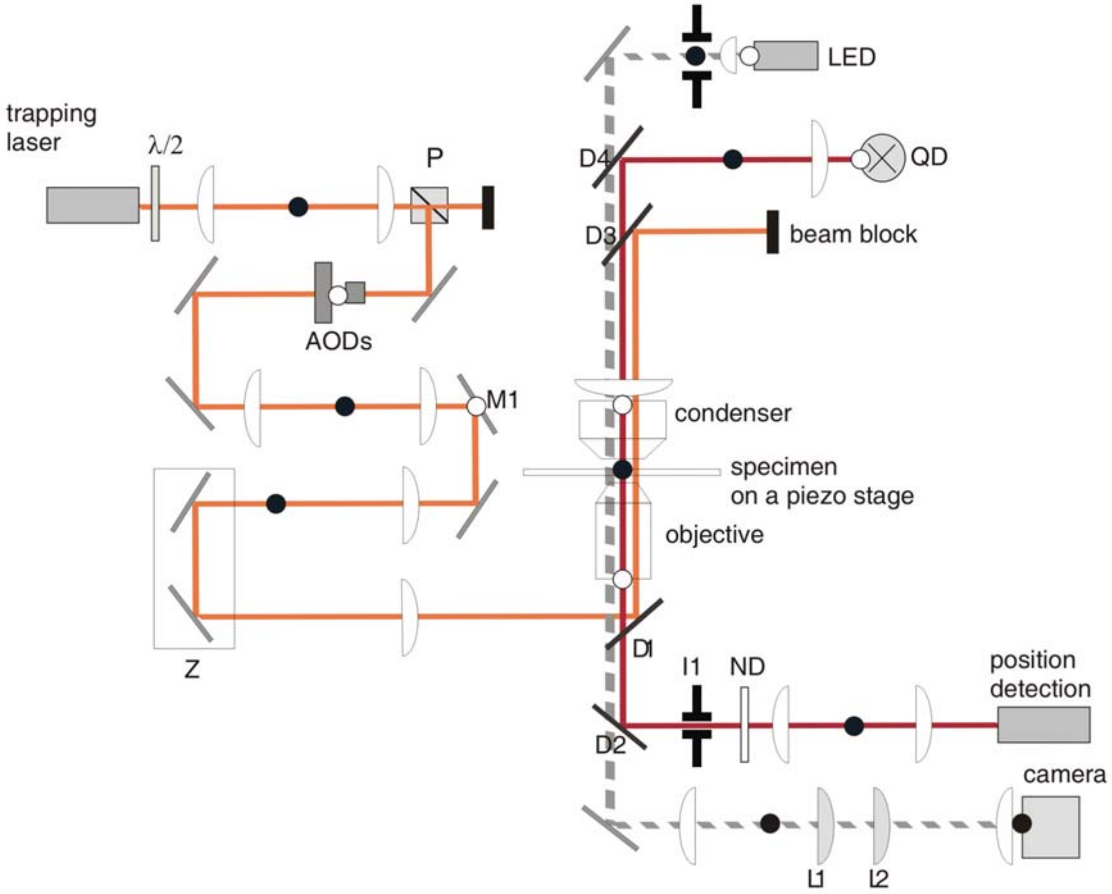

Figure 2.1: Schematic layout of the optical components in the system. The position detector laser beam is expanded to overfill the back aperture of the microscope objective. The width of the laser beam is additionally controlled with the iris I1, giving the option of setting different detector ranges at the expense of sensitivity. Detector laser power is controlled by iris I1 and neutral density filters, ND. After passing through the microscope objective and condenser, the detector laser beam is collimated and expanded to fill the quadrant diode (QD). The trapping laser passes through three pairs of lenses forming telescopes. The first set reduces the laser beam before entering the AODs, maximizing the response speed of the AODs. The other two expand the trapping laser beam to overfill the back aperture of the objective and create a plane conjugate to the back focal plane of the objective at the mirror M1 used for coarse steering of the trapping laser. The rail, Z, is used to adjust the trapping laser focus in the specimen plane. Lenses L1 and L2 give different magnifications of the image formed on the CCD camera. Planes conjugate to the specimen plane and to the back focal plane of the objective are marked with black and white circles respectively.

tion (Figure 2.3). Microscope slides holding specimens are attached to a metal plate mounted on a 3-axis piezo-electric stage (P-611.3S nanocube with E-664 LVPZT

Figure 2.2: Picture of the system shown in schematic layout of Figure 2.1.

Amplifier/Servo driver, 100 μm travel in x, y, z, 1 nm resolution, with a settling times of a few milliseconds, Physik Instrumente, Germany) which is in turn mounted on a lockable 3-axis dovetail stage (Newport, UK) for coarse positioning.

Position detection is by back-focal-plane interferometry [209] using a laser beam (Helium-Neon, 632 nm, 17 mW, Coherent, USA) focused into the specimen plane by the objective and collimated onto the face of a quadrant photodiode (UDT Sensors Inc., CA, USA), Figure 2.4. Optimal positioning was achieved by fine adjustment of the axial position of the QD so as to minimize sensitivity to movement of the condenser (Figure 2.5). After amplification, the QD signals are passed through anti-aliasing first-order pre-filters with time-constants ranging from 0.625 ms to 6.25 μs and digitized at an appropriate sample rate [251] as described below. The detector laser beam slightly over-fills the back-aperture of the objective, producing a diffraction limited focus in the sample plane. This maximizes detector sensitiv-

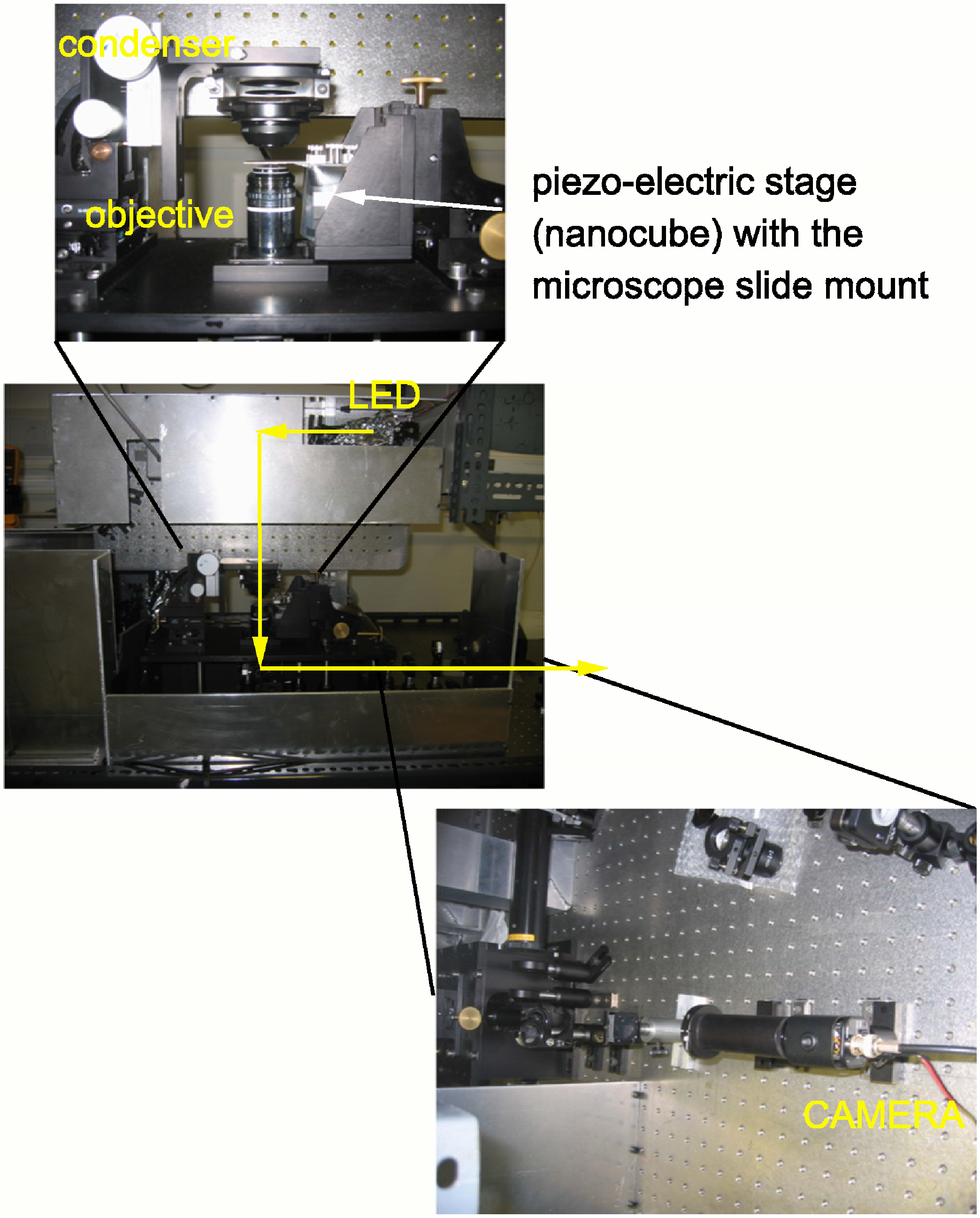

Figure 2.3: Custom-built inverted microscope. Top: Close-up of condenser, objective and piezo-electric stage (indicated with white arrow). The microscope slide mount is designed to be light and compact to minimize drift and vibration. Centre: Front view of the custom-built microscope. Yellow arrows indicate the light path through the microscope. Bottom, right: After passing through the objective light passes through several lenses for different image magnifications and reaches the camera (shown in top view).

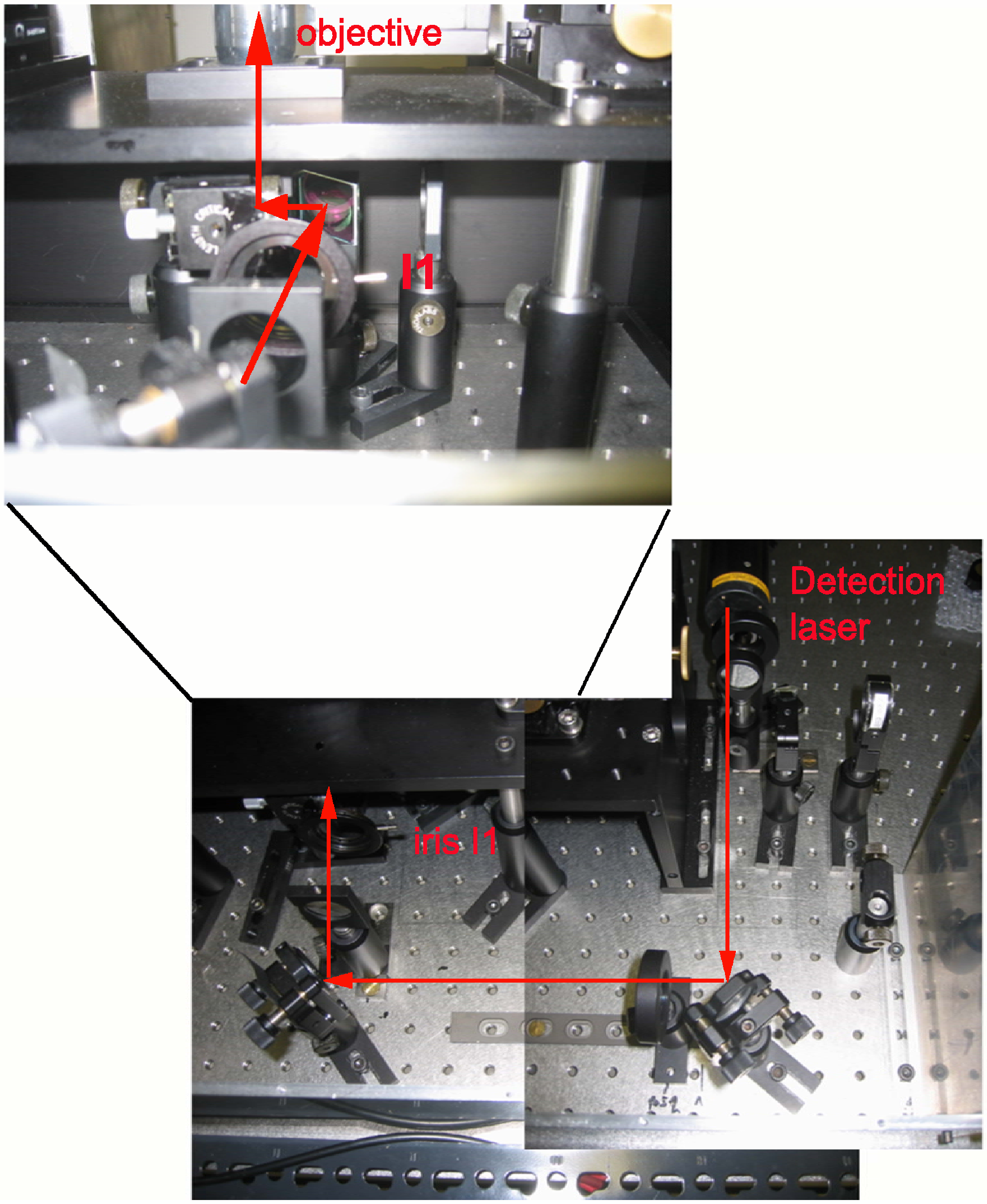

Figure 2.4: Detector laser trap. Bottom: Top view of the detector laser path (red arrows) is shown. Top: Close-up of the laser path as it reaches the back aperture of the objective. Iris I1, used for adjustment of the incoming detector laser beam size, is indicated.

ity but limits the detection range to approximately the laser wavelength. Detector range can be increased at the expense of sensitivity by reduction of the laser beam width using an iris (Figure 2.1 and 2.4 I1). The intensity of the detector laser is controlled by the iris aperture and neutral density filters, according to the requirements of particular experiments. Higher intensities give lower noise, but also increase laser damage to the specimen and optical trapping forces due to the detector laser.

The optical trap is formed by a near-infra-red Ytterbium fiber laser (1064 nm, PYL-3-LP, 3 W continuous-wave, IPG Photonics Corporation, MA, USA), collimated by the manufacturer, with <3% power fluctuation in 4 hours (Figure 2.6). The pointing fluctuations of this laser are ~2.5 μrad (rms) in 1 hour, with the spectral characteristics of white noise above ~30 Hz and $\frac{1}{f}$ noise below ~30 Hz. The

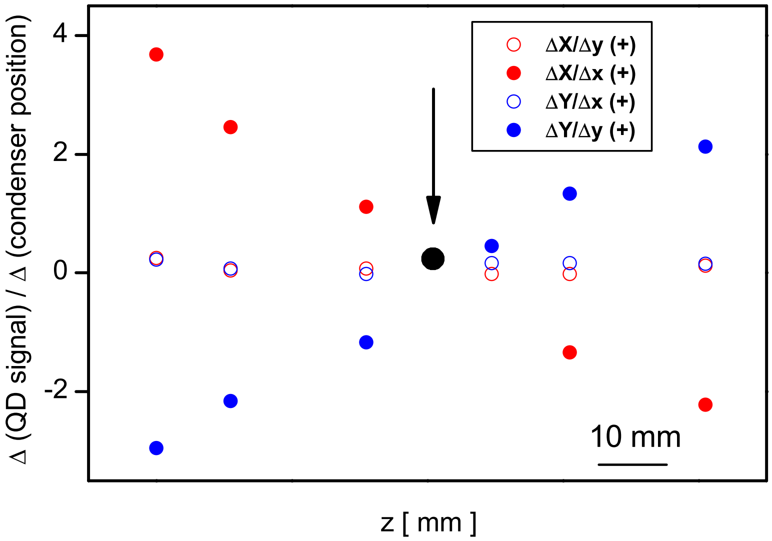

Figure 2.5: Determining the best axial position of the QD. After passing through the condenser, and a pair of lenses forming a telescope, collimated detector laser light reaches the QD. To determine the optimal axial position of the QD, the effect of moving the condenser in x and y on the QD signal (X, Y) was monitored, with the QD placed at six different axial positions. Black circle and an arrow indicate the axial position of the back focal plane of the condenser obtained from simple ray optics calculations. The QD signal X is not sensitive to changes of the condenser position in y, similarly QD signal Y is not sensitive to changes of the condenser position in x, for any of the indicated axial positions of the QD. However QD signal X is sensitive to the movements of the condenser in x, and QD signal Y to the movements of the condenser in y, for all axial positions apart from the one that corresponds to the position of the back focal plane of the condenser. Therefore the QD was placed at the back focal plane of the condenser.

intensity of the trapping laser was varied via the diode current and the combination of a half-wave plate and polarizing beam-splitter (Figure 2.6, $\frac{\lambda}{2}$ and P). Fine control of the trapping laser is achieved with acousto-optic deflectors ("AODs", AA.DTS.XY.250@1064nm, AA.DDS.60-90.XY driver, Opto-Electronique, France), positioned in a plane conjugate to the back focal plane of the objective. The centre drive frequency of the AODs driver is 75 MHz, with a 30 MHz bandwidth and 15.3 kHz resolution. This corresponds to angular range and resolution of 49 mrad and 24.9 μrad respectively. The AODs response time is 0.1 ms; corresponding to the time it takes for the radio-frequency acoustic wave to propagate a distance equal to the beam width in the acusto-optic medium. Initially the resolution of the DDS was significantly better, $\sim$300 Hz, however when DDS was controlled with the computer and the driving frequency changed faster then 1 s a fault was encountered. After 6-8 months with no replacement DDS the company returned the driver with the current characteristics explaining that they cannot achieve the stability needed to acquire initial driver resolution.

The entire instrument is mounted on an optical table in a temperature-controlled room. All experiments were carried out at 22°C. To quantify drift in the apparatus the following was measured; *(1)* drift in the detection laser optics by recording the position signal of a bead trapped several microns away from the cover slip surface with the detection laser, *(2)* drift in the trapping laser and detection laser optics by recording the position signal of a bead trapped several microns away from the cover slip surface with the trapping laser, and *(3)* drift of the stage by recording the position of a bead stuck to a coverslip. In all cases a bead of diameter 1 μm was used. In 1 hour, measured drift in the detector laser optics was $\sim$2 nm, and in the trapping and detector laser optics combined was $\sim$4 nm, compared to predicted $\sim$2 nm contribution from the measured trapping laser pointing stability. The stage drift was considerably larger, $\sim$1.5 nm/min, and was sensitive to occasional

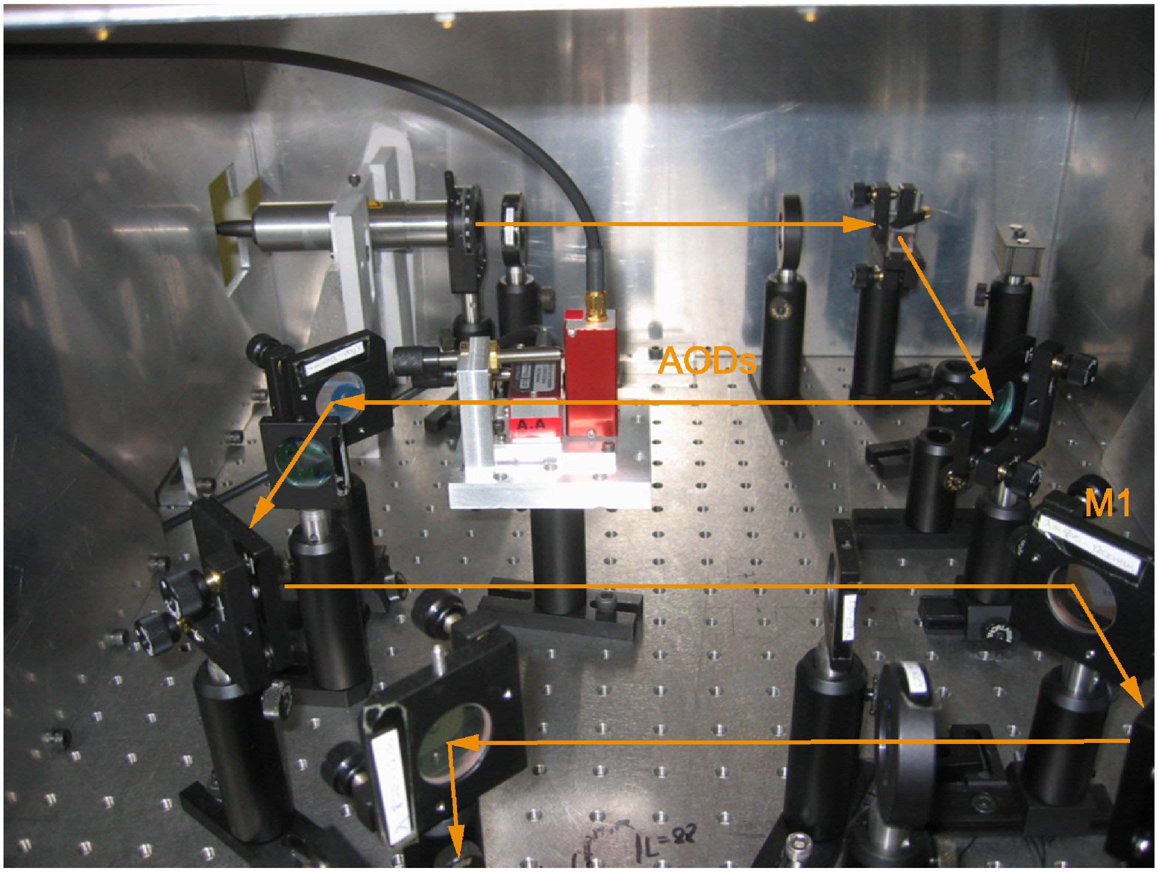

Figure 2.6: Trapping laser path (indicated with arrows). Mirror labelled as M1 is used for coarse adjustments of the trapping laser position in the specimen plane.

fluctuations in the temperature-control circuit of the room. At this stage it was not necessary to take further measures to reduce drift and instrumental noise [17], which are not expected to be limiting factors in experiments on rotary motors.

2.1.3 Data acquisition and control electronics

Data acquisition, feedback calculations and control of the optical trap are all performed by a digital signal processing board ("DSP", SI-C33DSP-PCI, 150MHz processor speed with SI-DSP6433R2-PCI daughter module, 16 analog input channels, 4 analog output channels, 16 digital channels, sampling rate up to 50 kHz, Sheldon Instruments, CA, USA) installed in a host computer (1.8 GHz processor, 1 GB RAM) running Windows 2000. Digital lines can be configured as either inputs or outputs and they are used as 8 individual lines and one word. Unfortunately of 16 digital lines several never worked (did not input or output signal). Also, when digital lines are used the output rate falls drastically and therefore only 4 analog output lines can be used with a satisfyingly high output rate. Although, I communicated extensively with the manufacturers this problem was never resolved. The Sheldon Instruments company was always very friendly but never very useful. On some occasions the encountered problems were solved with their help. Typically I found a way to bypass the problems which, in the case of not being able to use digital lines, reduced the performance of the system.

The board is programmed using a software package, QuVIEW, provided by the manufacturer. QuVIEW represents a set of Dynamic Link Libraries (DLLs) written in C/C++ that are incorporated into National Instruments graphical programming language LabVIEW as user libraries. The software package came with significant number of errors which were either interactively corrected in correspondence with Sheldon Instruments company, or bypassed by programming around the errors. QuVIEW DLLs are arranged in a specific sequence using LabVIEW. Once the LabVIEW program has been run the sequence is sent from the host computer to the board and the program continues running on the DSP irrespective of the host computer. Changes made in the LabVIEW program on the fly (on the host computer) will be sent to the DSP but the timing between the host and the DSP will not be controlled and will depend on other processes running on the host computer. To precisely time the events in QuVIEW, the DSPs clock is used via one of the QuVIEW DLLs. All the feedback programs on the DSP board (an example of a typical program written in QuiVIEW is given in Appendix A) were run at up to 10 kHz sampling rate unless otherwise stated. This is the maximum sampling rate at which the processor on the board can handle most of the feedback programs without ‘loosing’ data points, either when reading inputs or when outputting. The size of the feedback programs is larger then expected when purchasing this board, due to the faulty digital lines. The result of this was a need for analog to digital converter (the AODs driver has 15 digital controls for both X and Y). QuVIEW programs used just for bfp detection are significantly smaller and can be run up to the maximum DSP sampling rate, 50 kHz. Data acquired with QuVIEW are stored in QuVIEW specific format and later on converted into text or binary format using an adjusted version of a program supplied by the manufacturer. Analog output channels from the DSP daughter module are converted to digital for the AODs control by a custom-made 12-bit analog to digital converter (ADC). ADCs were designed and produced with the help of Central electronics workshop, Department of Physics, University of Oxford. Timing is based on the clock signal coming from the board. ADCs used were set to 0-20 V, to increase the noise margin (since the AODs driver has 15 digital controls for both X and Y, it was important to successfully convert as many bits as possible from each of the 4 analog channels). The DSP board outputs 0-10 V, thus first most significant bit of all 4 ADCs was set to 0. Also, 3 least significant bits of two ADCs and 2 least significant bits of the other two ADCs were set to zero. This gave 16 bits with 20 mV and 18 bits with 10 mV noise margin from all ADCs, which were subsequently arranged and sent to the AODs driver (a layout of the ADC board and bit arrangements is given in Appendix B). A maximum scan range and resolution are 27.5 MHz and 15.3 kHz, respectively, corresponding to 44.9 mrad and 24.9 μrad beam deflection and 16.5 μm and 9 nm displacement of the optical trap. However, the feedback programs which aim to achieve as high bandwith as possible use a maximum range of 3.9 MHz, corresponding to maximum displacement of the optical trap $\sim$2.6 μm (minimal resolution stays the same). Calculations on the DSP board needed to obtain the required signal for analog to digital conversion in this range are much shorter. Where a larger maximal displacement is needed, feedback bandwidth needs to be sacrificed. The 'analog lines on the DSP→ADC→DDS' scheme described above, as well as the temporal and spatial resolution of the system are not optimal. It is a result of faults encountered when using the DDS and the DSP. A new DSP from the same company has been purchased, with a 300 MHz processor (which should speed up the execution of programs 2 to 5 times), 36 working digital output lines and 8 working analog output lines with the same number of input lines. When the time resolution of the current system is no longer satisfactory, this new DSP and AODs with a faster response time can be fitted to further increase it.

2.1.4 Laser damage to biological samples

Choice of laser wavelengths was determined by the following factors. The trapping laser was chosen for low cost, high power and relatively low levels of laser-induced photodamage to biological samples at this wavelength [252]. The shorter wavelength of the detector laser allows a smaller focussed spot and therefore improved detector sensitivity, especially for beads with diameters below about 500 nm. It also avoids potential difficulties with effective low pass filtering (8-9 kHz) that can occur with silicon photodiodes and 1064 nm lasers [253, 251]. Photodamage caused by the detector laser was characterized by recording laser-induced changes in the speed of a bead attached to a rotating flagellar filament of *Escherichia coli* [173] over the range of laser powers used (20-150 μW in the objective back-focal-plane). Using a speed reduction of 5% to define a threshold for laser damage, I was able to record for 1.5 to 2 min at 150 μW and for 5 to 10 min at 20 μW before observing any laser damage. By contrast, previous work has shown that similar speed recordings using a laser at 1064 nm can be extended for hours without observable laser damage [171]. The instrument can be adapted for extended observations by using the trapping laser for detection, which can easily be achieved by swapping dichroic mirrors D3 and D4 (Figure 2.1) or by the use of singlet-oxygen scavengers (the observation time can be increased up to 10 min at 2 mW, personal communicaton with Dr. Yoshiyuki Sowa). Protein motors such as F_1 are typically less sensitive to photodamage than live cells, and can be protected by the addition of singlet-oxygen scavengers if necessary [54].

2.2 Bead pair preparation

CONTRIBUTIONS AND COLLABORATIONS:

Final stages of bead pair preparation protocol were developed together with Thomas Bilyard, a DTC student as part of his two months project in Dr. R. Berry's group.

Amino-functionalized, biotinylated, plain (diameter 500 and 200 nm, Polysciences, Germany), as well as carboxy-functionalized (diameter 350 nm, Bangs Laboratories, USA) polystyrene microspheres were used. Biotinylated microspheres (beads) were prepared by modification of amino-functionalized and carboxy-functionalized beads as follows. Amino-functionalized beads, 1% by volume, were incubate for 2 hours at room temperature with rolling, in 100 mM sodium bicarbonate buffer pH=8.05 plus 2 mM 6-(biotinamidocaproylamido)caproic acidin-hydroxysuccinimide ester (Sigma-Aldrich, UK) added as 100 mM stock in dimethyl sulfoxide (Sigma-Aldrich, UK); followed by resuspension in storage buffer (10 mM HEPES/NaOH pH=7.8). Carboxy-functionalized beads, 1% by volume, were incubated for 2 hours at room temperature with rolling, in 50 mM 2-morpholinoethanesulfonic acid-KOH, pH=5.5 plus 200 μM 1-ethyl-3-(3-dimethylaminopropyl) carbodiimide (EDAC) and 2 mM (+)-biotinyl-3, 6-dioxaoctanediamine (Biotin-PEO-amine). Biotin-PEO-amine was added as 100 mM stock in DMSO, and EDAC as a 10 mM stock in water. After incubation beads were resuspended in storage buffer.

Bead pairs were prepared by incubating beads in media with high salt concentrations, which is assumed to collapse the Debye layer and allow beads to stick to each other by van der Waals interactions. 100-340 mM KCl was used for plain polystyrene beads and 200-500 mM $MgCl_2$ for biotinylated amino and carboxy beads, both in storage buffer. Bead concentrations were between 0.5% and 2% by volume. After adding salt, beads were sonicated for 4-30 min, washed 3 times in storage buffer and stored at a final concentration of ~0.5%. The number of bead pairs formed

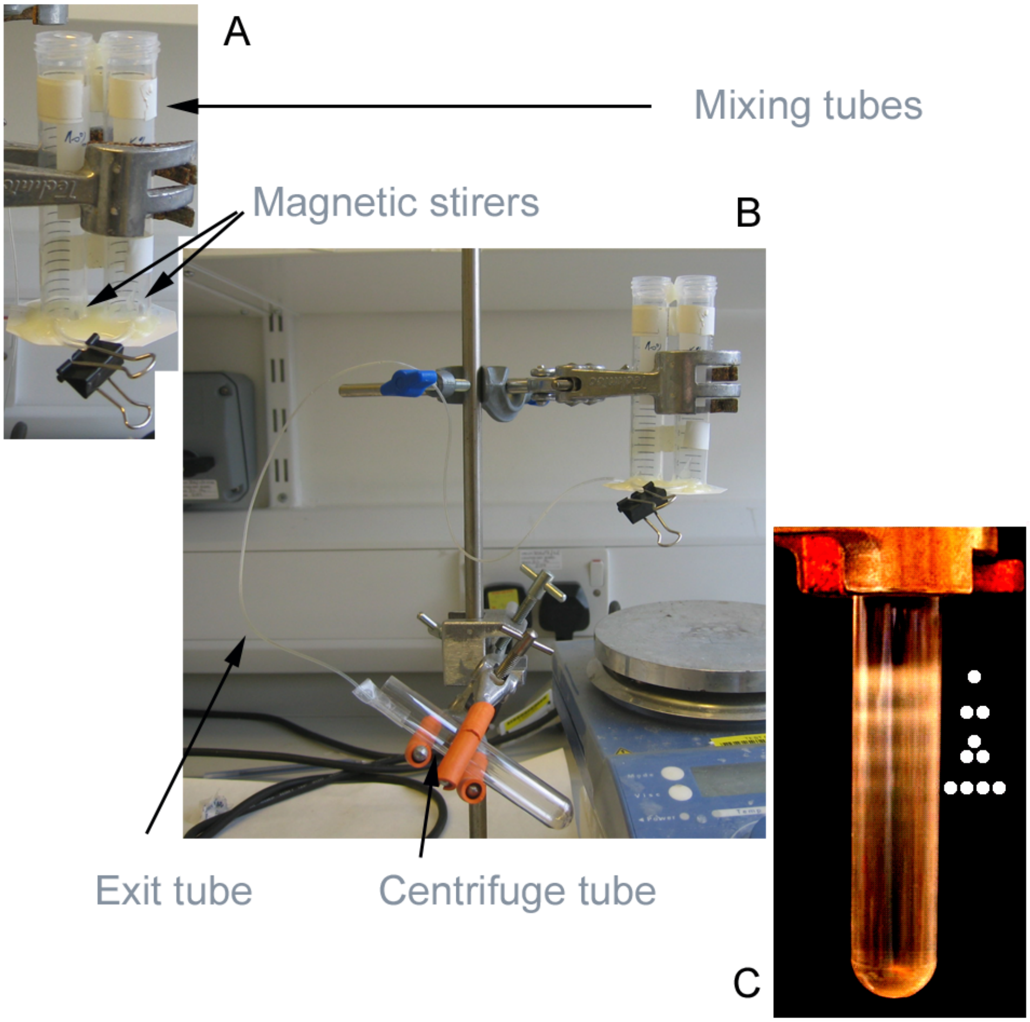

Figure 2.7: (A) Home made gradient mixer, with the mixer tubes clamped. (B) Exit tube of gradient mixer is indicated and centrifuge tube in which sucrose gradient is formed shown. (C) Bands of bead clusters of different sizes (singles, pairs, triples and quadrupls are indicated). Figure C was taken by Thomas Bilyard.

was estimated by direct observation in the microscope. Immediately after washing 10-15% of all objects in the solution were bead pairs, which is consistent with the maximum number of pairs predicted by modelling bead aggregation as a simple second-order process with equal rate constants for all interactions, in which single beads combine to form pairs and all other interactions lead to clumps containing more than 2 beads. The fraction of bead pairs did not change after storage for a month.

The bead pairs were separated from single beads and clumps containing more than

2 beads by sucrose gradient centrifugation. Sucrose gradients were prepared with a home made gradient mixer (Figure 2.7 A) in the following way: *(1)* The gradient mixer was setup on a stand as shown in Figure 2.7 B with magnetic stirrers free to rotate. *(2)* Both the mixing tubes and the exit tubes were clamped prior to use and 5 ml of 5% and 10% sucrose were added to the mixing tubes. *(3)* A small amount of BSA in water was added to the centrifuge tubes (Figure 2.7 B) and collected to ensure that the sucrose is flowing smoothly down the centrifuge tube and prevent mixing that might destroy the gradient. The centrifuge tubes were placed about 10 cm below the mixer. *(4)* The clamps were removed from the mixing tubes and the ends of the exit tube secured on the inside of the centrifuge tube such that bubbles of sucrose do not form and a slow continuous flow is the result. *(5)* After the gradient was formed beads were carefully loaded into the top of the gradient. This proved to be a very important step, so adequate care was taken to ensure that the pipette is in contact with the top of the sucrose gradient and that the flow is very slow and across the top of the sucrose (not directly into it). *(6)* Beads were centrifuged for 15, 25 or 40 min for 500, 350 and 200 nm biotinylated beads, respectively, at 12 256g using the JS13.1 rotor in a centrifuge J2-21 (Beckman, UK). The centrifuge is located in Micro-Biology Unit, Department of Biochemistry, University of Oxford. Centrifuge, rotor and the tubes were chosen as the best option for the gradient centrifugation of $\sim$500 nm particles, as well as for extraction of bead pairs after centrifugation. No adequate adaptor exists for this tube-adaptor-rotor-centrifuge combination; therefore, additional home made adaptors were made. *(7)* Beads were extracted and washed 2 times into storage buffer (Figure 2.7 C). Immediately after gradient separation 60-80% of all objects in the solution were bead pairs. For a maximum yield of bead pairs, sucrose gradient centrifugation is performed just prior to use.

2.3 Bead pair assay preparation

Biotinylated bead pairs were attached to the surface of a coverslip as follows. The coverslip was cleaned with saturated KOH in 95% ethanol prior to use. A tunnel slide was constructed using double-sided adhesive tape to define a channel between the coverslip and a microscope slide (Figure 2.8), filled with KA buffer (10 mM MOPS/KOH, 2 mM $MgCl_2$, 50 mM KCl, pH=7) containing 6 mg/ml Bovine Serum Albumin (Sigma- Aldrich, UK) and incubated for 1 min. 4 μM streptavidin (Sigma-Aldrich, UK) in KA buffer was then added and incubated for 10 min. After washing with KA buffer, 0.5% biotinylated bead pairs in KA buffer were added and incubated for 10 min. After incubation, loose beads were washed out and the tunnel sealed with vacuum grease.

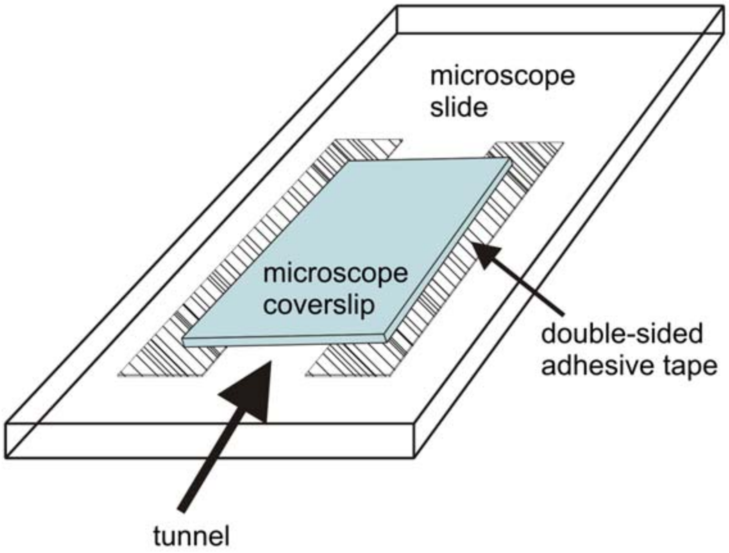

Figure 2.8: A tunnel slide constructed out of a microscope slide, double-sided adhesive tape and a microscope coverslip (22 x 22 x 0.35 mm). The coverslip is placed closer to the edge of the microscope coverslide to fit in home made microscope and microscope stage shown in Figure 2.3

2.4 F_1-ATPase purification

E.coli **F_1-ATPase purification** is based on protocols obtained from Professor Masamitsu Futai.

CONTRIBUTIONS AND COLLABORATIONS: Protocols, as done in Prof. M. Futai's lab, were learned, working with Hiroyuki Howokawa, in November 2003 during a 3 week stay at Division of Biological Sciences, Institute of Scientific and Industrial Research, Osaka University. Protocols as well as relevant strains were brought from Japan to Oxford and adequately adopted. This, as well as purchasing all relevant chemicals, involved adjusting the protocols to best suit the available equipment, in terms of centrifuges, rotors, centrifuge tubes and adaptors, French press cells and warm baths. The work was done initially in Prof. Judy Armitage's lab in Micro-Biology Unit, Department of Biochemistry, University of Oxford together with two undergraduate students, Jelena Baranovic and Maja Petkovic*. Due to lack of space the work was continued in Prof. Anthony Watt's lab, Department of Biochemistry, University of Oxford. Adequately adopted protocols are currently performed when F_1-ATPase is required for rotation assay experiments by Dr. Simon Ross, an IRC (Interdisciplinary Research Collaboration) technician working in Prof. Anthony Watt's lab.

F_1, with six histidine residues intorduced in front of the initiation codon of the α subunits genes and two cystine mutations in γ subunit, was constructed in pBUR17 plasmid and expressed in DK8 bacterial strain by Dr. H. Omote as described previously [254, 255]. The F_1 was purified in four steps (each taking $\sim$ one day) as shown in Table 2.1. The first two steps involve cell growth, wich yield a cell pellet of $\sim$1 g. At the end of the third step, disrupted cells are collected as membrane fragments containing F_1F_o as well as other membrane proteins. During the fourth step F_1 is separated from F_o and collected by glycerol gradient centrifugation.

---

*J. Baranovic and M. Petkovic, worked on their diploma thesis each for two months, as part of their undergraduate degree at University of Zagreb, Department of Molecular Biology. They were financed for their stay by city of Zagreb through NGO znanost.org and program Connect (of which I am the program leader).

Day	*Purificationstep*	*Finalproduct*
Day 1	Cell preculture	8 ml of preculture
Day 2	Cell culture grown in glycerol reach growth medium	Cell pellet of ~1 g
Day 3	Cell membrane isolation	Membrane fragments containing different proteins (including F_1F_o-ATPase)
Day 4	Glycerol gradient purification of F_1-ATPase protein	F_1-ATPase

Table 2.1: F_1-ATPase purification protocol

(1) Cells were grown in 20 ml Luria-Bertani (LB) medium with 100 μg/ml final concentration of ampicilin for 12-15 hours, with 120 rpm shaking speed and bath temperature of 37°C.

(2) 800 ml of Tanaka medium was inoculated with 8 ml of overnight preculture (64 mM K_2HPO_4, 34 mM KH_2PO_4, 20 mM $(NH_4)_2SO_4$, 1 μM $FeSO_4$, 10 μM $CaCl_2$, 10 μM $ZnCl_2$, 50 mg/l L(+)-Isoleucin, 50 mg/l L-Valine, 2 mg/l Thiamine-HCl, 0.3 mM $MgCl_2$, 100 μg/ml ampicilin, 0.5% (w/V) glycerol) and incubated with shaking speed of 160 rpm and bath temperature of 37°C. The culture was grown until OD_{600} (optical density, i.e. the absorbance of the cell culture measured at 600 nm wavelength) became ~1.0. The culture was then centrifuged for 22.5 min at 6 000 g average at 4°C (JLA 9.1000 rotor for Beckman Coulter centrifuge, 6300 rpm average). The cell pellet was resuspended in 50 mM Tris-HCl (pH=8.0 at 4°C), using 200 ml per 800 ml Tanaka medium, and centrifuged for 22.5 min at 6000g average at 4°C, as above. The pellet was resuspended with TKDG buffer (20 mM Tris-HCl

pH=8.0 at 4° C, 140 mM KCl, 10% (w/V) glycerol, 0.5 mM DTT), using 20 ml per 800 ml Tanaka medium and centrifuged for 11.5 min at 6000g average at 4° C (JA 12 rotor for Beckman Coulter centrifuge, 7000 rpm average). Cell pellet wet weight after centrifugation was measured.

(3.) *E. coli* cells were resuspended in TKDG-a buffer (TKDG buffer with 0.5 mM PMSF (Sigma-Aldrich, UK), 5 μg/mL leupeptin (Sigma-Aldrich, UK), 5 μg/mL pepstatin A (Sigma-Aldrich, UK) and 1 μg/mL DNase I) at 7 ml of buffer per 1 g cells (wet weight) and disrupted with a French Press (SIM AMINCO, SLM Instruments Ltd.). Gauge pressure was set at 1800 kg/cm^2 to achieve $\sim$ 28 000 psi when using a 40k pressure cell. When using a 20k pressure cell, gauge pressure was set to 1200 kg/cm^2, actual pressure was $\sim$19 000 psi. Disrupted cells were centrifuged two times for 12.5 min at 12 000g average, at 4°C (JA 20 rotor for Beckman Coulter centrifuge, 12 000 rpm average). Supernatant was transfered to fresh tube and centrifuged for 1.5 hr at 130 000g average, at 4°C (Type 70.1 TI rotor for 43 500 rpm in L-XP Beckman Coulter ultracentrifuge). The precipitate was resuspended on ice in TKDG-b buffer (TKDG-a buffer without DNase I) and centrifuged again for 1.5 hour at 130 000 g average, at 4°C as before. The precipitate was resuspended on ice in TKDG buffer (approximately 200 μl/1 g cells (wet weight)).

(4.) The suspension of membranes was diluted about 50 times with TKDG-E buffer (TKDG buffer with 1 mM Ethylenediamine-N,N,N',N'-tetraacetic acid (EDTA), 5 g/ml Leupeptin and 5 g/ml Pepstatin A), and centrifuged for 1 hour at 150 000 g average, at 15°C (rotor Type 70.1 TI at 46 700 rpm in ultracentrifuge L-XP Beckman Coulter). The precipitate was rinsed with 1 ml per 1 g of cells of buffer A (1 mM Tris-HCl pH=8.0 at 25°C and 0.5 mM EDTA) carefully and quickly, suspended in 0.6 ml per 1 g of cells (wet weight) of buffer A and centrifuged two times for 20 min at 370 000 g average, at 15°C (rotor TLA 100.2, 100 000 rpm, Optima TL ultracentrifuge). 0.5 M MOPS-NaOH buffer (pH=7.0, at 25°C) and 1 M Na_2SO_4 were

added to the supernatant to final concentration of 25 mM and 50 mM, respectively. After the pH of the solution was checked to be 7.0, 20 mM Biotin-PEAC$_5$-maleimide (Sigma-Aldrich, UK), 10 mg/ml Leupeptin and 10 mg/ml Pepstatin A were added to final concentrations of 100 μM, 10 μg/ml and 5 μg/ml respectively. The solution was incubated for 1.5 hour at room temperature. After the biotinylation, the solution was layered on a glycerol gradient (prepared in ultra centrifuge tubes by layering 30, 25, 20, 15 and 10% (w/V)) glycerol solutions (in 20 mM MOPS-NaOH pH=8.0 at 25°C, 50 mM Na_2SO_4, 1 mM ATP, 5 μg/ml Leupeptin and 5 μg/ml Pepstatin A) and centrifuged for 4 hr at 250 000g (average), at 15°C. (SW 55 Ti rotor, 51 300 rpm average, Optima L-XP Beckman Coulter ultracentrifuge). After centrifugation the solution was fractioned. To determine the peak fraction, the ATPase activity of fractions was checked. Peak fraction was aliquoted and fast frozen for storage at -80°C (a gel of peak fractions is shown in Figure 2.9). Protein concentration was

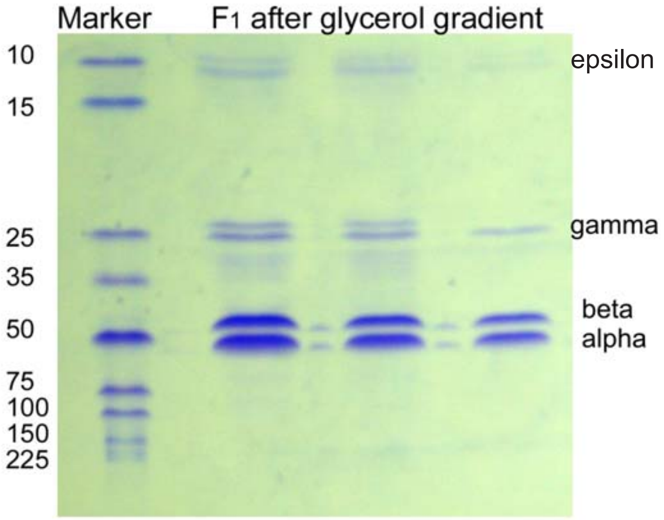

Figure 2.9: SDS-PAGE gel of peak F_1 fractions after glycerol gradient purification. Weights of marker proteins and positions of α, β and γ units of F_1 are indicated. Small amounts of ϵ subunits are also present as indicated.

obtained using the Bradford and Lowry methods, and ATPase activity was tested by P_i coloring method.

The Bradford method is based on an absorbance shift in the Coomassie dye when it is bound to arginine and hydrophobic amino acid residues present in the protein of interest. The increase in absorbance at 595 nm is proportional to the amount of bound dye, and thus to the amount of protein present [256].

The Lowry method was used to estimate the amount of membrane bound protein. Divalent copper ions, under alkaline conditions, form a complex with peptide bonds in which they get reduced to monovalent ions. Monovalent copper ions and tryosine, tryptophan and cysteine R-groups react with the Folin reagent to form an unstable product that gets reduced to molybdenum/tungsten blue. The amount of product is proportional to amount of protein and can be detected by absorbance at 650 nm [257].

ATPase activity by coloring: The assay measures a formation of phosphate by hydrolyzing ATP. The method depends on quantifying the color obtained from the formation of a phospho-molybdate complex and its subsequent reduction to highly colored blue compounds [258].

The yeast mitochondrial F_1-ATPase

CONTRIBUTIONS AND COLLABORATIONS: The enzyme was genetically modified for rotation assays and purified in laboratory of Professor David M. Mueller, Laboratory of Molecular Bioenergetics, Department of Biochemistry and Molecular Biology, The Chicago Medical School.

A 6-His tag was introduced on each of the β subunits and a cys mutation in the γ subunit.

2.5 F_1-ATPase rotation assay preparation

Both *E.coli* F_1 and yeast F_1 were attached to the surface of a coverslip prepared in on of the following ways.

CONTRIBUTIONS AND COLLABORATIONS: The F_1-ATPase rotation assay preparation was done together with Thomas Bilyard, a DTC student who after finishing his two month DTC project joined Dr. Richard Berry's group as Dphil student and started working on F_1-ATPase.

Microscope coverslips were

- cleaned as described for bead pair assay and coated with BSA (BSA surface)
- cleaned as described for bead pair assay and coated with nitrocellulose (Collodion Solution, Sigma-Aldrich, UK) and 1 μM Ni-NTA Horseradish-peroxidase (HRP, Qiagen, UK) (HRP surface)
- cleaned as described for bead pair assay and functionalized with 2%(3-Mercaptopropyl)trimethoxy silane and 50 mM DTT in 10 mM MOPS/KOH pH=7.5, prior to reaction with 10-15 mg/ml maleimide-C3-NTA (Dojindo, Japan) in 10 mM MOPS/KOH pH=7 and 10 mM $NiCl_2$ in 10 mM MOPS/KOH pH=8. [109, 90] (silane surface)
- Cu^{2+} chelated coverslips from Microsurfaces Inc, USA were used. These are made from a proprietary coating, consisting of a high density poly-ethylene-glycol (PEG) brush, which is further functionalized with Cu^{2+} as shown in Figure 2.10 (Cu^{2+} surface)

Microscope coverslips were then assembled into tunnel slides as described for bead pair assay.

The following were flowed through the channel: 1 to 0.2 nM F_1 in KB buffer (KA

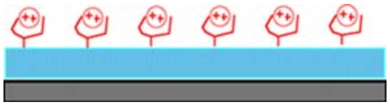

Figure 2.10: Cu^{2+} coated surface. PEG brush is shown in blue. Figure is taken from company's webpages (Microsurfaces Inc, USA http://proteinslides.com/product.html).

Buffer, 5 mg/ml BSA, pH=7), wait 10 min; KB buffer; 4 μM streptavidin (Sigma-Aldrich, UK) in KA buffer, wait 10 min; KB buffer; 0.5% biotinylated bead pairs in KB buffer, wait 10 min; KB buffer; 24 mM, 1 μM, 60 nM or 20 nM Mg-ATP in KB buffer (Reaction Mixture). For 1 μM, 60 nM or 20 nM [Mg-ATP] following ATP regenerating system was used to keep the [ATP] constant: 10 nm/ml PK and 100 mM PEP. At these concentrations oxygen scavengers were used as well (0.5% β-mercapthoethanol, 25 mM glucose, 36 μl/ml catalase, 4.24 mg/ml glucose oxidaze) were included in the Reaction Mixture (RM). To prevent evaporation, the tunnel was sealed with vacuum grease. The rotation assay preparation given above is a final result of several attempts to determine the buffers and concentrations which gave the highest yiled of functional surface immobilized complexes. These include

- For incubation in the channel the concentration of F_1 was varied between 10 and 0.1 nM . If every F_1 molecule present in the 22 x 3 mm^2 channel gets attached to the coverslip surface, a 10 nM concentration of F_1 will give $\sim$ 9000 molecules/μm^2 and 0.1 nM concentration will give $\sim$ 90. Concentrations of F_1 between 1 and 0.2 nM were chosen as the most suitable, with F_1 complexes well distributed on the surface and bead pairs present in good numbers.

- F_1, streptavidin and bead-pair incubation was tried with FB buffer (10 mM HEPES/NaOH pH=7.8, 6 mM $MgCl_2$, 25 mM KCl, 5 mg/ml BSA) as well as KB. FB buffer is often used in rotation assays reported by other researchers and was therefore tested [58]. Casein was used instead of BSA in both KA and FA (FB buffer without BSA) buffer. Concentration of BSA and casein was varied from 0.25 mg/ml to 10 mg/ml in both KA and FA buffer. It was found that incubation in KA gives the highest number of spinners and almost no non-specific sticking for the 500 nm biotinylated amino-functionalized bead-pairs.

- Neutravidin (Pierce, USA) was used in stead of streptavidin to try and improve specific stickiness and minimize non-specific sticking, as well as to reduce the off rate compared to streptavidin and avidin [259]. No significant improvement was found.
- Amino functionalised 500 nm beads from Polysciences (Germany) gave almost no non-specific sticking when biotinylated and used in KB buffer. Carboxy functionalised beads from different manufacturers were tried (Bangs, USA and Polysciences, Germany), each having different charge and slightly different size (all in the range from 300 to 350 nm). In KB buffer, biotinylated 350 nm (Polysciences) carboxy-functionalized beads gave no non-specific sticking. Also, biotinylated 200 nm amino functionalized beads from Polysciences were found to give low non-specific sticking when used in KB buffer.

2.6 *E. coli* rotation assay preparation

CONTIRBUTIONS AND COLLABORATIONS: The data presented in section 4.3.2 was obtained from C. J. Lo for the purpose of demonstrating the capabilities and different uses of the trapping system.

Cells of *E. coli* strain KAF95, expressing flagellar filaments that spontaneously stick to plain polystyrene beads and flagellar motors that do not switch direction and cells of *E. coli* strain KAF84, expressing flagellar filaments that spontaneously stick to plain polystyrene beads and flagellar motors that switch direction were used [260]. 5 ml of tryptone-broth was inoculated with 100 μl of cells (TB; 1% tryptone, Difco, USA; 0.5% sodium chloride) and 5 μl of 100 μg/ml ampicillin (Sigma-Aldrich, UK) then grown for 5 hours at 30°C with shaking at 200 r.p.m. [260]. Tunnel slides were prepared as described for the bead pair assay. Poly-L-lysine (Sigma-Aldrich, UK) was incubated in the tunnel for one minute and washed with motility buffer (10 mM potassium phosphate; 0.1 mM EDTA at pH=7.0). Prior to use, flagellar filaments were sheared by passing the cell culture through a home made shearing device made of two syringes with narrow gauge needles connected by polyethylene tubing. The turbulent flow inside the needle is sufficient to shear the flagella at a random point along the filament. Cells were sheared 40-70 times [174]. Cells with trunctuated filaments were incubated in the tunnel slide for 10 minutes. Motility buffer was subsequently added to the tunnel, after which 0.5% solids concentration 500 nm diamtere beads (Polysciences, Germany) in motility buffer were added and incubated for 10 min. After incubation loose beads were washed with motility buffer and the tunnel was sealed with vacuum grease.

In section 4.3.2, C. J. Lo used YS34 strain containing pYS13 and pYS11 plasmids, and flowed the following through the channel: poly-L-lysine, wait 1 min; sodium motility buffer (motility buffer with 85 mM NaCl); cells with truncated filaments, wait 10 min; 0.5% solids concentraion 350 nm or 200 nm beads (Polysciences, Germany), wait 10 min; sodium motility buffer. The channel was subsequently sealed with vacuum grease.

CHAPTER 3

FEEDBACK

3.1 Overview

Having described the setup built as part of this thesis in the previous chapter, here I present the feedback algorithms used and demonstrate the performance of the 'angle clamp' system. I give a brief introduction to the feedback theory, which helps to understand the limits of the system in terms of temporal resolution. I then present experiments performed on a single bead and a bead-pair, with details of the experimental procedures developed for each particular feedback algorithm.

3.2 Feedback theory

In order to understand the limitations and expected performance of the feedback system I take a short look at the underlying theory and present algorithms chosen for use in the experiments.

The equation of motion of a trapped object in the system presented here is given as [261]

$$\zeta \frac{dx}{dt} = -k[x(t) - u(t)] + f_b(t) \tag{3.1}$$

where $u(t)$ is the feedback control term (for this system the position of the trapping laser), which can have different forms depending on the chosen algorithm. Without this term, Equation (3.1) represents a Langevin equation where k is the trap stiffness, $x(t)$ the position of the object in the trap, ζ the viscous drag coefficient of the bead and $f_b(t)$ the Brownian force due to thermal fluctuations. If $u(t) = 0$, the power spectrum of the system in Equation (3.1) is a Lorentzian [262]. At low frequencies it asymptotically behaves as white noise, while at frequencies above the cut-off frequency f_c, it asymptotically decays as $1/f^2$. The aim of a feedback algorithm is to make the system output, $x(t)$, follow a control signal, $r(t)$. The general strategy as described in [261] minimizes the error-signal $e(t) = r(t) - x(t)$ by choosing a suitable control law $K(t)$, where $u(t) = u(K(t), e(t))$ in Equation 3.1.

The most frequently used control law is

$$u(t) = K_p(t)e(t) + K_i \int e(t)\,dt + K_d \frac{de(t)}{dt}; \quad K_p, K_i, K_d = const. \tag{3.2}$$

known as the proportional integral derivative (PID) feedback control law.

In the case of the derivative term, the response is linear with frequency and high frequency Brownian noise can strongly influence the performance of the feedback. Therefore, K_d is usually set to zero (PI feedback). A proportional feedback term K_p is sufficient to reduce fluctuations in $e(t)$ below a certain cut-off frequency f_{K_p}, which is higher than f_c. However, the long-term response with only the proportional term differs from a desired set-point as discussed elsewhere [261]. This steady state error is eliminated by an integral feedback term. In addition, with the integral term, the response time of the system is increased [261] and the system changes from first order to second order, where the system bandwidth and damping is influenced by the feedback coefficients K_i and K_p.

When discussing the feedback bandwidth and stability of the system, the delays introduced when the feedback loop is implemented digitally have to be factored in. To correctly describe the system, Equation 3.1 is discretized

$$\zeta \frac{(x_{n+1} - x_n)}{T_s} = -k(x_n - u_n) + f_{bn} \tag{3.3}$$

where $T_s = \frac{1}{f_{sampling}}$. The control law in discrete form can be written as

$$u_n = K_p(r_n - x_n) + K_i \sum_{j=0}^{n} (r_j - x_j) + K_d((r_n - x_n) - (r_{n-1} - x_{n-1})) \tag{3.4}$$

with K_d usually set to 0.

Further time delays are present in the system due to the AODs response time (the time it takes for the acoustic wave to reach and cross the laser beam), and to the delay between the input and output signals on the DSP board, corresponding to computational time of the board (which depends upon the size of the program used to run the feedback). These delays and the parameters k, ζ, K_p and K_i set the feedback bandwidth of the system. The maximum frequency up to which the feedback can reduce $e(t)$ is usually significantly less than the sampling frequency $f_{sampling}$ [263]. Simple calculation for an analog first order system such as Equation 3.1 as given in [261], with the effect of delays taken into account, suggests that the maximum frequency up to which the feedback can reduce Brownian noise is approximately one quarter of the overall feedback execution frequency, f_{loop}. Spontaneous oscillation occurs at this frequency when K_p and K_i are increased beyond a critical point. This prediction was compared with experiments presented later in the text, and found that it gives a rough estimate of the frequency at which the system becomes unstable. These delays limit the speed of the system to ∼1 ms. Faster feedback would be possible with commercially available hardware updates, specifically AODs with faster response times and a DSP board with a faster processor. (For display in this thesis, the experimental data were low-pass filtered based on the measured oscillation frequency, unless otherwise stated.)

The discussion so far considers a cartesian linear system (extension to a 2-D linear system is straight forward). However, for the purpose of controlling a bead attached to a rotary molecular motor it is more convenient to express the position of the bead in polar coordinates (r_b, θ_b). To control only the angle coordinate, θ_b, the radius of the trap was chosen to remain constant irrespective of r_b. This is desired as a bead attached to a rotary molecular motor rarely moves along a perfect circle, and forcing it to move along such a path with feedback, would not be beneficial.

The 2π periodicity of θ_b requires a non-linear feedback algorithm:

$$\theta_{t,n} = \begin{cases} \theta^*_{t,n} & \text{if} \quad |\theta^*_{t,n} - \theta_b| < \theta_{max} \\ (\theta_{b,n} - \theta_{max}) & \text{if} \quad (\theta^*_{t,n} - \theta_b) < -\theta_{max} \\ (\theta_{b,n} + \theta_{max}) & \text{if} \quad (\theta^*_{t,n} - \theta_b) > \theta_{max} \end{cases} \tag{3.5}$$

where

$$\theta^*_{t,n} = \theta_{s,n} - K_p(\theta_{b,n} - \theta_{s,n}) - K_i \sum_{j=0}^{n} (\theta_{b,j} - \theta_{s,n}) \tag{3.6}$$

and $\theta_{t,n}$, $\theta_{b,n}$ and $\theta_{s,n}$ are trap angle, bead angle and set angle respectively. θ_{max} is a constant. The classic PI-algorithm of Equation 3.4 is modified so that the angle between the trap and the bead (proportional to torque) never exceeds θ_{max} (typically 90° in most of the presented experiments). This ensures that the torque on the bead will be in the correct direction even for large error signals and gain. Also, the addition of the term $\theta_{s,n}$ in the expression for $\theta_{t,n}$ removes the steady state error in the classic algorithm even with $K_i = 0$.

3.3 Single bead algorithms and experiments

3.3.1 Alignment and calibration of the detector and AODs

The back-focal-plane (bfp) laser detection used to monitor the position of a bead is non-linear and was calibrated for each bead that was studied or for a bead in each sample preparation [209, 17]. The dimensionless position signal from the QD, $N = (X, Y)$, is defined by $X = (\alpha + \beta - \gamma - \delta)/(\alpha + \beta + \gamma + \delta), Y = (\alpha - \beta - \gamma + \delta)/(\alpha + \beta + \gamma + \delta)$, where α, β, γ and δ are proportional to the photo-currents of the four quadrants. N is a non-linear function of the 3-dimensional position of the bead, $n = (x, y, z)$ (Figure 3.1), and therefore requires calibration. Before each experiment, the QD and AODs were aligned in the following way.

1. A bead stuck to the coverslip surface was moved through the detector laser focus with the piezo stage and the centre of the detector beam was defined as the mid-point of the single-valued range of the X and Y signals (see Figure 3.1 B). *2.* With the bead at this centre, X and Y were set to zero by adjustment of a mirror that steers the detector laser beam onto the QD. *3.* Steps 1 and 2 were repeated several times to remove any sensitivity to the initial state of alignment. *4.* With the AODs set at the centre driving frequency and the stuck bead replaced by a bead trapped a few microns from the coverslip, X and Y were again set to zero by adjustment of mirror M1 (Figure 2.1 and 2.6). By scanning beads, either in 2 dimensions with the AODs or in 3 dimensions with the piezo-electric stage, data-sets $N_i(n_i)$ were obtained, (the measured QD signal at selected bead positions n_i). For example, Figure 3.1 A shows an intensity plot of X versus (x, y) for a 500 nm bead scanned using the AODs, with iris open and objective overfilled. A least-squares 5^{th} order polynomial fit was used to describe the detector response in the region where (X, Y)

are single valued for each bead studied:

$$
\begin{aligned}
x &= \sum_{n=1...5} \left(a_n X^n + b_n Y^n \right), \\
y &= \sum_{n=1...5} \left(c_n X^n + d_n Y^n \right). \qquad (3.7)
\end{aligned}
$$

Figure 3.1 B shows X as a function of x at $y = 0$ for a 500 nm bead scanned with the piezo-electric stage, showing the effect of different settings of the detector beam iris. The detector response is monotonic over 400 nm with the iris open and the objective overfilled (*squares*), increasing to 1200 nm when the iris reduces the beam to 0.4 mm (*triangles*, the diameter of the objective back aperture is 7 mm). The primary calibration standard was the stage operated in closed-loop mode with capacitive sensing, giving an absolute position uncertainty of 1 nm as quoted by the manufacturer. To calibrate the AODs, an individual bead was scanned in (x, y) first using the AODs and then, after sticking it to the coverslip, using the stage. This confirmed the linear dependence of trap position on AODs driver frequency, and determined a conversion factor of 600 nm/MHz, consistent with the value estimated from the trap beam optics and the manufacturer's specifications for the AODs. The smallest movement of the trapping laser is 9 nm, limited by the frequency resolution of the AOD driver. For typical rotational trajectories of 100-1000 nm beads attached to motors this corresponds to an angular resolution of 1-10°, depending on the radius of the circle at which the trapping laser was kept. Figure 3.1 C, shows Y as a function of x at a range of equally-spaced values of y, for a 500 nm bead scanned in (x, y) by the stage, illustrating the cross-talk between orthogonal axes. An ideal detector, linear and without crosstalk, would give a series of equally spaced horizontal lines in such a plot. By contrast, the sensitivity of the QD signal Y to movement in y decreases at larger absolute values of x, as the bead moves out of the detector laser focus. This illustrates the need for the 2-dimensional fit of Equation 3.7. The

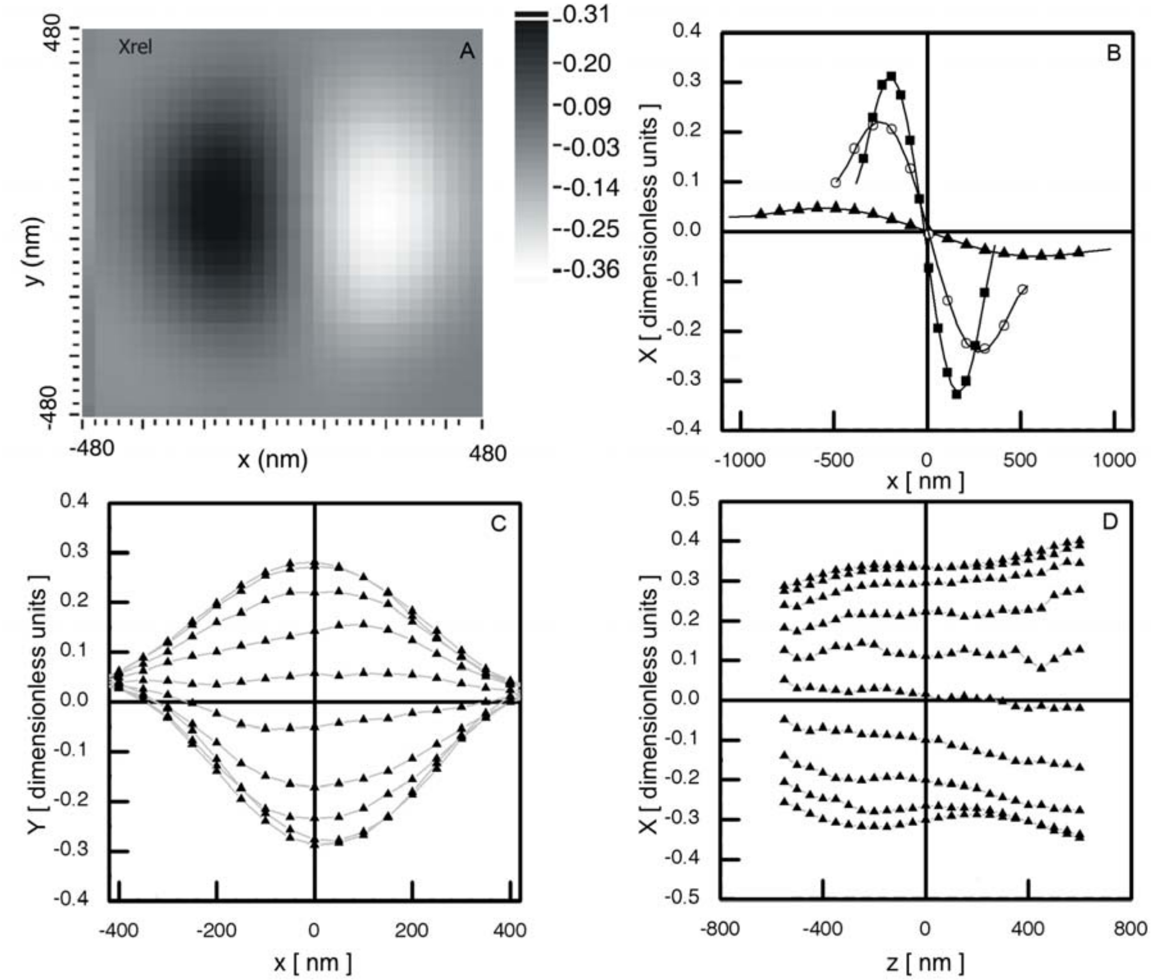

Figure 3.1: Calibration of QD signal (X, Y) from single beads, using AODs and piezo-electric stage. (A) Intensity plot of X versus bead position (x, y) for a 500 nm bead scanned using the AODs on a 30 nm square grid. (B) X as a function of x at $y = 0$, for a 500 nm bead scanned with the piezo-electric stage. The monotonic range of detector response increased from 300 nm to 600 nm and 1200 nm (squares, circles, triangles) as the iris opening decreased from 7 mm to 2.5 mm and 0.4 mm respectively. Lines represent a 5^{th} order polynomial fit . (C) Y as a function of x for 10 different equally spaced y values, showing cross talk between x and Y. (D) X as a function of z for 10 equally spaced x values, showing cross talk between z and X. In (C) and (D) a 500 nm bead was scanned by the piezo-electric stage, with 50 nm separation between y and x values respectively. Data were sampled at 2 kHz and X, Y values for each position were averaged over 0.2 s. The iris opening was 7 mm, equal to the diameter of the objective back aperture, except where otherwise stated.

crosstalk between X and z is illustrated in Figure 3.1 D, which shows X as a function of z at a range of equally-spaced values of x, also for a 500 nm bead scanned in (x, z) by the stage.

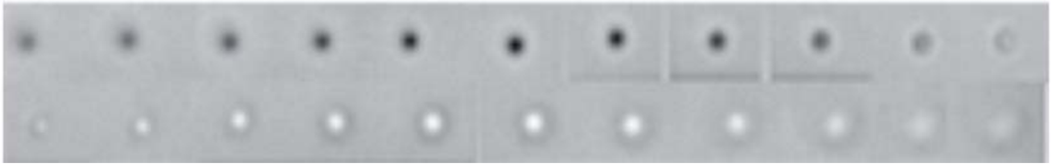

Figure 3.2: Bright-field images of a single bead scanned in 100 nm steps in z. The accuracy with which $z = 0$ could be set by eye using video images was found to be ∼30 nm.

At the beginning of each experiment $z = 0$ was defined such that the average brightness of the bright-field image of the bead was similar to the background: thus beads appeared gray at $z = 0$, black at $z > 0$ (by definition, when the microscope and laser focus was in the sample buffer) and white at $z < 0$ (focus in the coverglass, Figure 3.2). By setting $z = 0$ by eye 20 times each for 9 different beads and recording the spread of actual heights read from the calibrated piezo-electric stage, this procedure sets $z = 0$ with an estimated accuracy of ∼30 nm, comfortably within the range of ∼400 nm over which the variation of X with z is negligible (Figure 3.1 D). The same was true for crosstalk between Y and z (data not shown). Therefore any possible effects of z drift on the detector response $N(x, y)$ were neglected. The experimental procedure was as follows.

(1) Set $z = 0$ and then align QD and AODs as described above. *(2)* Trap a bead, scan it in (x, y) with the AODs, and use this scan to determine the calibration parameters a_n, b_n, c_n, d_n (Equation 3.7) for that bead. *(3)* Pass these parameters to the feedback algorithm running on the DSP board, to determine the trap position (u_n, corresponding to the control term U_n in Equation **??**) from the QD signal in subsequent experiments on that bead. In cases where it was not possible to scan a bead, for example when the bead of interest was attached to the motor before being examined, calibration parameters were obtained for another bead of the same size in the same sample preparation.

3.3.2 Trap stiffness

Calibration of trap stiffness is necessary if the absolute value of force or torque exerted upon a molecular motor via the bead are to be known. For small displacements of a trapped bead the force is given by $F = -kx$, where k is the trap stiffness and x is the bead displacement. This allows the trap to be calibrated using Brownian motion of the bead, in two different ways [17, 209]. The simplest method is based on the principle of Equipartition of Energy [209], which states:

$$\frac{1}{2}k\langle x^2\rangle = \frac{1}{2}k_BT \tag{3.8}$$

where k_B is Boltzmann's constant and T the absolute temperature. This gives k directly from the mean-squared displacement, dependent upon calibration of the QD signal as described above. An alternative method based on the power-spectrum of Brownian motion does not require knowledge of the absolute displacement of the bead [264]. To a first approximation the power-spectrum is Lorentzian, with a corner frequency $f_c = \frac{k}{2\pi\zeta}$, where ζ is the viscous drag coefficient of the bead. In practice the power-spectrum was fitted using a more accurate theory that accounts for discrete sampling of the data, low-pass filtering by the QD and inertial effects from the entrained fluid surrounding the bead [264], using a program made freely available by the authors [265]. The program gives a corrected value of f_c, from which the trap stiffness k was calculated, using Faxen's formula with correction for the proximity of the surface to calculate ζ [209]:

$$\zeta = \frac{6\pi\eta r}{1 - \frac{9}{16}(\frac{r}{h}) + \frac{1}{8}(\frac{r}{h})^3 - \frac{45}{256}(\frac{r}{h})^4 - \frac{1}{16}(\frac{r}{h})^5} \tag{3.9}$$

where η is the viscosity of the fluid, h distance of the bead from the surface of the coverslip and r the radius of the bead. At least 30 separate recordings were used at various laser powers to calibrate each bead, each lasting 2 s, with a sampling frequency of 36 kHz and anti-alias pre-filtering at 16 kHz. A 500 nm bead was trapped with a stiffness of (1.11 ± 0.02) pNμm^{-1} per mW of trapping laser power in the x direction, and (1.03 ± 0.02) pNμm^{-1}mW^{-1} in the y direction, as measured by the power-spectrum method (Figure 3.3 A). The equipartition method gave slightly lower values of stiffness, typically within 4% of the values obtained from the power-spectrum. This is most likely due to external noise at low frequencies, which is ignored in the power-spectrum method by exclusion of low frequencies from the fitting of f_c, but adds to the variance in the equipartition method, lowering the estimate of trap stiffness. The asymmetry between x and y stiffness is in agreement with theoretical predictions for polarized laser light, and is expected to vanish as the diameter of the bead approaches the trapping laser wavelength [266].

One unavoidable property of AODs is that the intensity of the deflected beam varies with the angle of deflection, and thus the trap stiffness varies with position. This effect was limited to a $< 8\%$ intensity variation over the full range of the AODs by choosing the appropriate driving amplitude for the range of frequencies used. The remaining variation was characterized by measuring trap stiffness at different positions, and was found to follow the intensity variation as expected (Figure 3.3 B).

3.3.3 2-Dimensional Feedback Control

Several tests were carried out to demonstrate the experimental performance of the feedback system anticipated by theory. Figure 3.4 A shows the trap acting as a position clamp, holding a 500 nm bead fixed, while measuring an external force applied by viscous drag. The piezo stage was moved in a triangular wave along the x-axis (Figure 3.4 A, bottom) with a velocity of ±420 ms^{-1}, corresponding to a Stokes drag force of ±2.1 pN. Figure 3.4 A, top shows the displacements of the trap and bead with no feedback. The bead displacement due to the external force

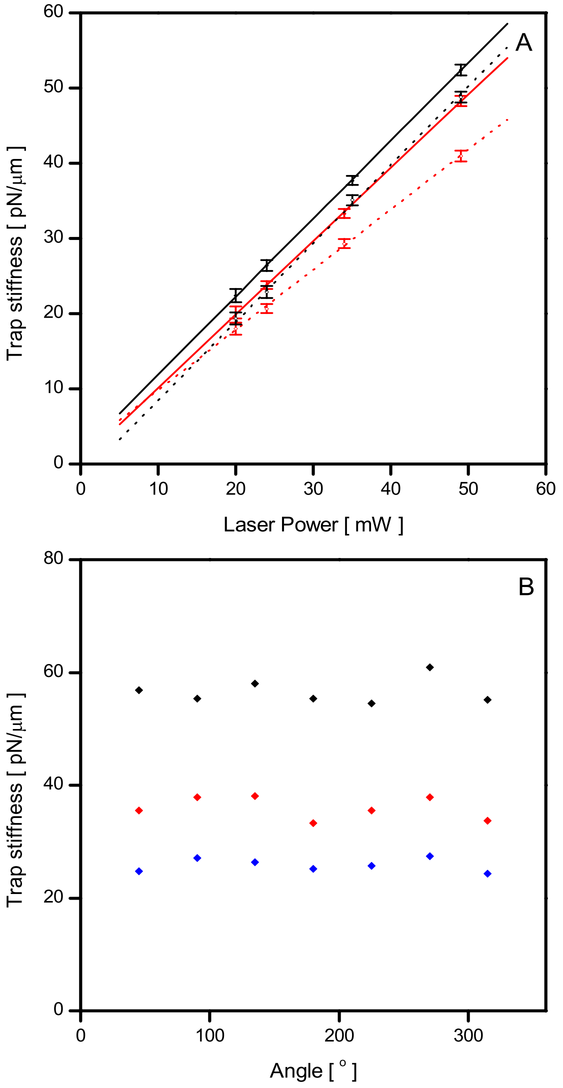

Figure 3.3: Trap stiffness (A) Trap stiffness versus laser power is shown. k_x (red, full line) and k_y (red, dotted line) calculated with the equipartition method have slightly lower value than k_x (black, full line) and k_y (black, dotted line) obtained from power spectrum analysis. The k_x value in both cases has a slightly higher value than k_y consistent with theoretical predictions [266]. (B) Trap stiffness versus angle is shown for 3 different laser powers: 24.5 mW (blue), 33 mW (red) and 55.5 mW (black). Variations with angle are 15.3%, 15% and 10.4 % consistent with measured variations in the laser power intensity over the range of AODs' frequencies used to generate these angles.

is ±100 nm, as expected given the drag force and the trap stiffness of 20 pNμm^{-1}. Figure 3.4 A, middle shows the corresponding displacements with the following

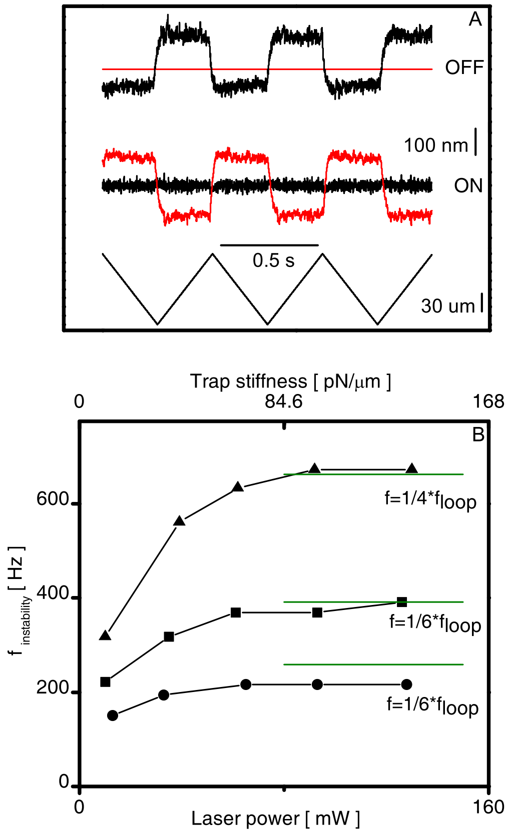

Figure 3.4: 2-D X and Y feedback. (A) Top: The response of the 500 nm bead without feedback (black) to a drag force of ± 2.1 pN, and the position of the trapping laser (red). Middle: The position of the bead (black) and the trapping laser (red) when the feedback in X and Y is turned on. Feedback parameters were set to K_p= 0.3, K_i= 0.06 and trapping laser power to 18 mW (20 pNμm^{-1} trap stiffness). The experimental data shown was passed through a low-pass second order Chebyshev filter (available in National Instruments LabView software) before display, with pass frequency set to 200 Hz. Bottom - Movements of the piezo-electric stage. (B) Critical frequency above which the system becomes unstable. Data were sampled at 10 kHz, 5 kHz and 2 kHz respectively (triangles, squares, circles). Feedback parameters K_p and K_i were increased until the bead held in the trapping laser visibly oscillated for a given laser power (trap stiffness) and sampling rate. The oscillation frequency was obtained from the power spectrum of the QD signal. Further increasing K_p and K_i does not change this frequency. The critical frequency depends on the laser power up to a point, above which the delays in the system, and not the trap stiffness, limit the feedback time resolution.

feedback algorithm

$$U_n = K_p(R_n - X_n) + K_i \sum_{j=0}^{n}(R_j - X_j) + K_d((R_n - X_n) - (R_{n-1} - X_{n-1})) \quad (3.10)$$

applied separately in the X- and Y-axis. Equation 3.10 is very similar to Equation 3.4, but the feedback is now performed on QD signal (X_n, Y_n), not the bead position. U_n and R_n are QD signals corresponding to u_n and r_n given in Equation 3.4. The polynomial fit of Equation 3.7 is used to determine the trap position u_n corresponding to the desired QD signal U_n; in most cases feedback is performed in the linear range of QD (Figure 3.1) and these are proportional. The bead displacement due to the external force is reduced to ±0.06 nm, indicating that the effective trap stiffness at low frequency is increased to 35 nNμm^{-1}. To further test the feedback performance and compare it to the theoretical predictions, the frequency at which the system under feedback becomes unstable was measured. Figure 3.4 B shows the critical frequency above which the system becomes unstable as a function of laser power (trap stiffness) for different sampling rates. The critical frequency depends upon laser power up to a point, above which trap stiffness is no longer limiting and instead feedback is limited by the delays in the system (as previously discussed). Horizontal lines in Figure 3.4 B correspond to the $\frac{1}{4}$ and $\frac{1}{6}$ of overall feedback execution frequency, f_{loop}, indicating a rough agreement with the simplified theoretical prediction that the critical frequency should be approximately $\frac{f_{loop}}{4}$. The algorithm in Equation 3.10 can run up to f_{loop} ~2.6 kHz, thus the minimum response time of our system with this algorithm is ~2 ms.

Figure 3.5 shows two methods of feedback control of the angle of a bead moving on a circular trajectory. In the first method, the QD set-point was moved step-wise to different points on the circle and applied feedback separately in the X- and Y-axis, as in the experiments of Figure 3.4. The trajectories of trap and bead are shown in Figure 3.5 A. In the second method, the trapping laser was moved on a circle of fixed radius 300 nm (Figure 3.5 B, right). The angle at which the trap was placed, θ_t, was determined using the feedback algorithm of Equation 3.5, with the bead angle, θ_b, determined directly from QD signals by a simple rectangular-to-polar conversion. The resulting trajectory of the bead is shown in Figure 3.5 B, left. During the time in which the bead was kept at the same angle θ_t and θ_b are expected to be equal, any differences observed are due to imperfect alignment of the AODs and QD. The algorithm in Equation 3.5 can run up to f_{loop} ~5 kHz in this system, thus the minimum response time of the system with this algorithm is ~1 ms.

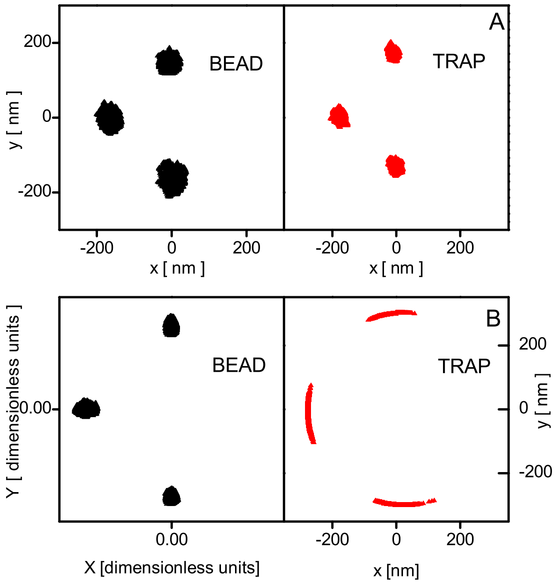

Figure 3.5: Control of a single bead with feedback (A) using the control law of Equation 3.10 applied to X and Y independently, (B) using the control law of Equation 3.5, in which the radius of the bead is not controlled and the trap is held at a fixed radius of 300 nm. Left - position of the bead, right - position of the trap. Feedback parameters were set to $K_p = 0.04$, $K_i = 0.002$ and $K_p = 0.8$, $K_i = 0.2$ in (A) and (B) respectively. Laser power was 18 mW. Experimental data was passed through a low-pass second order Chebyshev filter (available in National Instruments LabView software), with pass frequency (f_{pass}) set to 200.

This demonstrates that the system can control the position of a single bead in 2-dimensions using programmable feedback algorithms, and in particular that the angle of a bead moving on a circular trajectory can be controlled. If the bead is rigidly attached to the rotor of a molecular motor, for example to the γ-subunit of

F_1, then the only degree of freedom is the bead-rotor link angle and thus controlling the position of the centre of the bead controls the motor angle as desired.

3.4 Bead pair feedback algorithms and experiments

A bead-pair is necessary to control the rotation angle of the bfm with an optical trap (discussed further in Chapter 4.). It also has advantages for use with F_1. The asymmetry of a pair allows rotation to be observed directly, rather than relying on displacement of the centre of a single bead due to eccentricity of rotation. Also, the bead-pair acts as a lever-arm, allowing more torque to be applied to the motor. However, the use of a bead-pair as the handle of choice results in several specific problems which I address below.

3.4.1 Alignment

When replacing a single bead with a bead pair, the calibration of the QD for a single bead no longer applies. Instead one notes that for experiments with rotary motors only the angle of the projection of the long axis of the bead-pair onto the plane perpendicular to the motor's rotation axis is of interest. If the motor's axis is aligned with the microscope axis, this is the same as the angle of an image of the bead-pair, θ_{bp} (Figure 3.6). To estimate θ_{bp} from the QD signal (X, Y), a rectangular-to-polar conversion $(X, Y) \rightarrow (R_{bp}, \Theta_{bp})$ was performed and assumed that $\Theta_{bp} = \theta_{bp}$. This estimate of θ_{bp} can then be used to perform 1-D angular feedback using the algorithm of Equation 3.3, as described for single beads in section 3.2. and illustrated in Figure 3.4 and 3.5. To ensure that this estimate of θ is reasonable it was necessary to close the detector laser iris, extending the monotonic range of the QD to cover the size of a bead-pair. Feedback control of the angle of pairs of biotinylated beads each 500 nm in diameter, attached to a microscope coverslip via streptavidin and BSA (Methods 2.3.) was demonstrated. Pairs which showed free rotational Brownian motion (RBM), indicating a single point of attachment on one

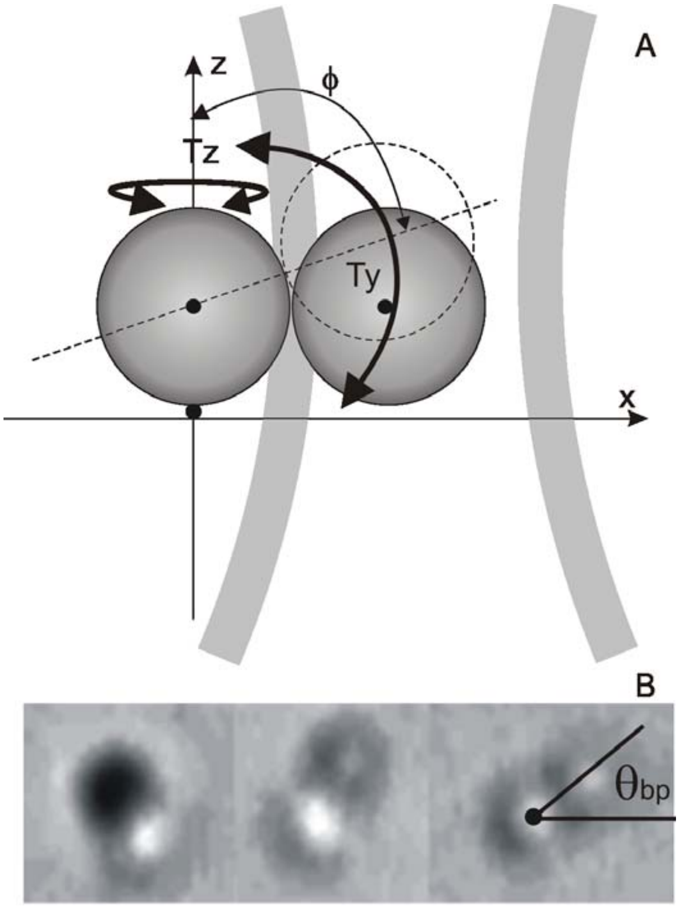

Figure 3.6: (A) Schematic diagram of a bead-pair attached to a surface by a motor at $x = y = z = 0$ and held by the optical trap. (B) Bright-field video microscope images of bead-pairs with different values of the angle as defined in (A). The pairs with ϕ ~90° like the one in the right panel were chosen, for which the angle θ_{bp} is defined.

of the beads were chosen. Conversion of QD signals and optical trap positions into angles is very sensitive to alignment of the centres of the QD and AOD range, as in the case of angular feedback experiments on single beads. This alignment was performed using single beads at the beginning of each experiment, as previously described. With bead-pairs attached to the surface, a further alignment of the point of attachment with the QD and AODs centres is also required. Two indicators were used to performed this alignment. Initial, **coarse alignment** was achieved by moving the stage so that the QD signal due to RBM (with no optical trap) became approximately circular. Subsequent, **fine alignment** was achieved by rotating the optical trap slowly in a circle centred on the AOD origin (previously aligned to the QD origin) and moving the stage to minimize variations in $\theta_{bp} - \theta_t$, which was taken to indicate that the point of attachment was at the centre of the AOD circle. The fine alignment procedure usually optimized the circularity of the QD signal, confirming that the attachment point, QD and AODs centres were all aligned. For pairs of 500 nm beads, the fine alignment procedure could be successfully applied if the radius of the circle described by the trap was between 300 and 600 nm. In most cases the best circularity was achieved with trap radius of 400-500 nm. In angular feedback experiments, the radius of the circle at which the trapping laser was kept was fixed at the value that gave the best circularity during the fine alignment.

3.4.2 Feedback control of Bead Pairs

Figure 3.7 shows the results of applying the angular feedback algorithm of Equation 3.3 to a bead pair that showed free RBM with a nearly circular QD signal: an indicator of good alignment and a single point of attachment to the surface. Figure 3.7 A shows the angles of the trap θ_t (*red*) and bead-pair θ_{bp} (*black*) versus time when the set-point angle θ_s was changed by 15°. The standard deviation of bead-pair angles at each set point was ∼2°. Figure 3.7 B (top-left) shows the power-spectra of θ_t (*red*) and θ_{bp} (*black*) when a bead pair is held at a fixed angle with the same feedback parameters and laser power as in Figure 3.7 A. Figure 3.7 B (top-right) shows the transient response to the change in set-point on an expanded time-scale; illustrating that the system response time is ∼2 ms. Figure 3.7 B (bottom) shows power-spectra and transient response with the same feedback parameters and increased laser power. In this case the rise time is reduced to ∼1 ms. In both cases the feedback is very stiff, approaching critical behaviour as indicated by the peak in the power-spectra and damped oscillations in the step response. The frequency at which the instability occurs is in agreement with expectations ($\sim \frac{1}{4} f_{loop}$). The differences between θ_t and θ_{bp} when the set-point is not changing are evidence of imperfect alignment between the trapping laser and the bead pair, which was found to be very difficult to eliminate.

3.4.3 Angular Trap Stiffness

Figure 3.8 A shows θ_t (*red*) and θ_{bp} (*black*) vs time as the trap is moved in a circle in 10° steps without feedback. Bead-pairs were attached to F_1 molecules (Methods 2.5.), but pairs that exhibited free RBM when not trapped were selected. (Such non-rotating pairs were very common in F1 rotation assays, they probably represent either damaged F1 molecules or freely rotating F1 molecules where only one of the 3 his-tags is attached to the surface.) 'Flat' bead-pairs, those with angles close to ϕ ~90° (Figure 3.6 A; Figure 3.6 B, right) were selected, for reasons discussed in Chapter 6. Angles are averages over 40 successive rotations lasting a total of 15 s. The relaxation time of the system was calculated, $\frac{\zeta_\theta}{k_\theta}$ (where k_θ is the torsional stiffness of the trap and ζ_θ is the rotational viscous drag coefficient of the bead-pair) from an exponential fit of the response to each step (inset, lower) at each angle. Analysis of the free RBM between steps provides an estimate of k_θ (the equipartition method was used, $\frac{1}{2}k_\theta\langle\Delta\theta_{bp}^2\rangle = \frac{1}{2}k_B T$). The rotational viscous drag coefficient of the bead pair attached to the surface is not known, therefore the power spectrum method cannot be used. Figure 3.8 B shows $\frac{k_\theta}{\zeta_\theta}$ vs θ_{bp} for 3 bead pairs on HRP surface, obtained from the step response (Figure 3.8 A, inset). Figure 3.8 C shows k_θ vs θ_{bp}, obtained using the equipartition method, for the same bead pair as in Figure 3.8 B (*black*), and two other bead pairs on a silane surface. Figure 3.8 D shows k_θ versus laser power, for several bead pairs held at 45°. Trap stiffness is linear with laser power for all bead pairs, but the slope ($\frac{dk_\theta}{dP}$, where P is laser power) varies from pair to pair. The different shapes of the curves for $\frac{k_\theta}{\zeta_\theta}$ and k_θ most probably reflect angular dependence of ζ_{bp}, which is often observed for the flagellar motor as

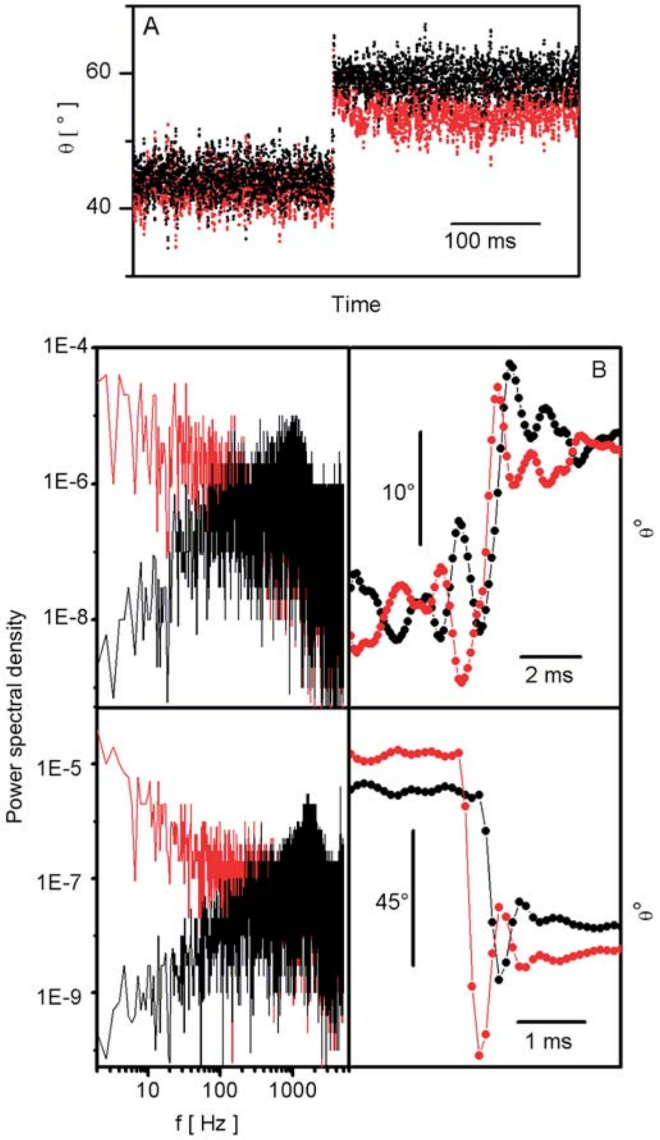

Figure 3.7: Control of bead-pair angle. (A) The angular feedback algorithm of Equation 3.3 was applied to bead-pairs that showed free RBM. Angles of the trap, θ_t, and bead-pair, θ_{bp}, are shown in red and black, respectively. The set-point angle θ_s was switched from 45° to 60°. Trapping laser power was 18 mW and radius 0.3 μm (resulting in a minimum angular movement of the trapping laser of $\sim 2°$). Feedback parameters are $K_p = 0.8$ and $K_i = 0.2$. The mean bead-pair angles and standard deviations are $(44.5 \pm 2.4)°$, $(59.3 \pm 2.2)°$ for $\theta_s = 45°$, 60°. Bead-pair angle and trap angle were passed through a low-pass second order Chebyshev filter before display, with f_{pass}= 450 Hz. (B) Top left: Power-spectra of θ_t (red) and θ_{bp} (black) for a bead-pair held at a fixed angle with the same feedback parameters and laser power as in (A), and bottom left: with laser power increased to 85 mW. Top right: θ_t (red) and θ_{bp} (black) versus time showing the response to a change of a set-point, for 18 mW laser power. System response time is $\sim$2 ms. Bottom right: with 85 mW laser power the system response time is reduced to $\sim$1 ms.

a variation in the speed of an un-trapped motor with angle [267]. Possible sources of angular variation and variation between bead-pairs are discussed in Chapter 6. Many questions can be answered by comparing relative motor torque under different conditions. However, if an accurate measurement of absolute torque is required it will be necessary to calibrate the angular trap stiffness for each bead pair after inactivating the motor at the end of each experiment [260]. A calibration procedure was developed and presented here, which can be completed in a few second and implemented as part of experimental protocol.

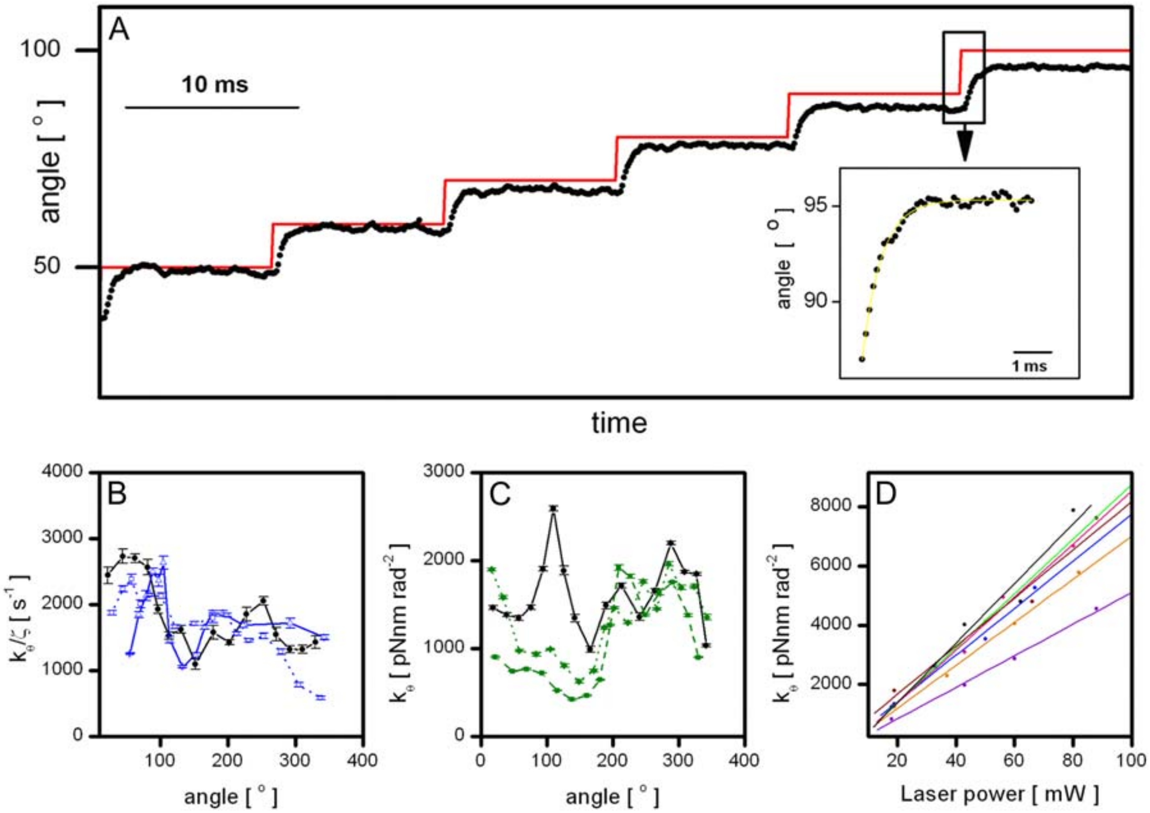

Figure 3.8: Calibration of the angular trap stiffness for 500 nm non-rotating bead-pairs attached to F1 molecules. (A) Bead pair angle, θ_{bp} (black), and trap angle, θ_t (red), vs time for a bead-pair in a trap moving in 10° steps without feedback. Angles are averages over 40 successive rotations. (inset) Step-response, with exponential fit. (B) The ratio of angular trap stiffness to rotational viscous drag coefficient, derived from the time constants in the fits in (A) as described in the text, vs angle, for 3 bead-pairs on HRP (black) and silane surface (blue) (Chapter 2.5.). (C) Angular trap stiffness vs angle for the bead-pair in black in (B) (black) and two additional bead-pairs (green) on a silane surface. (D) Trap stiffness at 45° vs laser power for several bead-pairs on a BSA surface (Chapter 2.5.). Data were sampled at 10 kHz, laser power in (A-D) was 30 mW and the trap was kept on a circle of radius 420 nm. Bead-pairs with $\phi\sim 90°$ which performed free rotational Brownian motion without the trap were chosen for all calibration experiments. Error bars in B and C are standard errors obtained by averaging values obtained from two adjacent angles.

CHAPTER 4

BACTERIAL FLAGELLAR MOTOR

4.1 Overview

In this chapter the ‘angle clamp’ system is applied to the bacterial flagellar motor (being able to stall the bfm with feedback is potentially useful for observation of stepping behaviour of the motor).

I have also found that with my system, a 500 nm bead-pair on the bfm can be rotated at speeds of up to ∼600 Hz, promising to be useful for investigations of the motor torque-speed curve*. Below I give the preliminary results of this method.

There is one more optical trapping system available in our group. This uses a 1064 nm laser wavelength for bfp detection*. Since my system uses a 632 nm laser wavelength for bfp detection it ‘sees’ better, allowing us to detect rotation of smaller beads attached to the bfm (500 nm, 300 nm, 200 nm in diameter). I give a brief example of the data obtained by other members of Dr. R.M. Berry’s group with a short explanation of the information learned from it.

CONTRIBUTIONS AND COLLABORATIONS: The system presented in this thesis was initially designed for experiments on the F_1 motor. However the experimental protocols for F_1 purification and rotation assay preparation needed to be investigated and established. Apart from a few preliminary experiments on F_1 (obtained and purified by Prof. M. Futai’s group) done by Dr. R.M. Berry, no previous research has been done on F_1 in this lab. Therefore I decided to test the performance of the system on a biological motor familiar to our group, prior to spending a substantial amount of time and work on starting the research on F_1. This reasoning was also influenced by the fact that at the stage in my research when the feedback system was ready to go (∼2 years after I started) I was eager for some biology and was interested in learning more about the bfm, having been the only person in the group not working on it.

---

[*] as an alternative to electrorotation. Tania Saxl, in this lab, has put and still is putting a substantial effort into electrorotation experiments

[*] This system is used for electrorotation experiments as well, together with a few other ongoing projects like, for example, using a polarized laser light to apply torque to a birefringent particle.

This has led to the initial feedback experiments done on the bfm as well as to the research into the switching mechanism of the bfm, which was started together with Fan Bai. The initial data was obtained by Fan Bai and I. Fan Bai subsequently continued this work and obtained additional data, and Dan Nicolau (D. Phil. student in the Department of Mathematics, University of Oxford) contributed to the theoretical modelling. Recently Richard Branch (DTC student working on an 8 week project prior to commencement of his D. Phil in our group) contributed to the experiments and theoretical modelling by looking at the interval time distributions of CW and CCW interval times.

Apart from Fan Bai and Richard Branch, Chien-Jung Lo and Dr. Yoshiyuki Sowa, in this lab, use the system and QuView programs I wrote for detection of small beads attached to a sodium driven *E. coli* flagellar motor. My contribution to their work is restricted to building the system and showing them how to use it.

4.2 Feedback on the bacterial flagellar motor

Preliminary experiments in which the stall torque of the bacterial flagellar motor was monitored demonstrate the use of the feedback system on a rotary molecular motor. Figure 4.1 demonstrates that a bead-pair is necessary to control the flagellar motor with an optical trap. Figure 4.1 A shows the x- and y- position and power spectrum obtained from a 500 nm bead attached to a flagellar filament, with no optical trap. The speed of the bead obtained from the power spectrum [173] is ∼60 Hz (inset). Figure 4.1 B shows the same signals with the bead held stationary at a point on the original orbit by independent x- and y-axis feedback using the algorithm of Equation 3.10, as illustrated in Figure 3.4. The motion of the bead was severely constrained compared to the original circular orbit, but the peak in the power spectrum indicates that the motor and bead are still rotating. This is possible because the hook can flex in such a way as to allow the filament stub to describe a cone, tangent to the bead with its apex at the motor, as illustrated in

Figure 4.1 E. Because the hook is a universal joint, this allows the motor to rotate about its (vertical) axis while the bead rotates about an axis joining the motor to the bead centre. Because the latter axis passes through the centre of the bead, the bead can rotate even if its centre is prevented from moving by the optical trap. In contrast, Figure 4.1 C shows the QD signal from a rotating bead-pair and Figure 4.1 D illustrates that there was no rotation of the motor when the pair was held stationary with the optical trap at a fixed point. Unlike with a single bead, there is no possible rotation axis passing through the motor and the bead-pair which is also a symmetry axis of the pair, and thus any rotation of the motor will be coupled to detectable rotation of the pair. In particular, rotation about the axis joining the motor and the centre of the trapped, outer bead is blocked by interaction between the inner bead and the cell surface as indicated by the black bars in Figure 4.1 F.

Figure 4.2 shows measurements of the torque of a bacterial flagellar motor when stalled. A bead-pair and the angular feedback algorithm of Equation 3.5 were used, and the same methods as described for Figure 3.7. The set angle was changed during periods of feedback lasting 3 s or 10 s, alternated with periods of same length when the motor was allowed to rotate freely, to provide an independent measure of the motor torque and to determine whether any damage had occurred. Figure 4.2 shows measurements of torque for one of 9 different set angles, 90°. The difference between the trapping laser angle (red) and bead angle (black) changes in time, hence the torque of the motor changes as well. Observed halving of the motor torque (Figure 4.2, middle) is likely caused by a change from two torque generator units to one, similar to speed changes seen previously in freely rotating motors [164, 173]. Speed of a freely rotating bead-pair was observed occasionally in between intervals where the bead-pair was held fixed. At the beginning of the experiment the speed of the freely rotating motor was $\sim$20 Hz, corresponding to 2 stator units, and at the end of the experiment bead-pair was not rotating.

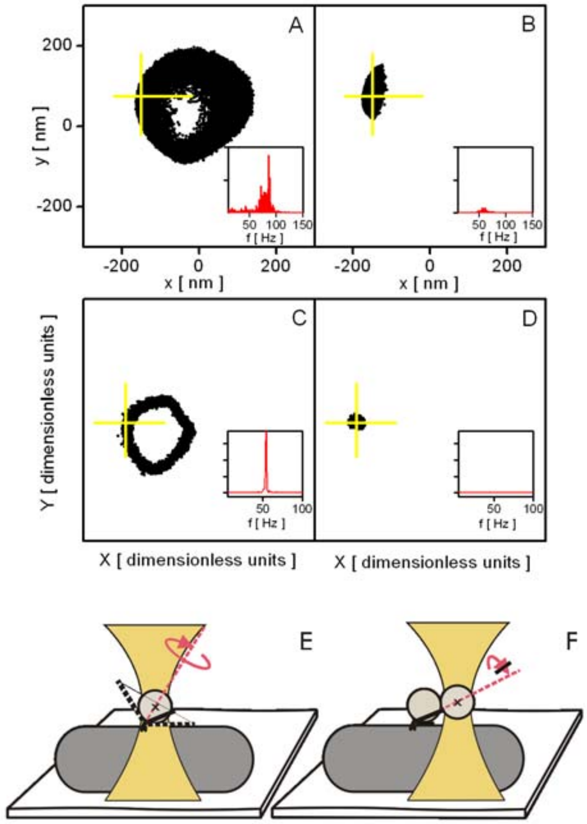

Figure 4.1: Stalling the bacterial flagellar motor with an optical trap. (A) (x, y) position of a single 500 nm bead attached to a freely rotating bacterial flagellar motor and (B) held by the trapping laser in conventional PI feedback at a point along the rotation trajectory of (A) indicated by the cross. Laser power was 25 mW and feedback parameters $K_p = 0.4$ and $K_i = 0.02$. (C) QD signal (X, Y) of a rotating 500 nm bead-pair attached to the bacterial flagellar motor and (D) held with the trapping laser at a fixed point indicated with a cross (along the trajectory of free bead-pair rotation in (C)). Laser power: 50 mW. Insets: power spectra of QD signal X, indicating the speed of bead rotation. Note that the motor is still spinning in B but not in D. (E) Schematic representation of a single bead experiment on the bacterial flagellar motor. A cell is fixed on a cover slip surface and a 500 nm bead attached to the bacterial flagellar motor via a filament stub. The centre of the bead is indicated with a cross and the bead rotation axis is indicated with a dashed line and curved arrow. The bead can rotate even when held fixed, due to the universal joint properties of the hook. This enables the motor to rotate as well. (F) Schematic representation of a bead-pair experiment on the bacterial flagellar motor. Black bars indicate that the rotation of the bead-pair around its axis, while the outer bead of the pair is held by the trap, is blocked by the interaction between the inner bead and the cell surface. This allows the motor to be stalled by holding the bead-pair fixed with the trapping laser.

This particular bead-pair was not calibrated, so an accurate estimate of the stall torque cannot be given. If a trap stiffness typical of the laser power, bead-pair size and radius of the circle at which the trapping laser was kept in Fig. 7 B is assumed, $k_\theta = 841 pNnmrad^{-2} \pm 100\%$, one can estimate the stall torque $T_{stall} = k_\theta \langle \theta_{bp} - \theta_t \rangle = 240 pNnm \pm 100\%$ which is consistent with the value of 150 pNnm estimated by other methods [171].

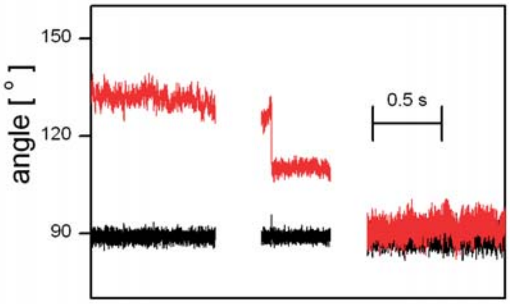

Figure 4.2: θ_{bp} (black) and θ_t (red) for a 500 nm bead-pair attached to the bfm with the feedback algorithm of Equation 3.10 used to hold θ_{bp}=90°. The difference between trap angle and bead-pair angle corresponds to the bacterial flagellar motor torque. Data is interpreted as showing a motor initially with 2 stator units losing first one and later both units, such that the torque goes from $2 \longrightarrow 1 \longrightarrow 0$ times the torque of a single unit. Feedback parameters $K_p = 0.8$ and $K_i = 0.1$, radius of the trapping laser = 420 nm, laser power = 29 mW.

4.2.1 Control of the speed of the bacterial flagellar motor

Figure 4.3 shows the QD signal and speeds of a bead pair attached to a bacterial flagellar motor, made to rotate at speeds up to 425 Hz by moving the trapping laser in a circle at a constant speed without feedback. As in the feedback experiment, the motors were allowed to rotate freely between periods of forced rotation to determine whether any damage had occurred. The experiment was stopped when rotation of the free motor was no longer observed.

Figures 4.2 and 4.3 indicate that damage is a significant obstacle for experiments were torque is applied to the bfm via an optical trap, and it needs to be reduced or avoided. Several ideas on how to reduce the encountered damage are discussed in Chapter 6. Both experiments, Figure 4.2 and 4.3, were performed at detection and trapping laser powers where no significant laser induced photodamage occurs, therefore most of the observed damage is expected to be mechanical [252].

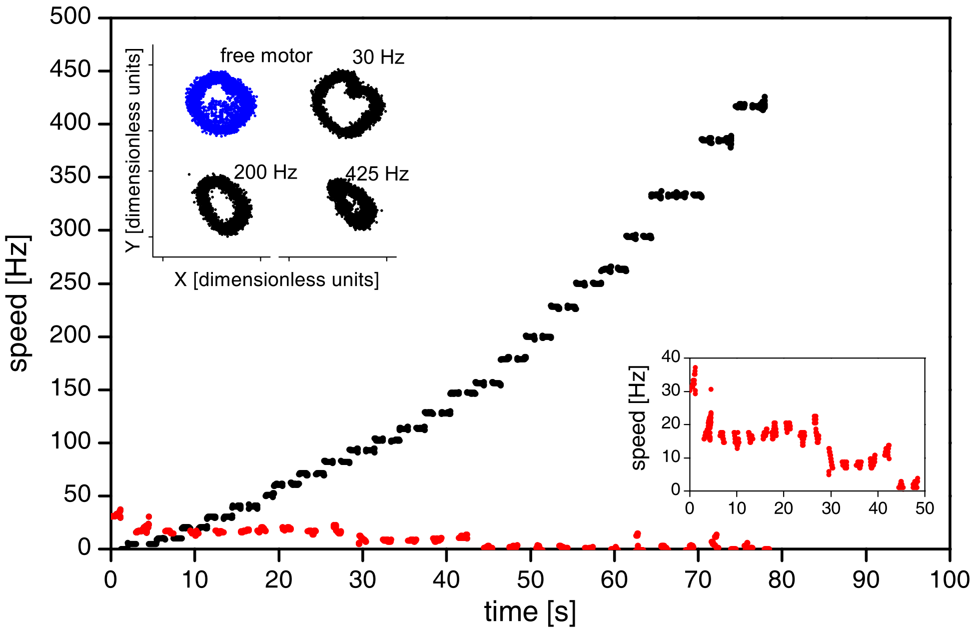

Figure 4.3: Control of the bfm rotation speed with an optical trap. Trapping laser was rotated at different speeds and applied to bfm motor via a bead-pair handle. Speeds of the externally rotated motor are shown in black. The trap radius was changed from 0.6 μm to 0.3 μm during the experiment and the laser power was 65 mW. The motor was rotated twice at each speed for 1 s, and allowed to rotate freely in between. Speeds of free rotating motor are shown in red. Inset right: close-up of free rotating motor speeds. The reduction in speed is stepwise suggesting a change in the number of stator units present in the order 3, 2, 1, 0. Inset left- The QD (X,Y) signal for the rotating bead-pair at different speeds.

4.3 Collaborations with other group members using the optical trap

4.3.1 Switching

The 1-D Ising model presented in Chapter 1.2 gives a possible mechanism of the bacterial flagellar motor switching. It can also explains pausing and slowdowns in motor rotation observed in previous experiments [187]. Initial data obtained in the system presented in this thesis with 500 nm, 350 nm and 200 nm beads on the wild type strain KAF84, who's motors switch direction, showed significant amount of pausing and slowdowns. In addition, (X, Y) traces of the bead rotation showed that the trajectory of the rotation stays the same in both directions not only during the rotation in a given direction after the switch, but also during the switch (as shown in Figure 4.4, Inset). This is an important feature for analysis of the motor switching (in particular for analysis of the time it takes for a motor to switch from rotating in one direction to the opposite direction) as it suggests that the time of the motor switch is not likely due to the universal joint properties of the hook. The switch time was defined as the time the motor stoppes having been rotating in CCW/CW direction, before it continues rotating in the CW/CCW direction. A stop is defined as an event where the motor speed is 0 Hz with the error margine given by the standard deviation in speed obtained from the records of continues CCW and CW rotation. The speed of the motor during the switch is calculated from (X, Y) trace by running window method. To further verify that the switch time is not instantaneous event, Fan Bai looked at the position of the longer and shorter switches on (X, Y) trajectory. This allowed him to compare them with the speed fluctuations within one rotation. He found that the longer switches happen on faster as well as slower parts of the (X, Y) trajectory confirming that they are not likely due to the universal joint properties of the hook or to the bead sticking to the cell and the surfaces at certain

parts of its circular trajectory. Since the initial data was encouraging for analysis of the motor switching F. Bai obtained additional data using 500 nm bead attached to the bfm via the hook and filament stub. He analysed ∼800 cells, giving ∼300 traces with no changes in the CW and CCW trajectories during the switch. He separated the cells according to the proportion of time spent in a CCW or CW direction*, and calculated the time it takes for a switch to happen from raw (X, Y) traces. This gave a distribution of switch times shown in Figure 4.4. Currently more data needs to be obtained to be able to look at the switch time distribution in all bias bins and compare the results with the predictions of the model. The distribution of switch times obtained in this experiment and its agreement with the model provides strong evidence that the underlying switch process occurs as explained in Chapter 1.2.
The interval time distribution of CW and CCW interval times for CCW to CW bias in the range of 0.8 to 0.9 is an exponential on short time scales (0-5 seconds). Again, more data needs to be obtained to look at switch interval distribution for other CW and CCW biases.

4.3.2 Low load measurements

Smf and torque-speed measurements at low load

As indicated in the Introduction, there are still many open question with regards to the function of the bfm in low load regime. This is the regime the motor normally operates in, when driving bacterial flagella, and is therefore of great interest. With the purpose of investigating the low load dependence of *smf* vs. speed and looking into the shape of torque-speed curve Chien Jung Lo performed experiments using my system for the detection of 350 nm and 200 nm beads attached to the bfm via the hook and filament stub.

---

*Thus the motors operating with similar [CheY-P] were looked at separately. Recent finding by [191] shows that combining experimental results obtained from cells with large differences in [CheY-P] masks the dynamical properties of the cooperative switching in a single motor.

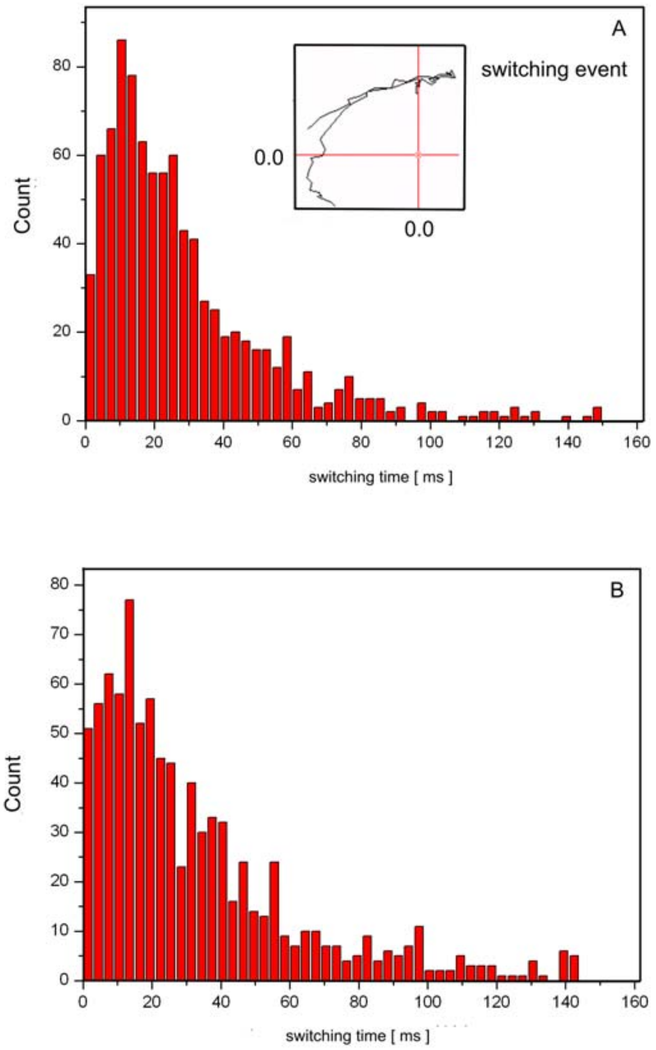

Figure 4.4: Distribution of observed times during which the switch occurs (switch time distribution) for (A) CCW to CW switches with the bias in the range of 0.8 to 0.9. Inset: An example of typical (X, Y) trace of the switching events that were analysed. Trajectory does not change in shape during the switch, and the bead rotates on the same trajectory in both directions (data not shown). (B) CW to CCW switches for the same bias as in (A). The Figure was obtained from Fan Bai.

An example of the signal obtained with a 200 nm bead is given in Figure 4.5 A. From the power spectral density shown in Figure 4.5 B the speed of the motor was ~600 Hz. C. J. Lo was able to obtain speeds of up to 800 Hz. However, the image of a 200 nm bead attached to the bfm in the bright field microscope is very small, and the speed of its rotation is very high thus lowering the yield of the assay and making it more difficult to obtain large enough data set of fast rotating 200 nm beads. In addition, when using beads of this size the drag coefficient of the sheared filament starts to significantly contribute to the overall drag coefficient (the size of the filament varies from cell to cell), affecting the accuracy of torque estimates. To increase the viscosity of the medium and thus overcome this problem C.H. Lo uses Ficoll [174, 268]. Once a fast rotating 200 nm bead is found, Ficoll of different concentrations is flowed through. The viscosity of the medium is appropriately increased, thus effectively increasing the load of a 200 nm bead. The procedure calibrates the shape of the torque-speed curve obtained with 200 nm beads.

Speeds of the motor, with a 200 nm and 350 nm beads attached, were obtained for different $\Delta\psi$ and pNa values and initial data suggest that the contributions of pNa and membrane potential in low load regime are not equivalent. If membrane potential is changed for each different external sodium concentration the slope of the speed and *smf* linear relationship will change. Further work will give additional new and interesting information.

Steps

Apart from investigating the relationship between the bfm power source and torque in the low load regime, independent control of $\Delta\psi$ and pNa will enable C.H. Lo to achieve stable motor rotation at low speed required for detection of motor stepping and precisely determine the number of stator units present. This is important in order to be able to determine whether the number of steps changes with the number of torque generating units. Analyses of motor fluctuations suggest that indeed the

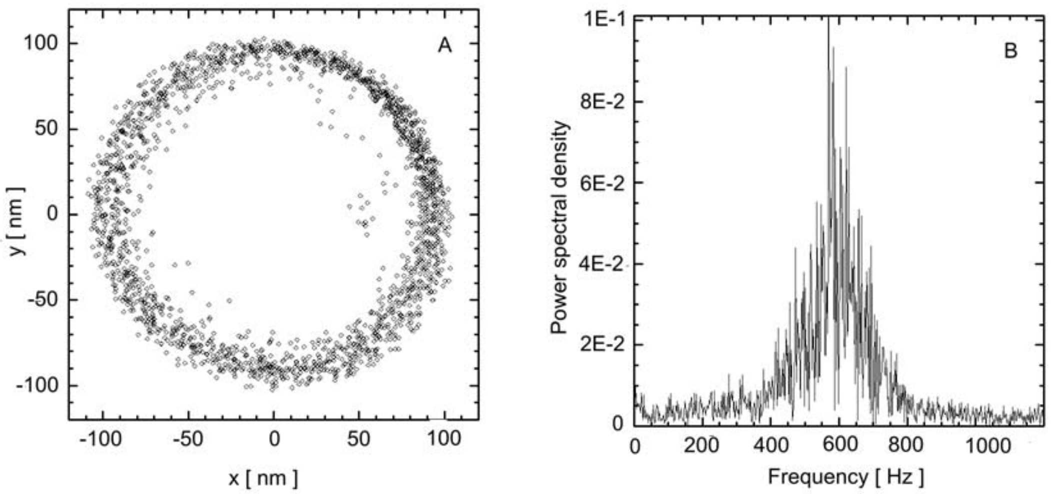

Figure 4.5: (A) An example of the trace obtained from 200 nm bead attached to the bfm via the hook and the filament stub. (B) Power spectral density ($z = X + iY$), indicating motor rotation is ∼600 Hz. The Figure was obtained from C. J. Lo.

number of steps increases with the number of torque generating units [180, 181]. This result is consistent with high duty ratio experiments, suggesting not only that the torque generating units are independent of each other but also that each remains connected to the rotor most of the time. However, these analyses were done based on the signal obtained from tethered cells, in the high load regime. The answer to the question of step number with two or more stator units present should tell us a lot in terms of the way the motor converts chemical energy into rotation. High temporal and angular resolution of the system described in this thesis allows C.J. Lo and Dr. Y. Sowa to observe steps at low motor speeds with 350 nm bead attached to the motor via the hook and the filament stub. An example of the trace thus obtained is given in Figure 4.6. The steps are clearly visible and the outcome of a step-finding routine is indicated with a red line. The motor speed in this experiment is stable, allowing C.J. Lo to precisely determine the number of stator units present. In the future this will enable him to answer the important question of relationship between the number of stator units present and the number of steps in the motor rotation.

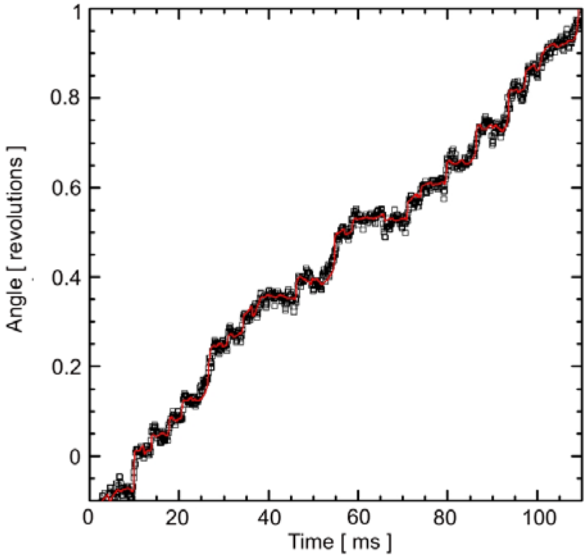

Figure 4.6: Steps in bfm rotation (only one revolution is shown). A 350 nm bead was attached to the motor via a filament stub. Motor rotation was ∼10 Hz. Approximately 27 steps per revolution were detected with a Chung-Kennedy filter in single revolution (shown in red). The Figure was obtained from C.J. Lo.

Chapter 5

F1- ATPase

5.1 Overview

In this chapter a summary of results obtained with the ‘angle clamp’ applied to the *E.coli* and yeast mitochondrial F_1 motor is given.

Initial experiments focused on obtaining a rotation assay with high yield in saturating [ATP] conditions using *E.coli* F_1. This is a sensible starting point since the rotation speed in this condition is several Hz for a 500 nm bead-pair. Upon obtaining a satisfactory protocol for rotation assay preparation, the ‘angle clamp’ was applied to a rotating F_1 molecule. The freely rotating motor was successfully stalled and once released it continued rotating. The result was very encouraging and we subsequently focused on obtaining steps in motor rotation. This would allow us to relate the angle at which we stall the motor to the crystal structure of F_1. Also, any changes in stepping angles before and after applying the ‘angle clamp’ would be a good indication that the motor’s attachment to the surface is not firm enough. The results, encountered problems and conclusions are given below.

Apart from the *E.coli* F_1 motor, yeast mitochondrial F_1 was also investigated. The rotation of this motor was observed for the first time. Although the motor characteristics are expected to be similar to *E.coli* and the *Thermophilic bacillus* F_1, an experimental confirmation of this assumption and possible differences between these motors are of interest.

5.2 *E. coli* F_1-ATPase rotation assay and feedback experiments

In previous chapters, the ‘angle clamp’ system was described, and the performance of the system demonstrated using a bead pair. The angular and temporal resolution achieved is promising for experiments on F_1. The system performance was also tested by applying it to the bfm. The damage issues encountered and discussed raise questions as to the practical use of the technique as applied to F_1-ATPase. These can be addressed by applying the 'angle clamp' to a 500 nm bead pair attached to the rotating γ-subunit of F_1. At saturating [ATP], a 500 nm bead-pair attached to F_1 rotates at ∼3 Hz making it easy to observe. This condition was therefore used to optimize the rotation assay prior to attempting to apply the angle control with feedback. To increase the rotation yield and minimize non-specific sticking to the coverslip surface several different buffers and concentrations of reagents were used during the rotation assay preparation to arrive at the final protocol given in Chapter 2.5. Coverslip surfaces used to attach the engineered His tags on α subunits of F_1 were also changed, and include (in section 2.5 different coverslip surfaces are described in more detail):

- A KOH cleaned coverslip coated with BSA (BSA surface)
- A KOH cleaned coverslip coated with Ni-NTA HRP (HRP surface)
- A KOH cleaned coverslip coated with Ni-NTA silane (silane surface)
- A Cu^2+ chelated surface from Microsurfaces Inc. (Cu^{2+} surface)

On each of these surfaces rotation was observed and the HRP surface was chosen as the best one (giving highest rotation yield and steadiest rotation) for attempting to control the angle of the bead pair with feedback.

Figure 5.1 B shows (X, Y) traces of a typical bead pair rotating on a HRP surface immobilised F_1. Speed of the bead pair is shown in Figure 5.1 C, and bead pair angle vs. time in A.

Figure 5.2 shows control of the angle of a 500 nm bead-pair attached to the rotating γ-subunit of F_1, using the feedback algorithm of Equation 3.5, at saturating ATP concentrations, [ATP]=24 mM. The angles of the bead pair, θ_{bp} and trap, θ_t, are shown in black and red respectively. After ∼5 revolutions with the trap shuttered

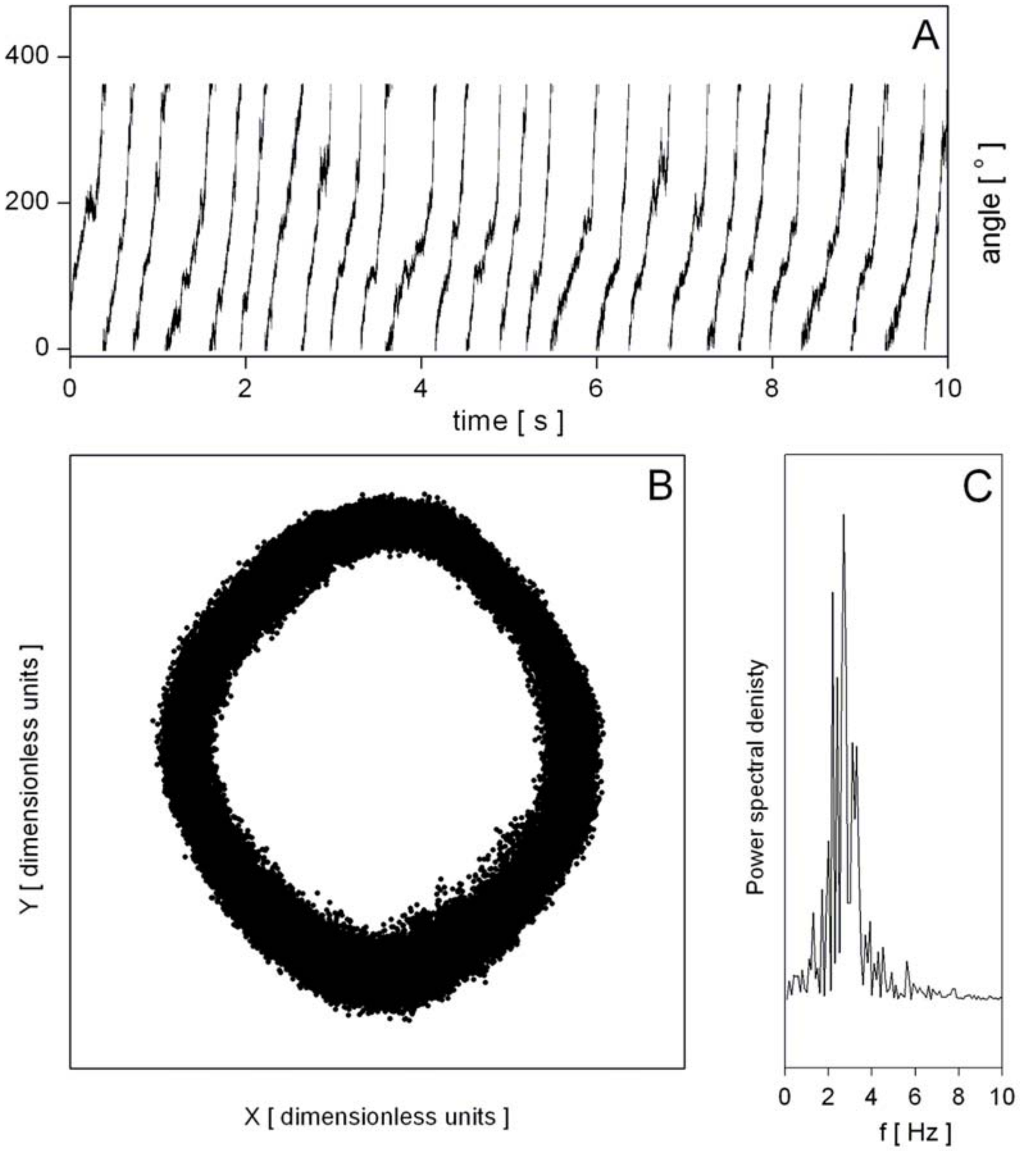

Figure 5.1: *E. coli* F_1 rotation. (A) Angle of the 500 nm bead pair attached to the γ-subunit of F_1 vs. time. (B) QD signal (X, Y) of a rotating bead-pair. (C) Power spectrum of QD signal X, showing the speed of the rotating bead-pair to be ~ 3Hz.

and the motor rotating freely, the shutter is opened and the motor stalled by a fixed trap at $\theta_t = 90°$. Approximately 0.5 s later feedback is switched on for ~2 s, with a set-point of $\theta_t = 90°$, and then switched off again, leaving the trap at $\theta_t = 90°$. Finally, the trap is shuttered and the motor starts rotating as before. This was repeated 8 times for the bead shown and for 12 different bead pairs attached to F_1. Preliminary experiment described demonstrates that the angle of F_1 can be controlled with high accuracy and time-resolution, and that the procedure does not appear to damage the motor.

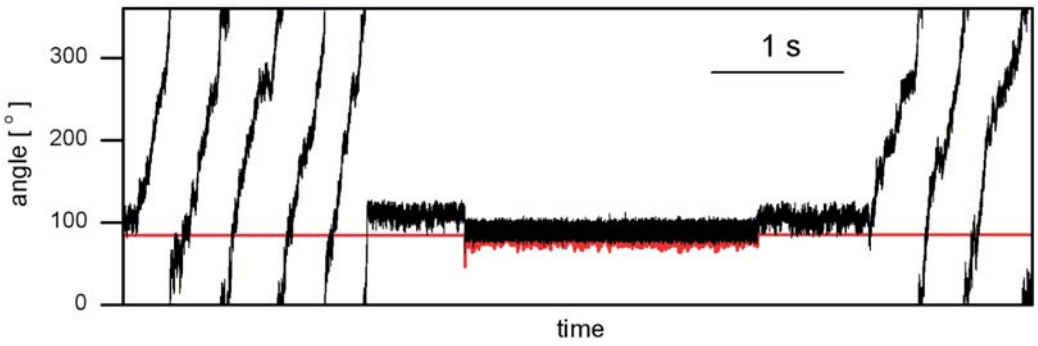

Figure 5.2: Bead pair angle, θ_{bp} (black), and the trap angle, θ_t (red), for a 500 nm bead-pair attached to the rotating γ-subunit of F_1. The bead-pair rotated at the beginning and end of the record when the trap was shuttered. The feedback algorithm of Equation 3.5 was used to hold $\theta_{bp} = 90°$ in the middle of the record. At other times, the bead-pair was held in the trap with no feedback. Feedback parameters $K_p = 0.8$ and $K_i = 0.2$, radius of the trapping laser = 480 nm, laser power = 31 mW.

This particular bead-pair was not calibrated, so an accurate estimate of the stall torque cannot be given. If the trap stiffness is estimated using the Equipartition of Energy and the signal of the stalled motor without feedback, one gets $k_\theta = 438 \pm 116$ pNnm rad^{-2} and a stall torque of $T_{stall} = k_\theta \langle \theta_{bp} - \theta_t \rangle = 74 \pm 20$ pNnm. This is higher than the values of 40 pNnm and 57 pNnm estimated by other methods [91, 250], (perhaps because the stiffness of the intact F_1 adds to the trap stiffness leading to an over-estimate of the latter), but nevertheless promises that future experiments with the calibration protocol performed for each bead pair as described in Chapter 3.3 can provide both the relative torque changes as well as absolute torque value.

There are several other requirements, however, that need to be met, in order to be able to gain detailed information about the working mechanism of F_1 with the 'angle clamp' experiments demonstrated above, these are:

- F_1 needs to be attached firmly to the surface with all available His-tags. This is required because the signature of His tags coming on and off, or F_1 sliding along the surface will be seen in the feedback signal and can mask the motor mechanics.
- The orientation of F_1 on the surface is determined randomly. It would be beneficial to observe steps during F_1 rotation, and thus relate the angle at which the motor was held with feedback to the structure of F_1 (i.e. to the [ATP] dependent stepping angles). Also, the position of the steps in the rotation of the free motor, prior to and after applying the feedback, is useful for determining whether any sliding, or uncoupling of His tags of the surface happened during the experiment.

With the above in mind, [ATP] was lowered to 600 nM, 200 nM, 100 nM and 60 nM. At these [ATP] rotation was observed in a total of 41 F_1 molecules on HRP, silane, BSA and Cu^{2+} surfaces. Clear steps were observed only in one F_1 molecule shown in Figure 5.3. After several rotations, the protein paused and resumed rotation in ~30 s. 120° steps were visible again (Figure 5.3 C), however the position of the steps changed (dotted lines in C show where the position of the steps would be if the motor continued stepping as before the pause, Figure 5.3 B). The shift in the position of the steps after the pause suggests that one or more of the His tags detached and re-attached from the surface, after which the motor resumed rotation. It is possible that this kind of behaviour is frequent and is the reason why clear steps were observed in only one motor protein. Figure 5.4 shows control of the angle of a 500 nm bead-pair attached to the rotating γ-subunit of F_1 as in Figure 5.2 except at 200 nM ATP. The angles of the bead pair (θ_{bp}) and trap (θ_t) are shown

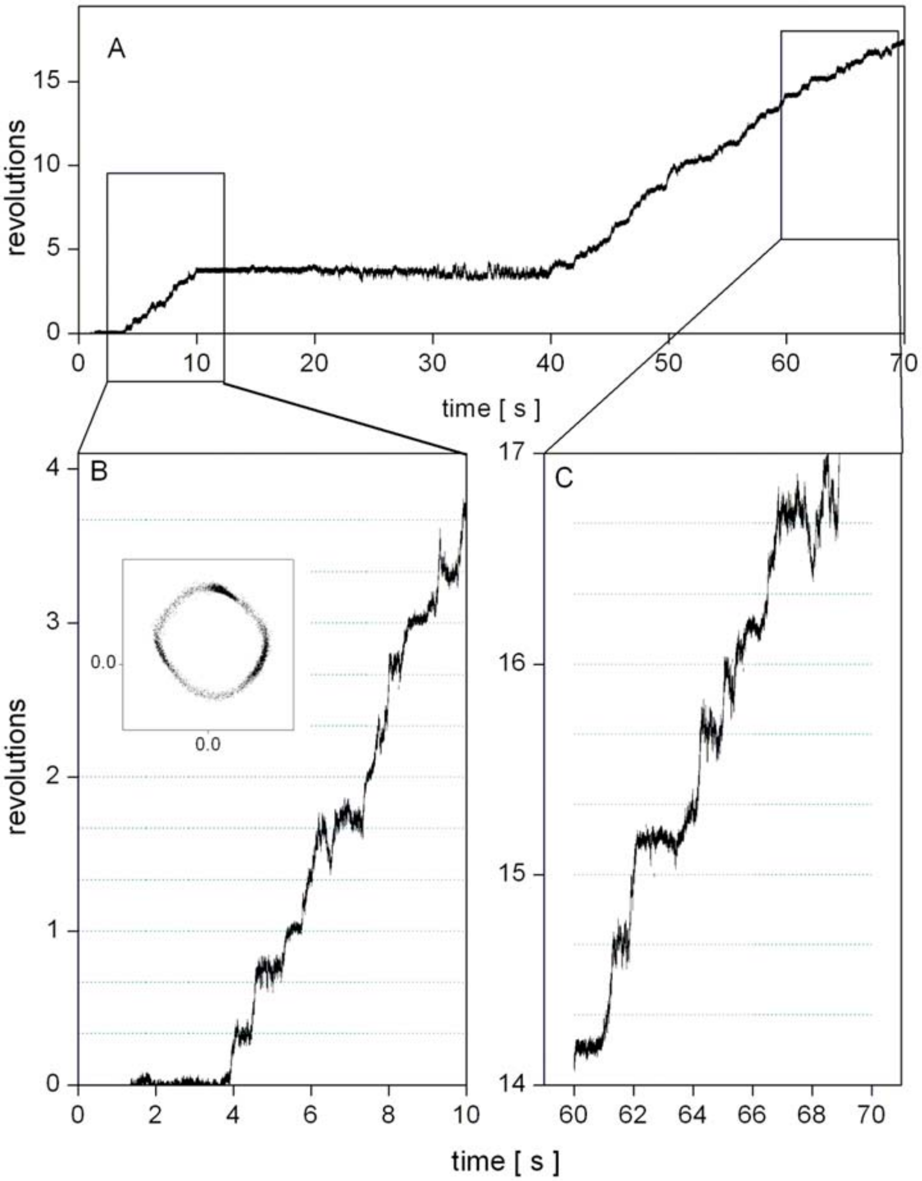

Figure 5.3: Steps in *E.coli* F_1 rotation, [ATP] = 200 nM. (A) Revolutions of F_1, with a 500 nm bead-pair attached to the rotating γ -subunit, vs. time. (B) Close-up of the first 10 seconds of the rotation shown in (A). Dotted lines indicate $\frac{1}{3}$ of a rotation. Inset: QD (X, Y) signal for the rotating bead-pair in first 10 seconds with clearly visible 120° steps (the signal was sampled with 10 kHz, for display in the inset every 20^{th} point is shown.) (C) Close-up of the last 10 seconds of motor rotation. Dotted lines indicate the position of the $\frac{1}{3}$ of one rotation continued from (B). Steps are again visible but the position of the steps has clearly changed after the ~30 s pause visible in (A).

in black and red, respectively. After ∼5 revolutions with the trap shuttered and the motor rotating freely, the shutter is opened and the motor stalled by a fixed trap at $\theta_t = 45°$. Approximately 2 s later feedback is switched on for ∼2 s, with a set-point of $\theta_t = 45°$, and then switched off again, leaving the trap at $\theta_t = 45°$. Finally, the trap is shuttered and the motor starts rotating as before. This was repeated 2 times for the bead pair shown and for 6 different bead pairs attached to F_1 at [ATP]=600 nM, 7 different bead pairs at [ATP]=200 nM, 1 bead pair at [ATP]=100 nM and 7 bead pairs at [ATP]=60 nM. The experiment demonstrates that at low [ATP] concentrations the angle of F_1 can be controlled without apparent damage to the motor. In order to improve the attachment of His tags to the surface

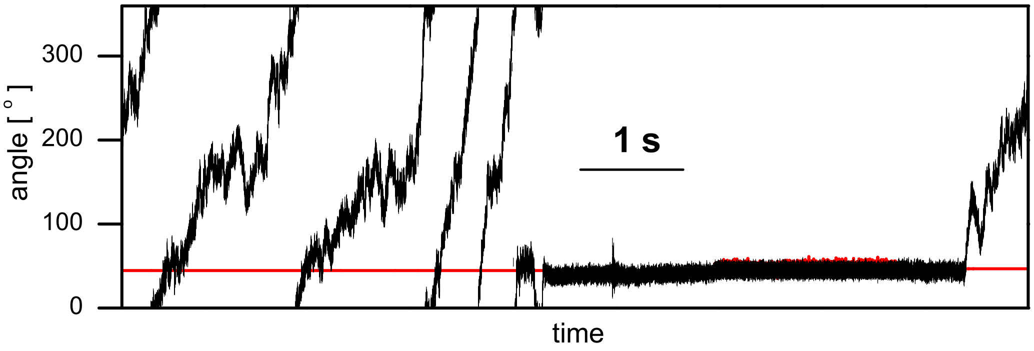

Figure 5.4: Bead pair angle, θ_{bp} (black), and the trap angle, θ_t (red), for a 500 nm bead-pair attached to the rotating γ-subunit of F_1 at [ATP]=200 nM. The bead-pair rotated at the beginning and end of the record when the trap was shuttered. The feedback algorithm of Equation 3.5 was used to hold $\theta_{bp} = 45°$ in the middle of the record. At other times, the bead-pair was held in the trap with no feedback. Feedback parameters $K_p = 0.8$ and $K_i = 0.2$, radius of the trapping laser = 480 nm, laser power = 29 mW.

several strategies are proposed in Chapter 6 for current and future work.

5.3 Yeast F_1-ATPase rotation assay

Rotation of yeast mitochondrial F_1 has so far not been reported. It is likely that the rotation characteristics will be similar to *E. coli* and *Thermophilic bacillus* F_1, but the experimental confirmation of this assumption is missing. It may also reveal some interesting characteristics due to structural differences of yeast F_1 compared to *E. coli* and *Thermophilic bacillus*. Several crystal structure of mitochondrial F_1 have been solved, thus the function of the F_1 system can be studied by genetic, biochemical, x-ray crystallographic and single molecule methods. The yeast F_1 was isolated from yeast mitochondria and genetically modified to incorporate a Cys mutation in the γ subunit, and a His tag on each of the β subunits, by Prof. David Mueller (The Chicago Medical School, USA). Observation of rotation at high and low load, as well as characterization of steps in yeast F_1 rotation will lay the ground work for further studies using specific mutants. These would be engineered in Prof. D. Mueller's group, and would be used to answer the following questions: How does the gamma subunit cause the energy transduction step? How does the binding of nucleotides affect the conformation of the active site?

The rotation of yeast F_1 at saturating [ATP]=24 mM was observed on a BSA surface with a bead pair attached to the γ subunit as the rotation marker. Figure 5.5 B shows (X, Y) traces of a typical bead pair rotating on yeast mitochondrial F_1 as in Figure 5.1. The speed of the bead pair is shown in Figure 5.5 C, and bead pair angle vs. time in Figure 5.5 A. The speed of this bead-pair on yeast mitochondrial F_1 is slightly higher than the *E.coli* F_1 rotation shown in Figure 5.1.

The 'angle clamp' was applied to yeast mitochondrial F_1 at saturating [ATP] in the same manner as for *E.coli* F_1 in Figure 5.2. Figure 5.6 shows control of the angle of a 500 nm bead-pair attached to the rotating γ-subunit of F_1, using the feedback algorithm of Equation 3.5 (as in Figures 5.2 and 5.4). The angle of the bead-pair,

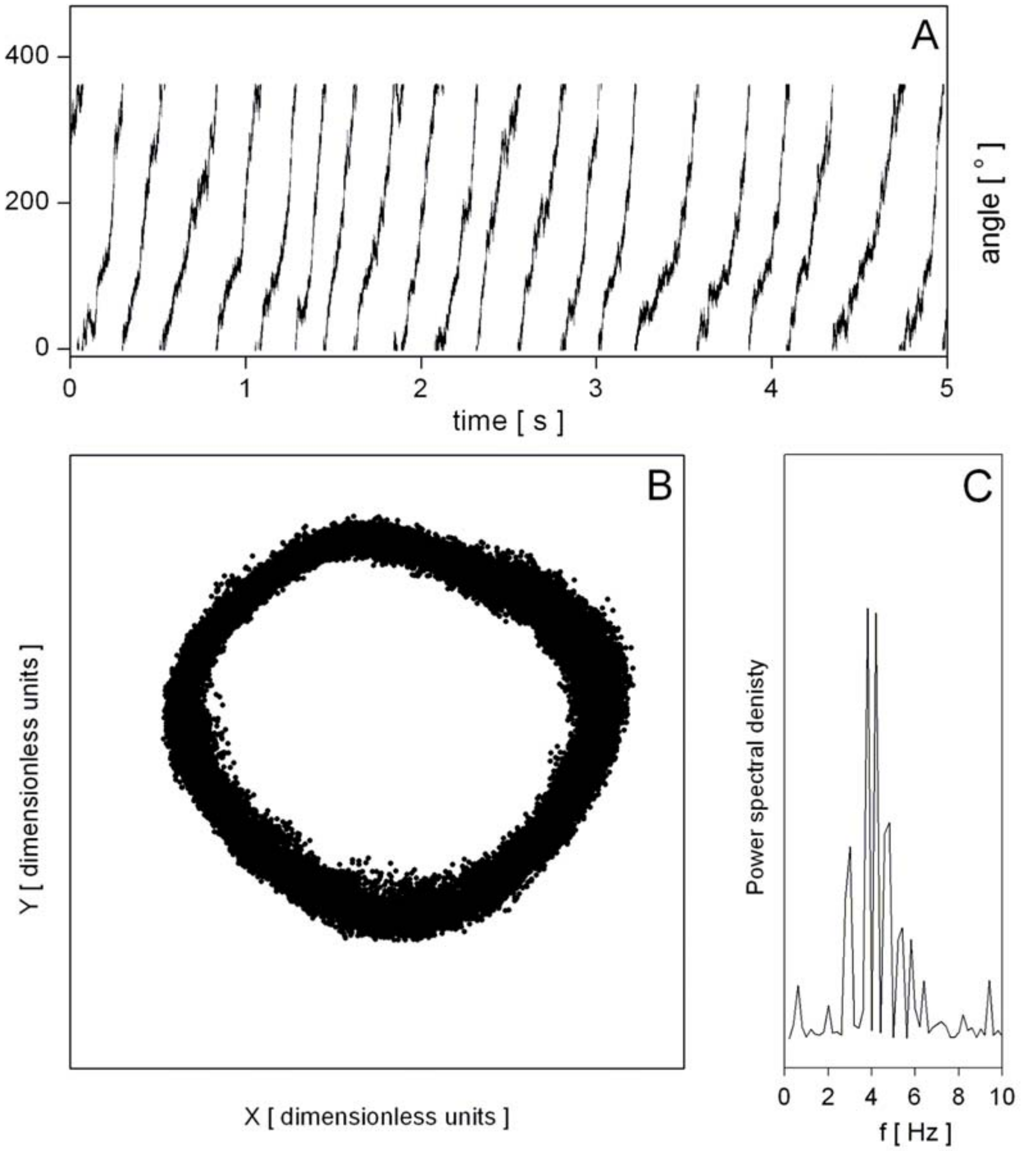

Figure 5.5: Yeast F_1 rotation. (A) Angle of the 500 nm bead pair attached to the γ-subunit of yeast F_1 vs. time. (B) QD signal (X, Y) of a rotating bead-pair. (C) Power spectrum of QD signal X showing the speed of the rotating bead-pair to be ~4 Hz.

θ_{bp}, is shown in black and the angle of the trap, θ_t, is shown in red. The motor was rotating freely before the shutter is opened and the motor stalled by a fixed trap at $\theta_t = 45°$. The feedback is subsequently switched on, with a set-point of $\theta_t = 45°$, and then switched off again, leaving the trap at $\theta_t = 45°$ in (A) and at $\theta_t = 38°$

in (B). Finally, the trap is shuttered and the motor starts rotating as before. The experiment shows that no damage occurs during the 'angle clamp' experiment on yeast mitochondrial F_1 (Figure 5.6 A). Figure 5.6 B demonstrates the sort of 'angle clamp' feedback behaviour one expects at 3 stepping angles of F_1, that could give information about the energy profile of the motor at those angles. However, looking at the X and Y trace of the bead pair shown (inset, right) it is visible that the radius was changing while the angle was controlled. This suggests that the changes observed in the θ_t during the period when feedback was active may correspond to motor mechanics or to the His-tags coming on and off the surface. This example stresses the importance of firm attachment of F_1 by the His tags to the coverslip surface (further discussed in Chapter 6).

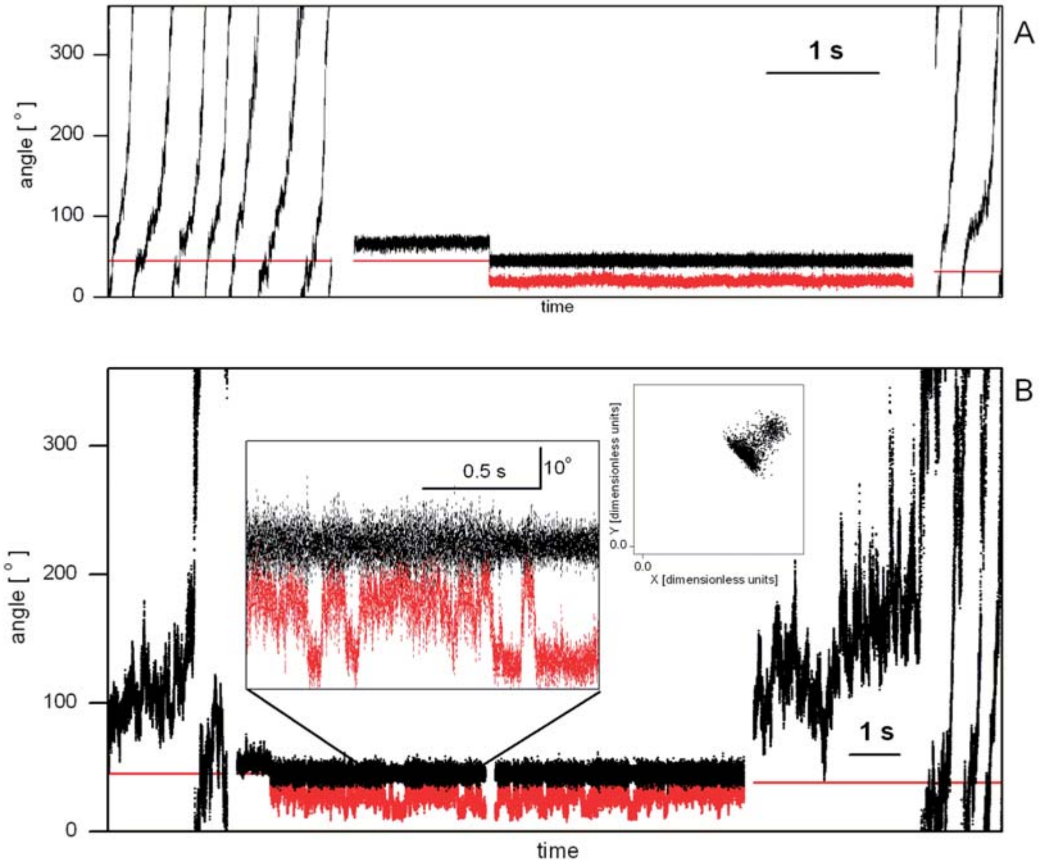

Figure 5.6: (A) Bead-pair angle, θ_{bp} (black), and the trap angle, θ_t (red), for a 500 nm bead-pair attached to the rotating γ-subunit of yeast F_1 at saturating [ATP]=24 mM. The bead-pair rotated at the beginning and end of the record when the trap was shuttered. The feedback algorithm of Equation 3.5 was used to hold $\theta_{bp} = 45°$ in the middle of the record. At other times, the bead-pair was held in the trap with no feedback. Feedback parameters $K_p = 0.8$ and $K_i = 0.2$, radius of the trapping laser = 360 nm, laser power = 30 mW. (B) As in (A). Left inset shows a close-up of the θ_{bp} and θ_t trace. Right inset shows X and Y trace, obtained from the QD, of the bead-pair for the same section shown in the inset on the left. The feedback trace corresponds to what one might expect for 3 steps with 120° rotation per step at low [ATP]. However, the radius of the bead pair changes thus it is possible that the trace corresponds to the His-tags on F_1 detaching and re-ataching of the surface.

CHAPTER 6

DISCUSSION, CONCLUSIONS AND FUTURE WORK

A novel system for the study of rotary molecular motors has been reported in this thesis. A polystyrene bead duplex has been used as a handle to apply external torque to rotary molecular motors with an optical trap designed to act as an 'angle clamp'. This technique achieves high temporal and angular resolution as well as great flexibility in control. Comparison of the 'angle clamp' performance with other available systems (discussed in Chapter 1.3) is given in Table 6.1.

As well as presenting the design, construction and calibration details of the 'angle clamp', application of the system to the two rotary molecular motors has been presented. In the case of *E.coli* F_1, the purification protocol has been set up and the rotation assay protocols investigated. Collaborative work on yeast mitochondrial F_1 has also been started. It has been shown that stalling F_1 with the 'angle clamp' does not damage the motor, and that the attachment of F_1 to the surface presents the biggest problem for these kinds of experiment. Several steps are planned to overcome this problem (some are in fact on going rather than future work) and are given towards the end of this chapter.

The performance of the system was demonstrated on the bfm as well. The mechanical damage appeared to be the biggest problem. In the experiment where the motor speed was controlled, for most of the cells observed, significant damage occurred during the fine alignment procedure. This was indicated by a reduction in the speed of the free motor. The time it takes for fine alignment varies from cell to cell, but it is usually on the order of 1 min. In cases where the trajectory of the bead pair attached to the motor was almost circular the fine alignment procedure may not be necessary and might be omitted in the future. The torque exerted by the trap is proportional to the difference between the trapping laser angle and the bead-pair angle during forced rotation. If the problems of alignment and mechanical damage can be solved, the method of Figure 4.3 will allow measurement of the torque-speed relationship of the flagellar motor under a wide range of different conditions, especially when the motor is driven backwards or forwards up to and beyond the zero-torque-speed regime which are not accessible without the application of external torque. The technique places no special requirements on the conductivity of the medium, allowing for example experiments in the relatively high ionic strengths that are suitable for study of sodium-driven flagellar motors.

Finally, when the system is used for detection, it offers high spatial and temporal resolution and was used for experiments on sodium driven bacterial flagellar motor, and a switching proton driven bacterial flagellar motor, giving several valuable experimental results. The switch time distribution obtained gives strong evidence that the switching event does not occur instantaneously and can be explained by the 1-D Ising model.

The interval time distribution obtained by R. Branch for CCW to CW bias in the range of 0.8 to 0.9 suggest an exponential. This is interesting with respect to the result obtained by Korobkova et al. [191], which shows that the probability density of switch time intervals is gamma distributed. The reasons for this discrepancy could be one of the following: *(1)* The [CheY-P] was not controlled by the chemotaxis network in Korobkova et al. experiment; instead a mutant with stably pre-expressed CheY** from an inducible vector was used. If the switching behaviour of the wild type motor and the mutant are different, the wild type behaviour is of greater relevance for in *vivo* function. *(2)* Korobkova et al. used 500 nm beads but did not shear the filaments in their rotation assay and report that their motors never stop rotating and exhibit only CW and CCW rotational states. It is possible that non-sheared filaments introduce filtering in an unpredictable manner (the length of the filament varies), causing them to miss slowdowns and pausing events. *(3)* The sampling rate they used was 100 Hz giving them 10 ms resolution.

To investigate which of the possibilities given above causes us to observe a different interval distribution, we plan to degrade our data according to the suspected filtering present in the Korobkova et al. experiment. Also, more data needs to be obtained in order to investigate the interval time distribution for all CW and CCW biases. Finally we plan to obtain the data with the mutant carrying a plasmid with IPTG inducible CheY** for comparison to the wild type data[*].

Experiments where 200 nm beads were attached to the motor allowed C. J. Lo to observe that in the low load regime ΔpNa and $\Delta\psi$ contributions to the *smf* are not equivalent. These experiments have also allowed him to determine the torque-speed curve for a chimearic motor in low load regime. Using 350 nm beads enabled C. J. Lo and Dr. Y. Sowa to observe steps in motor rotation under controlled conditions (known pNa, $\Delta\psi$ and stable rotation at given speed), a good indication of the number of stator units present.

As seen in Table 6.1 the calibration of bead-pair stiffness needed to obtain absolute torque values in this optical trap has proven to be the most difficult problem (section 3.4.3). There are several sources of angular and bead pairs variations reported in this thesis. To explain and understand these variations, I look at the torque (**T**) exerted on a motor via a bead pair in a linearly polarized optical trap This can be written as

$$\mathbf{T_{trap}} = \mathbf{T_{lever}} + \mathbf{T_{shape}} + \mathbf{T_{polarization}} \tag{6.1}$$

where $\mathbf{T_{lever}}$ is the combined effect of the linear force on the bead-pair and the reaction force at the motor, $\mathbf{T_{shape}}$ is the alignment effect of a non-spherical trap on a non-spherical particle, and $\mathbf{T_{polarization}}$ is a torque acting to align the long axis of the bead pair with the polarization vector of the laser beam. Referring to Figure

---

[*] I am currently working on obtaining this mutant with Dr. George Wadhams in Prof. J. Armitage's group

3.6 A, reproduced below in Figure 6.1, to define x, y and z axes, one can expect $\mathbf{T_{shape}} = (0, T_{y,shape}, 0)$, as single-beam optical traps are typically extended in the z direction and particles align with their long axes parallel to the optical axis of the trap [234, 235, 236], and $\mathbf{T_{lever}} = (0, 0, -k_{lever}(\theta_{bp} - \theta_t))$. When a bead-pair attached to a molecular motor is held in feedback, the trap torque will balance the torque due to the bead-motor-surface link: $\mathbf{T_{trap}} = \mathbf{T_{link}}$. Considering the z-components:

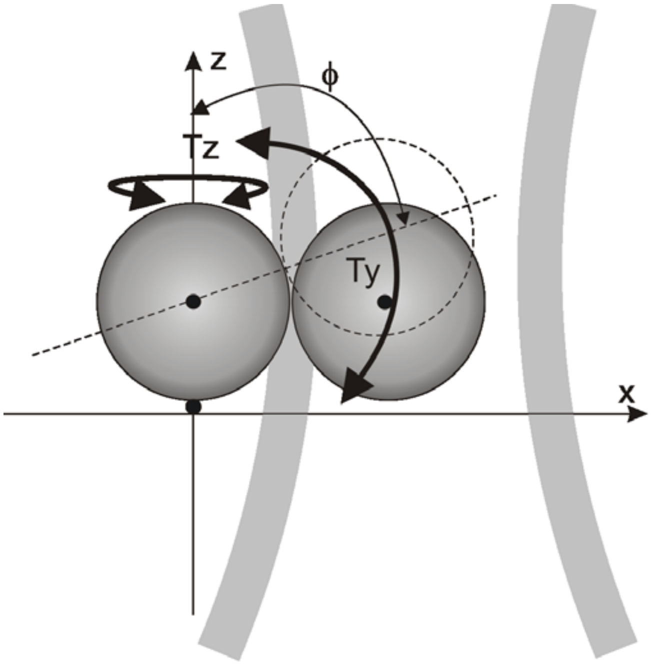

Figure 6.1: Schematic diagram of a bead-pair attached to a surface by a motor at $x = y = z = 0$ and held by the optical trap

$$T_{z,link} = -k_{lever}(\theta_{bp} - \theta_t) + T_{z,polarization} = -k_\theta(\theta_{bp} - \theta_t) \tag{6.2}$$

In an ideal system, $T_{z,link}$ would be dominated by the motor torque which is being investigated, k_{lever} would be a constant, and $T_{z,polarization}$ would negligible, in which case k_θ would also be a constant. In this case

$$T_{motor} = -k_\theta(\theta_{bp} - \theta_t) = -k_{lever}(\theta_{bp} - \theta_t) \tag{6.3}$$

In practice, however, $T_{z,link}$ and k_θ may vary with θ_{bp} for the following reasons.
(1) k_{lever} will vary with angle due to variations in laser intensity at different trap positions, differences between trap stiffness in x and y, and misalignment of each bead pair leading to different lengths of lever arm at different angles.
(2) $T_{z,polarization}$ is expected to have a period of 180° in θ_{bp}; however, theoretical predictions show that higher periodicities might be possible depending on the shape and size of the particle [269, 270].
(3) The most likely contributor to $T_{z,link}$, other than T_{motor} is direct interaction between the bead-pair and the surface, in parallel with the linkage via the motor. The angular dependence of this interaction is impossible to predict, and may vary from bead to bead, and may depend upon T_y. Minimizing T_y by selecting "flat-rotating propeller" bead-pairs (as discussed below) is expected to minimize this effect, and the observation of bead-pairs performing free RBM indicates that $T_{z,link}$ is negligible for many bead pairs in the absence of any trap torque. Regardless of the exact causes of angular variation in trap torque, the measurements of Chapter 3.4 indicate that variation is considerable and not predictable, and that trap stiffness must be calibrated for each bead-pair if absolute torques is to be measured. There are two reasons to minimize the alignment torque, T_y. As well as the possible affect on $T_{z,link}$ discussed above, T_y will be balanced by an opposing force that consists of a vertical force acting on the motor multiplied by the lever-arm between the motor and a point of contact between the bead and the surface. The lever arm is likely to be very short, on the order of the size of the motor, and thus the force on the motor may be large even for relatively small T_y. T_y consists of $T_{y,shape}$ and $T_{y,polarization}$, both of which depend upon the angle ϕ (Figure 3.6 A). As this angle increases, bead-pairs change from vertically stacked beads, $\phi = 0°$, to flat-rotating propellers, $\phi = 90°$, and the radius of the circle described by the center of the outer bead increases from zero to the bead diameter (Figure 3.6 B). At $\phi = 90°$ a bead pair is in an unstable

equilibrium and $T_y = 0$ [235, 269, 270]), which is the reason for choosing flat-rotating propellers in ‘angle clamp’ experiments. For bead pairs attached to the bfm or F_1, these are common. The height of a single 500 nm bead can be judged by eye with an accuracy of ∼30 nm, corresponding to ∼3° in ϕ. The accuracy in determining ϕ may be improved since the image of the two adjacent beads is compared (Figure 3.6 B). Others have estimated $T_y = \sim 300$ pNnm at $\phi = 87°$ for chloroplasts of radius 500 nm and length 2 μm (in a 1064 nm laser trap at 30 mW laser power, [235]). T_y is expected to be on the order of tens of pN nm or less in the ‘angle clamp’ experiments. As well as the vertical force opposing T_y and the lateral force completing the couple $\mathbf{T_{lever}}$, the motor may experience a radial force pulling the bead pair towards the centre of the trap. In these experiments, the trap moves at a radius similar to the bead diameter, and therefore a small radial force is expected, but whatever the actual values of the vertical and horizontal forces on the motor, the immediate resumption of spinning when the trap is shuttered illustrated in Figures 5.2, 5.4 and 5.6 demonstrates that they are small enough not to damage F_1.

As mentioned previously the attachment of F_1 to the surface presents the biggest problem for obtaining the detailed information on the motor’s energy profile. The following steps are either on going work or are planned to overcome this problem:
(1) A silane surface has proved to be the optimal in reports by other researchers [109, 111], but the surface quality can vary from preparation to preparation (personal communication with Dr. Y. Sowa and Prof. H. Noji*). Only 4 proteins were observed rotating at lower [ATP] (200 nM) on a silane surface and the traces obtained showed no stepping. This is probably due to the detachment and re-attachment of His tags, but it is also a possible indication that the surface was not adequately prepared. New protocols for silane surface preparation have been obtained from H. Hosokawa

---

*Personal communication with Dr. R. Berry and Dr. Y. Sowa which include several improvements. The first obvious step is to observe more low [ATP] rotation on silane surfaces prepared in this manner.

(2) The second step planned for future work is based on the assumption that His tag detachment is the primary cause for the lack of steps in the motor rotation. The dissociation rate of 6-His tags from Ni-NTA is ∼1 s^{-1} [271, 272]. On the other hand the dissociation rates of bis-NTA, tris-NTA and tetrakis-NTA are significantly smaller: -0.01 s^{-1}, 0.005 s^{-1} and 0.01 s^{-1} respectively. Bis, tris and tetrakis-NTA are engineered to have two, three or four binding sites for His tags. If instead of a 6-His tag, a 10-His tag is used, the time constants improve further: 0.005 s^{-1}, 0.0005 s^{-1} and 0.005 s^{-1} for bis, tris and tetrakis-NTA, respectively [271]. The higher dissociation time constant for tetrakis-NTA is attributed by the authors in [271] to its topology (as shown in Figure 6.2 A). Using a 10-His tag linker on α subunits and a coverslip surface covered with tris-NTA should significantly improve the attachment of F_1 to the surface. 10-His is currently constructed by Hiroyuki Hosokawa in the group of Prof. M. Futai. For functionalizing the coverslip surface with tris-NTA, DNA will be used as a linker. Currently tris-NTA is constructed by Wei-Ming Ho in collaboration with Dr. Achillefs Kapanidis, Clarendon Laboratory, University of Oxford. Using tris-NTA on DNA allows the option of constructing specific 2-D DNA structures, suitable for attaching 10-His tags on F_1 and further increasing the rotation yield. A starting point would be an already constructed structure by Dr. John Malo [273] as shown in Figure 6.2 B. Attaching DNA arrays to the coverslip as well as further developing arrays of adequate base lattice and size would be carried out in collaboration with Dr. J. Malo working in Prof. Andrew Turberfield group, Clarendon Laboratory, University of Oxford.

(3) Possible improvement in the detection of stepping motors could be achieved by using smaller beads. So far a few experiments at high [ATP] were carried out using smaller bead pairs (300 nm and 200 nm). Rotating enyzmes with 300 nm bead-pairs

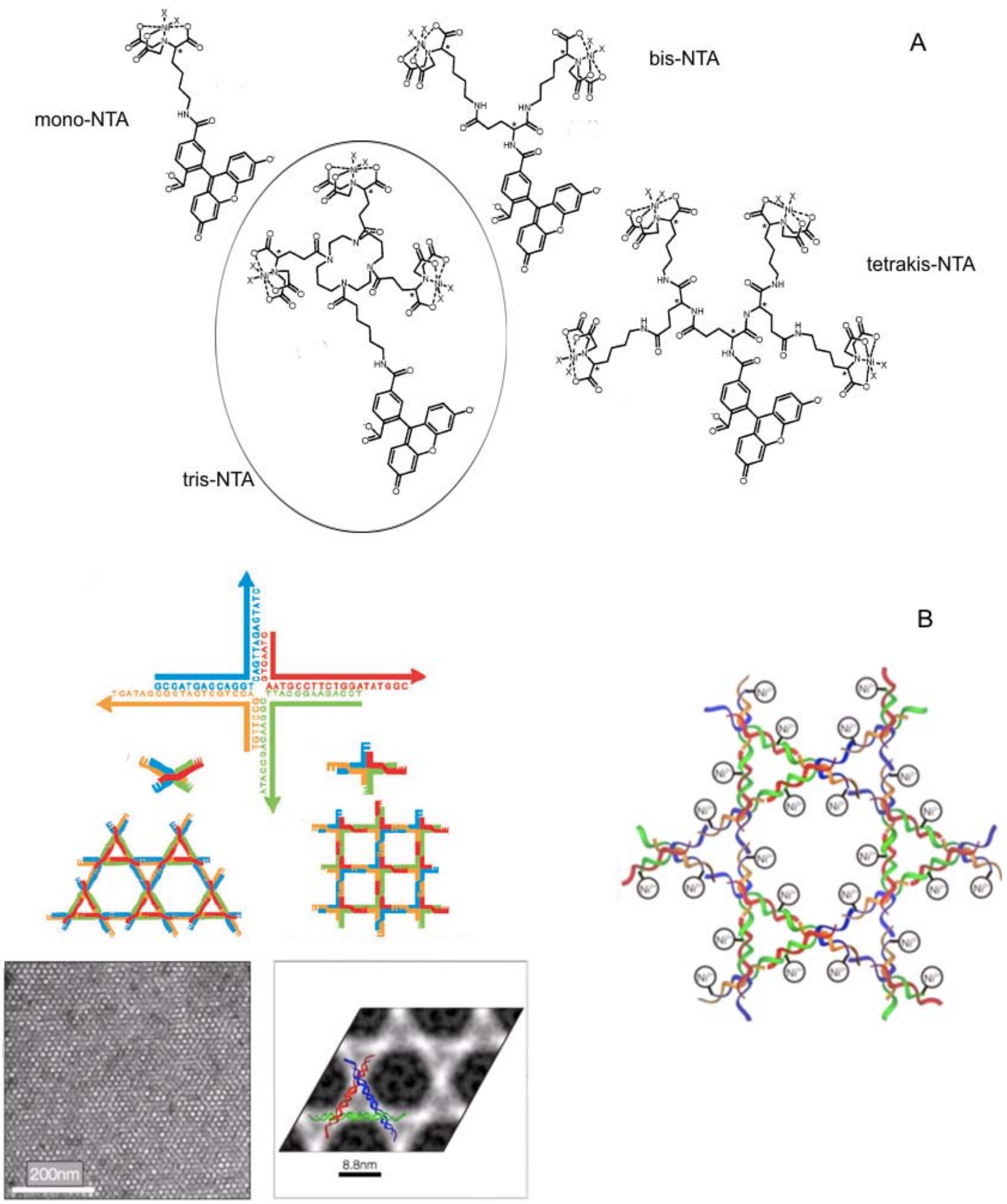

Figure 6.2: (A) Chemical structure of the carboxyfluorescein-conjugated chelator heads is shown. Figure is taken from [271]. Mono, bis, tris and tetrakis-NTA heads are indicated. These need to be constructed on a DNA molecule and consequently assembled in a 2-D array as shown in (B). (B) is taken from [273] and [274].

attached were recently observed by Thomas Bilyard but no rotating enzymes were observed with 200 nm bead-pairs.

To conclude I would like to mention a few ideas and possible directions for future research opened by the work done as part of this thesis. The model given in section 1.2.2 for the bacterial flagellar motor suggest that the soft elastic linkage between the motor and the viscous load used to observe the rotation is the reason behind the shape of the torque-speed curve (Figure 1.9). It would be interesting to be able to confirm this by stiffening the hook. The hook stiffness can be measured with the system presented in this thesis. Further more the response time of the bead attached to the motor via bacterial flagellar motor hook can be increased by increasing the hook stiffness, facilitating observation of steps in the presence of two or more stator units, together with the step dwell times and backward steps. Also, if it is possible to increase hook stiffness, controlling the angle of the bead pair with feedback can give information on the energy profile of the motor at a given angle. Finally, mechanism of switching can be further explored by increasing the response time of the switch time observation by holding the bead-pair at a certain angle with the 'angle clamp' feedback.

Since the system can be used to obtain detailed information on the working mechanism of the F_1-ATPase, some other unanswered questions can be addressed as well. For example, hydrolysis seems to be insensitive, while F_1 synthesis coupling efficiency is sensitive to the presence of ϵ subunit. How does the energy profile of the protein with and without ϵ subunit vary with angle? Is it different to the hydrolysis direction, and if so, in what way?

As well as F_1 purification, F_1F_o purification was learned as part of the 2003 visit to Prof. M. Futai, Osaka University, Japan. It was adopted to suit the conditions of the lab in Oxford and is given in Appendix C. In Chapter 1, I have given an introduction to the F_o motor and research carried out on it. Controlling the voltage across the membrane containing an F_o motor is certainly a challenge, but since little is known about this motor the challenge is a very rewarding one. Since F_1F_o has been successfully purified, the future research of F_1F_o and F_o motor in this lab is possible.

System	Characteristics and Advantages	Disadvantages
'Angle Clamp'	up to 1° angular resolution; up to 2° angular control precision; angle control with 1-2 ms time resolution; up to 1 kHz rotation rates; flexibility of implementing feedback algorithms; clocked output signals	Each individual bead pair needs to be calibrated at the end of the experiment for absolute torque measurements; the torque is applied on the motor in form of linear force to the bead pair resulting in observable mechanical damage to the bfm
Magnetic tweezers	up to 5° angular control precision, angle control with several seconds time resolution	Calibration of the absolute torque is complicated by the non-uniform nature of magnetic beads
Electrorotation	up to 100 Hz rotation rates; the applied torque is precisely know; the torque is applied directly to the cell body	Conductivity of the media is important placing a limit on the salt concentrations of the media used
Birefringent particles	rotation rates of usually 10-20 Hz; the torque is applied directly to the microscopic particle	low rotation rates; the need of a birefringent particle (potential problems with attaching the particle to the motor)
Asymmetrically shaped particles	rotation rates of typically few Hz; the torque is applied directly to the microscopic particle	low rotation rates
Absorbing particles	rotation rates of few Hz; the torque is applied directly to the microscopic particle	low rotation rates; heat absorption
Rotation within optical tweezers	rotation rates of few Hz, great flexibility of control	low rotation rates; complicated setups
Microfabricated chiral scattering particles	rotation rates of few Hz, exciting to watch	low rotation rates; need for specially manufactured particles

Table 6.1: Performance of the system presented in this thesis compared to the other available systems that allow external torque application.

Appendix A

An example of a QuVIEW program

An example of a typical program written in QuVIEW is given in figure A.1. The

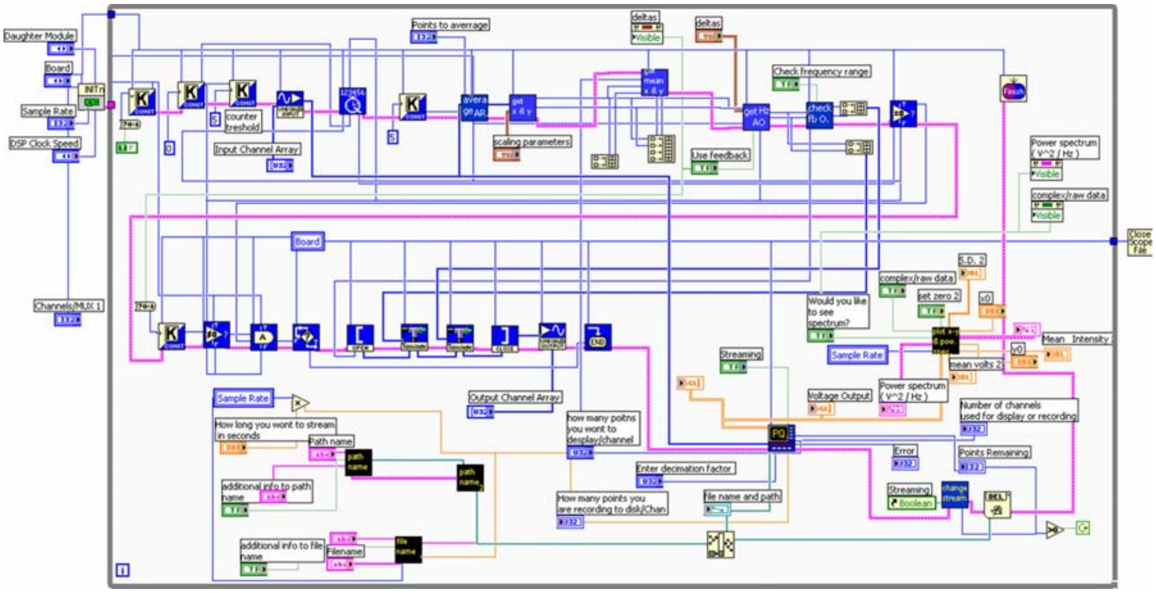

Figure A.1: A typical program written in QuVIEW. The program inputs 4 voltages coming from the quadrant detector, calculates the right voltage level to be outputed (based on the desired feedback scheme), checks whether it corresponds to the right frequency range, displays the position of the trapped object in dimensionless units and saves data.

'INTn' QuVIEW Virtual instrument (Vi) outside of the LabView continuous loop in Figure A.1 initializes the DSP. Once the initialization was performed the sequence, as shown in the LabView loop, is sent to the DSP by the host computer. The sequence is executed on the DSP even if the program shown is stopped in LabView. The new sequence can be sent to the DSP and executed only after the DSP has been re-initialized. All the blue icons in Figure A.1 represent QuVIEW Vis that are executed only on the DSP. The blue and white Vis (for example; the first three Vis in the LabView loop) communicate both with the DSP and the host computer and are used to send the values of the user defined variables in LabView to the DSP. The fourth Vi inside the LabView loop is the analog input Vi, and the fifth Vi is crucial to set the timing on the DSP. The timing based on the board's processor clock and can be set as a counter with an ouput that indicates when the counter has reached the desired value. The blue 'PQ' Vi in the second row is the Vi that enables the display of inputed values on the host computer; it also enables saving of the data on the DSP to the host computer (in a QuVIEW specific format). This Vi always has to be the last in the sequence before the 'Finish' Vi. The order of the Vis is set by the thick line ('error' line) coming in and out of the Vis and shown in pink.

For the purpose of feedback and detection experiments the following programs have been written:

(1) Detection only programs. These programs input QD voltage, display and save this voltage, and were used in section 4.3.

(2) Programs written for the purpose of calibrating the QD signal. These programs move the AODs or the nanocube in a grid and save the output signal as well as the inputed QD signal (used in section 3.3.1).

(3) Programs for the 2-D X and Y feedback used to control the piezo-electric stage. These are the same programs as used in the section 3.3.3 but for the control of the piezo-electric stage, not the AODs. They can be particularly useful when longer

detection experiments are needed and drift becomes a problem.

(4) Programs for the 2-D X and Y feedback used for the control of the AODs (see section 3.3.3).

(5) Programs used to control the speed of the bacterial flagellar motor (used in section 4.2.1).

(6) Programs used for the angular trap stiffness calibration (used in section 3.4.3).

(7) Programs for the 'angle clamp' feedback (used in section 3.4.2, 4.2 and Chapter 5).

Appendix B

Analog to digital converter

The analog to digital converter was designed and produced with the help of the Central Electronics Workshop (Department of Physics, University of Oxford) for the AODs' driver (DDS), with 19 digital lines for control of both X and Y AOD. This DDS had to be replaced after a fault was found (see section 2.1.3). The new DDS was received by the manufacturer after the ADCs for the original DDS were already produced by the Electronics Workshop.

Figure B.1 gives the arrangement of bits used to control the original DDS. For this DDS the 25-pin connector coming out of the analog to digital converter corresponded to the input 25-pin connector on the DDS. The replacement DDS was significantly different, both in resolution and in the arrangements of the control bits on the 25-pin output connector. The re-arrangement scheme for the new DDS is given in Figure B.1 B. The re-arrangement was a much shorter but nevertheless satisfactory option; the alternative would be designing and producing a new analog to digital converter by the Central Electronic Workshop. Figures B.3 and B.2 give the layout of the ADC.

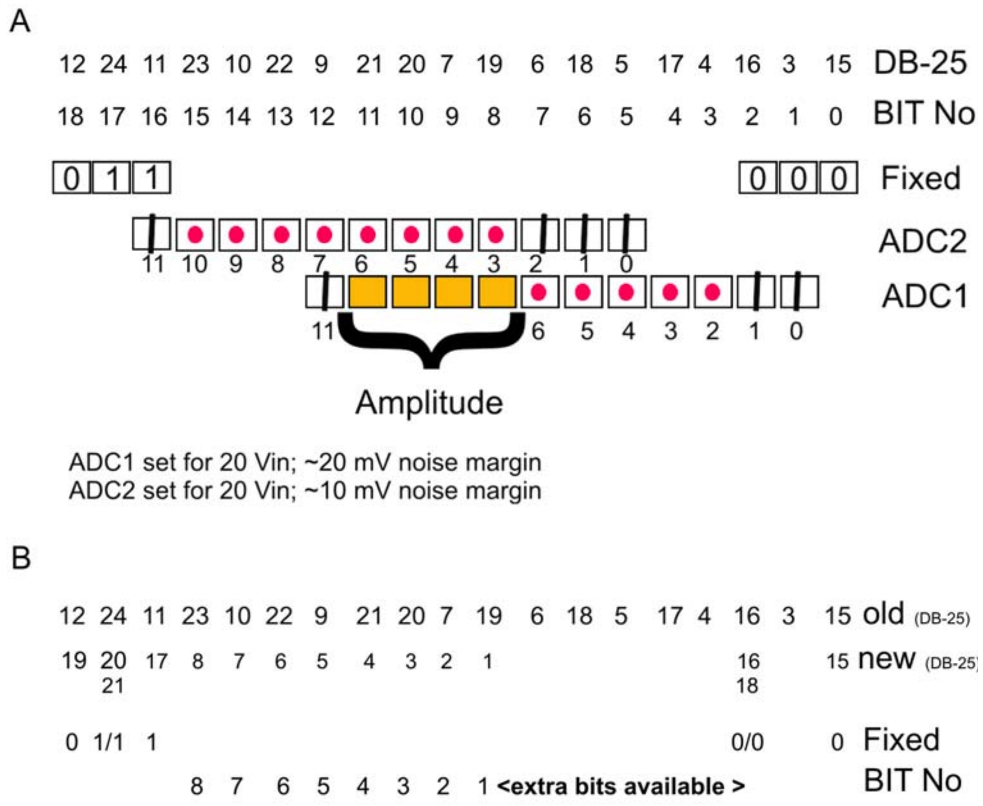

ADC1 set for 20 Vin; ~20 mV noise margin
ADC2 set for 20 Vin; ~10 mV noise margin

Figure B.1: Bit arrangement. (A) As designed for the DDS driver with 19 digital control lines for both the X and Y AOD, and with ∼300 Hz resolution. Different bits on two ADCs are labeled. Used bits are indicated with red dots and black lines indicate unused bits. Fixed bits are shown as well. The second line of 19 bits corresponds to the bits used by the X or Y channel of the AODs driver. The first row corresponds to the pins on a 25 pin connector (X or Y channel), which is the output of the analog to digital converter as well as the input of the DDS. (B) As re-arranged for the DDS with 15 digital channels for both X and Y control and with ∼15 kHz resolution. The output 25 pin connector on the ADCs no longer corresponds to the 25 pin connector on the DDS. The layout of the new connector is given in a second row. Fixed bits as well as 8 bits converted by the ADCs are given in two rows below. The bits marked in brackets are not used for the fastest feedback programs but are available when the speed of the program is not a primary concern and when a larger movement in both x and y-axis is required (see Chapter 2.1.3. for further details).

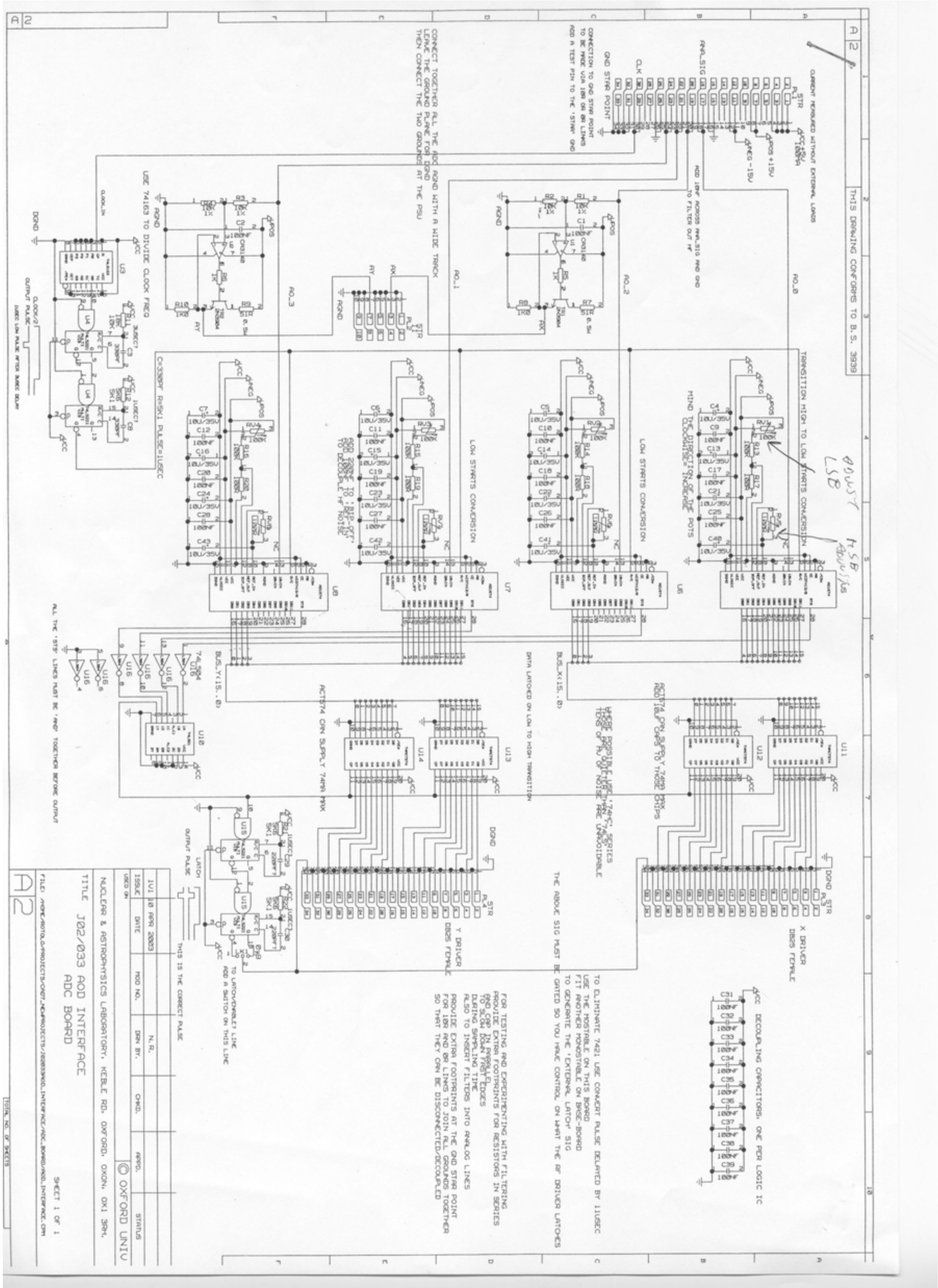

Figure B.2: Layout of the ADC board as designed by the Electornics Workshop, Department of Physics, University of Oxford.

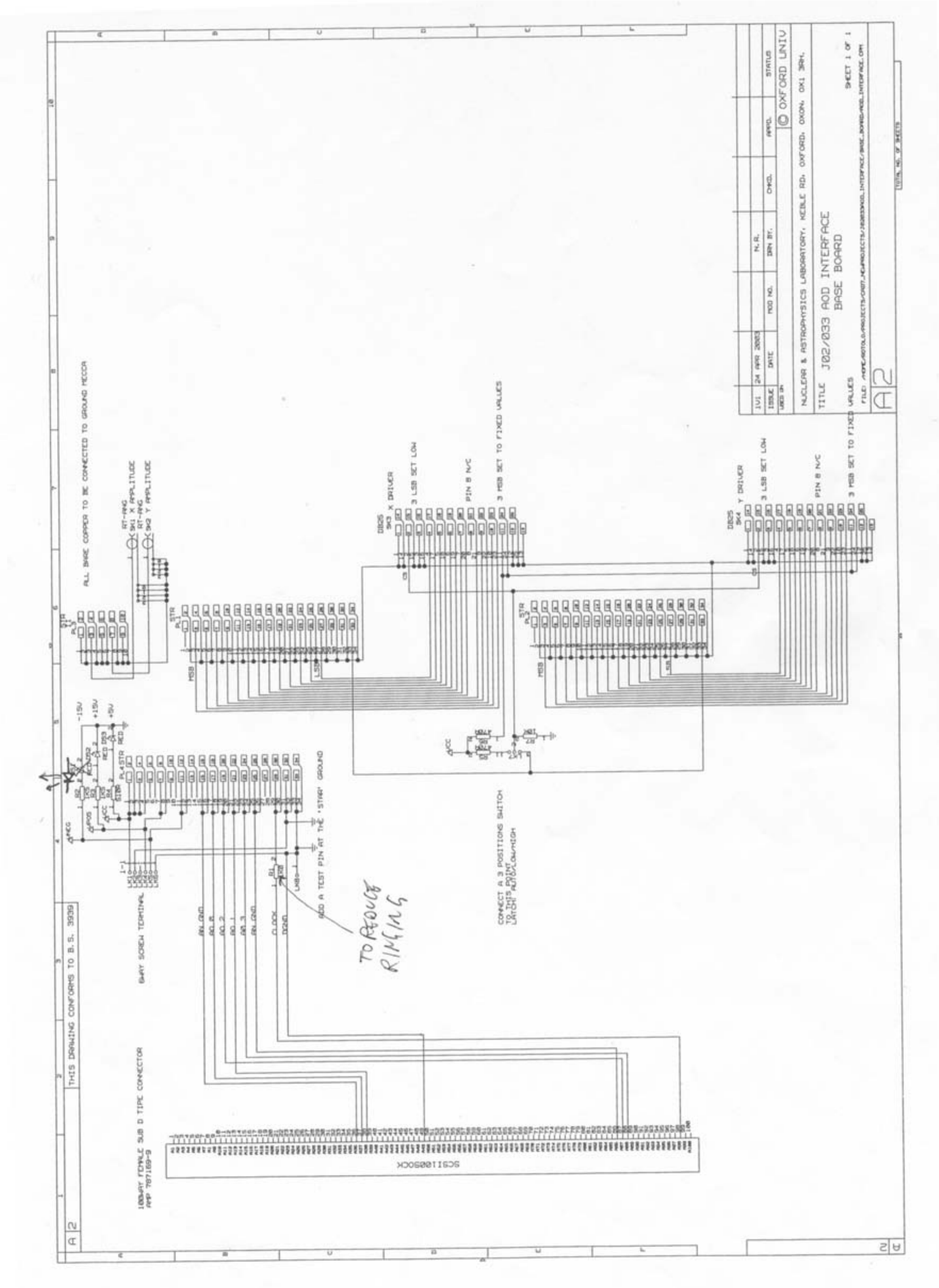

Figure B.3: Base board of the ADC as designed by the Electronics Workshop, Department of Physics, University of Oxford.

APPENDIX C

F_1F_o purification

E.coli F_1F_o-ATPase purification is based on protocols obtained from Professor Masamitsu Futai and is in principle very similar to the F_1-ATPase purification protocols given in Chapter 2.4.

F_1F_o, with six histidine residues introduced into c subunits and the transcarboxylase biotin binding domain in the β subunit, was constructed in the pBMU13S-βTC/cHis plasmid (modified from the pBWU13 plasmid [275]) in the DK8 bacterial strain [58]. The F_1F_o was purified in four steps (each taking $\sim$ one day). First two steps involve cell growth, with a cell pellet, usually of $\sim$1 g, as a result. At the end of the third step, disrupted cells are collected as membrane fragments containing F_1F_o as well as other membrane proteins. During the fourth step F_1F_o is separated from the membrane by detergent and collected by glycerol gradient centrifugation.

(1) Step one is only slightly different from step one of F_1 purification. The difference is in the Tanaka medium which now containes 2 μM biotin. Since the F_1F_o has a transcarboxylase binding domain the biotinylation is now part of the growth step. Step *(2)* and *(3)* are the same as with the F_1 purification. Step *(4.)* is the one with the most significant difference compared to the F_1 purification protocol. The

suspension of membranes was diluted with Membrane Wash buffer (50 mM Tris-HCl, pH=8 at 4°C, 2 mM $MgCl_2$, 10% clycerol, 0.5 mM EDTA, 1 mM DTT), ratio 10 mg of protein to 500 μl of Membrane wash buffer, and centrifuged for 20 min at 370 000 g average, at 4° C (rotor Type TLA 100.2 at 100 000 rpm in Optima TL ultracentrifuge Beckman Coulter). The precipitate was suspended in 0.4 ml buffer A (20 mM MES/Tris, pH=7 and 5 mM $MgCl_2$) with 20 μl of 2 M KCl and 110 μl 10% $C_{12}E_8$ (final concnetrations 100 mM and 2% respectively) and incubated on ice for 10 min. The suspension was then centrifuged for 1 hour at 180 000 g average, at 4° C (Type 70.1 TI rotor for 51 200 rpm in L-XP Beckman Coulter ultracentrifuge). After centrifugation 917 μl of supernatant was layered to a glycerol gradient (prepared in ultra centrifuge tubes by layering 30, 25, 20, 15 and 10 % (w/V)) glycerol solution (in 10 mM MES/Tris pH=7.0, 5 mM $MgCl_2$, 0.01% $C_{12}E_8$, 0.5 mM DTT, 5 μg/ml Leupeptin and 5 μg/ml Pepstatin A) and centrifuged for 5 hr at 250 000 g average, at 4°. (SW 55 Ti rotor, 51 300 rpm average, Optima L-XP Beckman Coulter ultracentrifuge). After centrifugation the solution was fractioned. To determine the peak fraction, the ATPase activity of fractions was checked. Peak fraction was aliquoted and fast frozen for storage at -80° C.

Bibliography

[1] C Bustamante, D Keller, and G Oster, *The physics of molecular motors*, Accounts of Chemical Research **34**, 414–420 (2001).

[2] R M Berry, *Theories of rotary motors*, Philosophical Transactions of the Royal Society B **355**, 503–9 (2000).

[3] M Schliwa, editor. **Molecular Motors**, chapter 1: The Myosin Superfamiliy: An Overview. Wiley-VCH, 2003.

[4] J R Sellers and C Viegel, *Walking with myosin V*, Current Opinion in Cell Biology **18**, 68–73 (2006).

[5] D M Warshaw, G G Kennedy, S S Work, E B Krementsova, S Beck, and K M Trybus, *Differential labeling of myosin V heads with quantum dots allows direct visualization of hand-over-hand processivity*, Biophysical Journal **88**, 30–32 (2005).

[6] L S Churchman, Z Okten, R S Rock, J F Dawson, and J.A Spudich, *Single molecule high-resolution colocfalization of Cy3 and Cy5 attached to macromolecules measures intramolecular distance through time*, Proceedings of National Academy of Science U S A **102**, 1419–1423 (2005).

[7] T Sakamoto, A Yildiz, P R Selvin, and J R Seller, *Step size is determined by neck length in myosin V*, Biochemistry **44**, 16210 (2005).

[8] N Volkmann, H Liu, L Hazelwood, E B Krementsova, S Lowey, K M Trybus, and D Hanein, *The structural basis of Myosin V processive movement as relealed by electron cryomicroscopy*, Molecular Cell **19**, 595–605 (2005).

[9] C Veigel, F Wang, M L Bartoo, J R Sellers, and J E Molloy, *The gated gait of the precessive molecular motor myosin V*, Nature Cell Biology **4**, 59–65 (2002).

[10] E M De La Cruz, A L Wells, S S Rosenfeld, E M Ostap, and H L Sweeney, *The kinetic mechanism of myosin V*, Proceedings of National Academy of Science U S A **96**, 13726–13731 (1999).

[11] A E Clemen, M Vilfan, J Jaud, J Zhang, M Barmann, and M Rief, *Force-dependent stepping kinetics of myosin-V*, Biophysical Journal **88**, 4402–4410 (2005).

[12] J E Baker, E B Krementsova, G G Kennedy, A Armstrong, K M Trybus, and D M Warshaw, *Myosin V processivity: multiple kinetic pathways for head-to-head coordination*, Proceedings of National Academy of Science U S A **101**, 5542–5546 (2004).

[13] C Veigel, S Schmitz, F Wang, and J R Sellers, *Load-dependent kinetics of myosin-V can explain its high processivity*, Nature Cell Biology **7**, 861–869 (2005).

[14] M Schliwa, editor. **Molecular Motors**, chapter 2: Dynein Motors: Structure, Mechanochenistry and Regulation. Wiley-VCH, 2003.

[15] S Block, C L Asbury, J W Shaevitz, and M J Lang, *Probing the kinesin reaction cycle with a 2D optical force clamp*, Proceedings of National Academy of Science U S A **100**, 2351–2356 (2003).

[16] K Visscher, M J Schnitzer, and S M Block, *Single kinesin molecules studied with a molecular force clamp*, Nature **400**, 184–189 (1999).

[17] M J Lang, C L Asbury, J W Shaevitz, and S M Block, *An automated two-dimensional optical force clamp for single molecule studies*, Biophysical Jorunal **83**, 491–501 (2002).

[18] R A Cross, *The kinetic mechanism of kinesin*, Trends in Biochemical Sciences **29**, 301–309 (2004).

[19] S P Gilbert and K A Johnson, *Pre-steady-state kinetics of the microtubule-kinesin ATPase*, Biochemistry **33**, 1951–1960 (1994).

[20] Y Z Ma and E W Taylor, *Interacting head mechanism of microtubule-kinesin ATPase*, Journal of Biological Chemistry **272**, 724–730 (1997).

[21] Y Z Ma and E W Taylor, *Kinetic mechanism of a monomeric kinesin construct*, Journal of Biological Chemistry **272**, 717–723 (1997).

[22] S S Rosenfeld, G M Jefferson, and P H King, *ATP reorients the neck linker of kinesin in two sequential steps*, Journal of Biological Chemistry **276**, 40167–40174 (2001).

[23] S Uemura and S Ishiwata, *Loading direction regulates the affinity of ADP for kinesin*, Nature Structural and Molecular Biology **10**, 308–311 (2003).

[24] M J Schnitzer and S M Block, *Kinesin hydrolyses one ATP per 8-nm step*, Nature **388**, 386–390 (1997).

[25] F J Kull and S A Endow, *Kinesin: switch I and II and the motor mechanism*, Journal of Cell Science **115**, 15–23 (2002).

[26] L M Klumpp, A Hoenger, and S P Gilbert, *Kinesin's second step*, Proceedings of National Academy of Science U S A **101**, 3444–3449 (2004).

[27] S S Rosenfeld, P M Fordyce, G M Jefferson, P H King, and S M Block, *Stepping and stretching. How kinesin uses internal strain to walk processively*, Journal of Biological Chemistry **278**, 18550–18556 (2003).

[28] I Crevel, N Carter, M Schliwa, and R Cross, *Coupled chemical and mechanical reaction steps in a processive Neurospora kinesin*, EMBO Journal **18**, 5863–5872 (1999).

[29] K Kaseda, H Higuchi, and K Hirose, *Alternate fast and slow stepping of a heterodimeric kinesin molecule*, Nature Molecular Cell Biology **5**, 1079–1082 (2003).

[30] C L Asbury, A N Fehr, and S M Block, *Kinesin moves by an asymmetric hand-over-hand mechanism*, Science **302**, 2130–2134 (2003).

[31] M Schliwa, editor. **Molecular Motors**, chapter 3: Kinesin Superfamily Proteins. Wiley-VCH, 2003.

[32] Z Wang, S Khan, and M P Sheetz, *Single cytoplasmic dynein molecule movements: characterization and comparison with kinesin*, Biophysical Journal **69**, 2011–2023 (1995).

[33] R D Vale and Y Y Toyoshima, *Rotation and translocation of microtubules in vitro induced by dyneins from tetrahymena cilia*, Cell **52**, 459–469 (1988).

[34] O Kagami and R Kamiya, *Translocation and rotation of microtubules caused by multiple species of Chlamydomonas inner-arm dynein*, Journal of Cell Science **103**, 653–664 (1992).

[35] K Oiwa and H Sakakibara, *Recent progress in dynein structure and mechanism*, Current Opinion in Cell Biology **17**, 98–103 (2005).

[36] S A Burgess, M L Walker, H Sakakibara, P J Knight, and K Oiwa, *Dynein structure and power stroke*, Nature **421**, 715–718 (2003).

[37] S A Burgess, M L Walker, H Sakakibara, K Oiwa, and P J Knight, *The structure of dynein-c by negative stain electron microscopy*, Journal of Structural Biology **146**, 205–216 (2004).

[38] M A Gee, J E Heuser, and R B Vallee, *An extended microtubule-binding structure within the dynein motor domain*, Nature **390**, 636–639 (1997).

[39] N Mizuno, S Toba, M Edamatsu, J Watai-Nishii, N Hirokawa, Y Y Toyoshima, and M Kikkawa, *Dynein and kinesin share an overlapping microtubule-binding site*, EMBO Journal **23**, 2459–2467 (2004).

[40] T Kon, M Nishiura, R Ohkura, Y Y Toyoshima, and K Sutoh, *Distinct functions of nucleotide-binding/hydrolysis sites in the four AAA modules of cytoplasmic dynein*, Biochemistry **43**, 11266–11274 (2004).

[41] A Silvanovich, M G Li, M Serr, S Mische, and T S Hays, *The third P-loop domain in cytoplasmic dynein heavy chain is essential for dynein motor function and ATP-sensitive microtubule binding*, Molecular Biology of the Cell **14**, 1355–1365 (2003).

[42] M Samsó and M P Koonce, *25 Angstrom resolution structure of a cytoplasmic dynein motor reveals a seven-member planar ring*, Journal of Molecular Biology **340**, 1059–1072 (2004).

[43] C Shingyoji, H Higuchi, M Yoshimura, E Katayama, and T Yanagida, *Dynein arms are oscillating force generators*, Nature **393**, 711–714 (1998).

[44] H Sakakibara, H Kojima, Y Sakai, E Katayama, and K Oiwa, *Inner-arm dynein c of Chlamydomonas flagella is a single-headed processive motor*, Nature **400**, 586–590 (1999).

[45] E Hirakawa, H Higuchi, and Y Y Toyoshima, *Processive movement of single 22S dynein molecules occurs only at low ATP concentrations*, Proceedings of National Academy of Science U S A **97**, 2533–2537 (2000).

[46] C B Lindemann and A J Hunt, *Does axonemal dynein push, pull, or oscillate?*, Cell Motility and the Cytoskeleton **56**, 237–244 (2003).

[47] S Toba, T M Watanabe, L Yamaguchi-Okimoto, Y Y Toyoshima, and H Higuchi, *Overlapping hand-over-hand mechanism of single molecular motility of cytoplasmic dynein*, Proceedings of National Academy of Science U S A **103**, 5741–5745 (2006).

[48] M Schliwa, editor. **Molecular Motors**, chapter 6: RNA and DNA Polymerases. Wiley-VCH, 2003.

[49] M D Wang, M J Schnitzer, H Yin, R Landick, J Gelles, and S M Block, *Force and velocity measured for single molecules of rna polymerase*, Science **282**, 902–907 (1998).

[50] H Yin, M D Wang, K Svoboda, R Landick, S M Block, and J Gelles, *Transcription against an applied force.*, Science **270**, 1653–1656 (1995).

[51] G J Wuite, S B Smith, M Young, D Keller, and C Bustamante, *Single-molecule studies of the effect of template tension on T7 DNA polymerase activity*, Nature **404**, 103–106 (2000).

[52] M Schliwa, editor. **Molecular Motors**, chapter 7: Helicases as Molecular Motors. Wiley-VCH, 2003.

[53] M Yoshida, E Muneyuki, and T Hisabori, *ATP synthase-a marvellous rotary engine of the cell*, Nature Molecular Cell Biology **2**, 669–77 (2001).

[54] H Noji, R Yasuda, M Yoshida, and K Jr Kinosita, *Direct observation of the rotation of F1-ATPase*, Nature **386**, 299–302 (1997).

[55] H Kanazawa, K Mabuchi, T Kayano, T Noumi, T Sekiya, and M Futai, *Nucleotide sequence of the genes for F0 components of the proton-translocating ATPase from Escherichia coli: prediction of the primary structure of Fo subunits*, Biochemical and Biophysical Research Communications **103**, 604–612 (1981).

[56] J E Walker, I M Fearnley, N J Gay, B W Gibson, F D Northrop, S J Powell, M J Runswick, M Saraste, and V L Tybulewicz, *Primary structure and subunit stoichiometry of F1-ATPase from bovine mitochondria*, Journal of Molecular Biology **184**, 677–701 (1985).

[57] G S Hudson, J G Mason, T A Holton, B Koller, G B Cox, P R Whitfeld, and W Bottomley, *A gene cluster in the spinach and pea chloroplast genomes encoding one CF1 and three CF0 subunits of the H+-ATP synthase complex and the ribosomal protein S2*, Journal of Molecular Biology **196**, 283–98 (1987).

[58] K Nishio, A Iwamoto-Kihara, A Yamamoto, Y Wada, and M Futai, *Subunit rotation of ATP synthase embedded in membranes: a or beta subunit rotation relative to the c subunit ring*, Proceedings of National Academy of Science U S A **99**, 13448–13452 (2002).

[59] J Xing, J C Liao, and G Oster, *Making ATP*, Proceedings of National Academy of Science U S A **102**, 16539–16546 (2005).

[60] J P Abrahams, A G Leslie, R Lutter, and J E Walker, *Structure at 2.8 A resolution of F1-ATPase from bovine heart mitochondria*, Nature **370**, 621–8 (1994).

[61] R Yasuda, T Masaike, K Adachi, H Noji, H Itoh, and K Kinosita, *The ATP-waiting conformation of rotating F1-ATPase revealed by single-pair fluorescence resonance energy transfer*, Proceedings of National Academy of Science U S A **100**, 9314–9318 (2003).

[62] C Gibbons, M G Montgomery, A G Leslie, and J E Walker, *The structure of the central stalk in bovine F(1)-ATPase at 2.4 A resolution*, Nature Structural Biology **7**, 1055–61 (2000).

[63] R I Menz, J E Walker, and A G Leslie, *Structure of bovine mitochondrial F(1)-ATPase with nucleotide bound to all three catalytic sites: implications for the mechanism of rotary catalysis*, Cell **106**, 331–41 (2001).

[64] R Kagawa, M G Montgomery, K Braig, A G W Leslie, and J E Walker, *The structure of bovine F1-ATPase inhibited by ADP and beryllium fluoride*, EMBO Journal **23**, 2734–44 (2004).

[65] K Braig, R I Menz, M G Montgomery, A G Leslie, and J E Walker, *Structure of bovine mitochondrial F(1)-ATPase inhibited by Mg(2+) ADP and aluminium fluoride*, Structure **8**, 567–73 (2000).

[66] R I Menz, A G Leslie, and J E Walker, *The structure and nucleotide occupancy of bovine mitochondrial F(1)-ATPase are not influenced by crystallisation at high concentrations of nucleotide*, FEBS Letters **494**, 11–4 (2001).

[67] M J van Raaij, J P Abrahams, A G Leslie, and J E Walker, *The structure of bovine F1-ATPase complexed with the antibiotic inhibitor aurovertin B*, Proceedings of the National Academy of Sciences of the U S A **93**, 6913–7 (1996).

[68] J P Abrahams, S K Buchanan, M J Van Raaij, I M Fearnley, A G Leslie, and J E Walker, *The structure of bovine F1-ATPase complexed with the peptide*

antibiotic efrapeptin, Proceedings of the National Academy of Sciences of the U S A **93**, 9420–4 (1996).

[69] E Cabezón, M G Montgomery, A G W Leslie, and J E Walker, *The structure of bovine F1-ATPase in complex with its regulatory protein IF1*, Nature Structural Biology **10**, 744–50 (2003).

[70] J R Gledhill and J E Walker, *Inhibition sites in F1-ATPase from bovine heart mitochondria*, Biochemical Journal **386**, 591–8 (2005).

[71] Y Shirakihara, A G Leslie, J P Abrahams, J E Walker, T Ueda, Y Sekimoto, M Kambara, K Saika, Y Kagawa, and M Yoshida, *The crystal structure of the nucleotide-free alpha 3 beta 3 subcomplex of F1-ATPase from the thermophilic Bacillus PS3 is a symmetric trimer*, Structure **5**, 825–36 (1997).

[72] S Wilkens and R A Capaldi, *Electron microscopic evidence of two stalks linking the F1 and F0 parts of the escherichia coli ATP synthase*, Biochimica et Biophysica Acta **1365**, 93–7 (1998).

[73] R A Capaldi, B Schulenberg, J Murray, and R Aggeler, *Cross-linking and electron microscopy studies of the structure and functioning of the Escherichia coli ATP synthase*, The Journal of Experimental Biology **203**, 29–33 (2000).

[74] S Wilkens, J Zhou, R Nakayama, S D Dunn, and R A Capaldi, *Localization of the delta subunit in the Escherichia coli F(1)F(0)-ATPsynthase by immuno electron microscopy: the delta subunit binds on top of the F(1)*, Journal of Molecular Biology **295**, 387–91 (2000).

[75] A C Hausrath, R A Capaldi, and B W Matthews, *The conformation of the epsilon- and gamma-subunits within the Escherichia coli F(1) ATPase*, Journal of Biological Chemistry **276**, 47227–47232 (2001).

[76] T Meier, P Polzer, K Diederichs, W Welte, and P Dimroth, *Structure of the rotor ring of F-Type Na+-ATPase from ilyobacter tartaricus*, Science **308**, 659–662 (2005).

[77] R J Carbajo, F A Kellas, M J Runswick, M G Montgomery, J E Walker, and D Neuhaus, *Structure of the F1-binding domain of the stator of bovine F1Fo-ATPase and how it binds an alpha-subunit*, Journal of Molecular Biology **351**, 824–38 (2005).

[78] R J Carbajo, J A Silvester, M J Runswick, J E Walker, and D Neuhaus, *Solution structure of subunit F(6) from the peripheral stalk region of ATP synthase from bovine heart mitochondria*, Journal of Molecular Biology **342**, 593–603 (2004).

[79] V K Dickson, J A Silvester, I M Fearnley, A G W Leslie, and J E Walker, *On the structure of the stator of the mitochondrial ATP synthase*, EMBO Journal **25**, 2911–8 (2006).

[80] S Wilkens, S D Dunn, J Chandler, F W Dahlquist, and R A Capaldi, *Solution structure of the N-terminal domain of the delta subunit of the E. coli ATPsynthase*, Nature Structural and Molecular Biology **4**, 198–201 (1997).

[81] O Dmitriev, P C Jones, W Jiang, and R H Fillingame, *Structure of the membrane domain of subunit b of the Escherichia coli F0F1 ATP synthase*, The Journal of Biological Chemistry **274**, 15598–15604 (1999).

[82] P A Del Rizzo, Y Bi, S D Dunn, and B H Shilton, *The "second stalk" of Escherichia coli ATP synthase: structure of the isolated dimerization domain*, Biochemistry **41**, 6875–84 (2002).

[83] J L Rubinstein, J E Walker, and R Henderson, *Structure of the mitochon-*

drial ATP synthase by electron cryomicroscopy, EMBO Journal **22**, 61826192 (2003).

[84] B E Schwem and R H Fillingame, *Cross-linking between helices within subunit a of Escherichia coli ATP synthase defines the transmembrane packing of a four helix bundle*, Journal of Biological Chemistry **281**, 37861–7 (2006).

[85] Y Kato-Yamada, H Noji, R Yasuda, K Kinosita, and M Yoshida, *Direct observation of the rotation of epsilon subunit in F1-ATPase*, Journal of Biological Chemistry **273**, 19375–19377 (1998).

[86] B Zimmermann, M Diez, N Zarrabi, P Gräber, and M Börsch, *Movements of the epsilon-subunit during catalysis and activation in single membrane-bound H(+)-ATP synthase*, EMBO Journal **24**, 2053–2063 (2005).

[87] R Yasuda, H Noji, K Kinosita, and M Yoshida, *F1-ATPase is a highly efficient molecular motor that rotates with discrete 120 degree steps*, Cell **93**, 1117–1124 (1998).

[88] Jeremy M Berg, John L Tymoczko, and Lubert Stryer, **Biochemistry** (W. H. Freeman, 5th edition edition, feb 2002).

[89] K Adachi, R Yasuda, H Noji, H Itoh, Y Harada, M Yoshida, and K Kinosita, *Stepping rotation of F1-ATPase visualized through angle-resolved single-fluorophore imaging*, Proceedings of National Academy of Science U S A **97**, 7243–7247 (2000).

[90] N Sakaki, R Shimo-Kon, K Adachi, H Itoh, S Furuike, E Muneyuki, M Yoshida, and K Kinosita, *One rotary mechanism for F1-ATPase over ATP concentrations from millimolar down to nanomolar*, Biophysical Journal **88**, 2047–2056 (2005).

[91] R Yasuda, H Noji, M Yoshida, K Kinosita, and H Itoh, *Resolution of distinct rotational substeps by submillisecond kinetic analysis of F1-ATPase*, Nature **410**, 898–904 (2001).

[92] K Shimabukuro, R Yasuda, E Muneyuki, K Y Hara, K Kinosita, and M Yoshida, *Catalysis and rotation of F1 motor: cleavage of ATP at the catalytic site occurs in 1 ms before 40 degree substep rotation*, Proceedings of National Academy of Science U S A **100**, 14731–14736 (2003).

[93] T Nishizaka, K Oiwa, H Noji, S Kimura, E Muneyuki, M Yoshida, and K Kinosita, *Chemomechanical coupling in F1-ATPase revealed by simultaneous observation of nucleotide kinetics and rotation*, Nature Structural and Molecular Biology **11**, 142–148 (2004).

[94] K Y Hara, H Noji, D Bald, R Yasuda, K Kinosita, and M Yoshida, *The role of the DELSEED motif of the beta subunit in rotation of F1-ATPase*, Journal of Biological Chemistry **275**, 14260–14263 (2000).

[95] T Ariga, T Masaike, H Noji, and M Yoshida, *Stepping rotation of F(1)-ATPase with one, two, or three altered catalytic sites that bind ATP only slowly*, Journal of Biological Chemistry **277**, 24870–24874 (2002).

[96] H Noji, D Bald, R Yasuda, H Itoh, M Yoshida, and K Kinosita, *Purine but not pyrimidine nucleotides support rotation of F(1)-ATPase*, Journal of Biological Chemistry **276**, 25480–25486 (2001).

[97] G Oster and H Wang, *Reverse engineering a protein: the mechanochemistry of ATP synthase*, Biochimica et Biophysica Acta **1458**, 482–510 (2000).

[98] M D Hossain, S Furuike, Y Maki, K Adachi, M Y Ali, M Huq, H Itoh, M Yoshida, and K Kinosita, *The rotor tip inside a bearing of a thermophilic*

F1-ATPase is dispensable for torque generation, Biophysical Journal **90**, 4195–4203 (2006).

[99] A Iwamoto, J Miki, M Maeda, and M Futai, *H(+)-ATPase gamma subunit of Escherichia coli. Role of the conserved carboxyl-terminal region*, Journal of Biological Chemistry **265**, 5043–8 (1990).

[100] M Sokolov, L Lu, W Tucker, F Gao, P A Gegenheimer, and M L Richter, *The 20 C-terminal amino acid residues of the chloroplast ATP synthase gamma subunit are not essential for activity*, Journal of Biological Chemistry **274**, 13824–13829 (1999).

[101] M Müller, O Pänke, W Junge, and S Engelbrecht, *F1-ATPase, the C-terminal end of subunit gamma is not required for ATP hydrolysis-driven rotation*, The Journal of Biological Chemistry **277**, 23308–23313 (2002).

[102] Y Hirono-Hara, H Noji, M Nishiura, E Muneyuki, K Y Hara, R Yasuda, K Kinosita, and M Yoshida, *Pause and rotation of F(1)-ATPase during catalysis*, Proceedings of National Academy of Science U S A **98**, 13649–13654 (2001).

[103] Y M Milgrom, L L Ehler, and P D Boyer, *ATP binding at noncatalytic sites of soluble chloroplast F1-ATPase is required for expression of the enzyme activity*, Journal of Biological Chemistry **265**, 18725–18728 (1990).

[104] Y M Milgrom, L L Ehler, and P D Boyer, *The characteristics and effect on catalysis of nucleotide binding to noncatalytic sites of chloroplast F1-ATPase*, Journal of Biological Chemistry **266**, 11551–11558 (1991).

[105] J M Jault and W S Allison, *Slow binding of ATP to noncatalytic nucleotide binding sites which accelerates catalysis is responsible for apparent negative cooperativity exhibited by the bovine mitochondrial F1-ATPase*, Journal of Biological Chemistry **268**, 1558–1566 (1993).

[106] D J Hyndman, Y M Milgrom, E A Bramhall, and R L Cross, *Nucleotide-binding sites on Escherichia coli F1-ATPase. specificity of noncatalytic sites and inhibition at catalytic sites by MgADP*, Journal of Biological Chemistry **269**, 28871–28877 (1994).

[107] N Mitome, S Ono, T Suzuki, K Shimabukuro, E Muneyuki, and M Yoshida, *The presence of phosphate at a catalytic site suppresses the formation of the MgADP-inhibited form of F(1)-ATPase*, European Journal of Biochemistry **269**, 53–60 (2002).

[108] Y Hirono-Hara, K Ishizuka, K Kinosita, M Yoshida, and H Noji, *Activation of pausing F1 motor by external force*, Proceedings of National Academy of Science U S A **102**, 4288–4293 (2005).

[109] H Itoh, A Takahashi, K Adachi, H Noji, R Yasuda, M Yoshida, and K Kinosita, *Mechanically driven ATP synthesis by F1-ATPase*, Nature **427**, 465–468 (2004).

[110] Y Rondelez, G Tresset, K V Tabata, H Arata, H Fujita, S Takeuchi, and H Noji, *Microfabricated arrays of femtoliter chambers allow single molecule enzymology*, Nature Biotechnology **23**, 361–365 (2005).

[111] Y Rondelez, G Tresset, T Nakashima, Y Kato-Yamada, H Fujita, S Takeuchi, and H Noji, *Highly coupled ATP synthesis by F1-ATPase single molecules*, Nature **433**, 773–777 (2005).

[112] G Kaim, M Prummer, B Sick, G Zumofen, A Renn, U P Wild, and P Dimroth, *Coupled rotation within single F0F1 enzyme complexes during ATP synthesis or hydrolysis*, FEBS Letters **525**, 156–163 (2002).

[113] M Diez, B Zimmermann, M Börsch, M König, E Schweinberger, S Steigmiller, R Reuter, S Felekyan, V Kudryavtsev, C A Seidel, and P Gräber, *Proton-*

powered subunit rotation in single membrane-bound F0F1-ATP synthase, Nature Structural and Molecular Biology **11**, 135–141 (2004).

[114] M D Wang, H Yin, R Landick, J Gelles, and S M Block, *Stretching DNA with optical tweezers*, Biophysical Journal **72**, 1335–1346 (1997).

[115] T Nishi and M Forgac, *The vacuolar (H+)-ATPases–nature's most versatile proton pumps*, Nature Reviews Molecular Cell Biology **3**, 94–103 (2002).

[116] K W Beyenbach and H Wieczorek, *The V-type H+ ATPase: molecular structure and function, physiological roles and regulation*, Journal of Experimental Biology **209**, 577–89 (2006).

[117] O Drory and N Nelson, *The emerging structure of vacuolar atpases*, Physiology **21**, 317–325 (2006).

[118] P M Kane, *Disassembly and reassembly of the yeast vacuolar H(+)-ATPase in vivo*, Journal of Biological Chemistry **270**, 17025–17032 (1995).

[119] M Lu, Y Y Sautin, L S Holliday, and S L Gluck, *The glycolytic enzyme aldolase mediates assembly, expression, and activity of vacuolar H+-ATPase*, Journal of Biological Chemistry **279**, 8732–8739 (2004).

[120] A M Smardon, M Tarsio, and P M Kane, *The RAVE complex is essential for stable assembly of the yeast V-ATPase*, Journal of Biological Chemistry **277**, 13831–13839 (2002).

[121] T Inoue, Y Wang, K Jefferies, J Qi, A Hinton, and M Forgac, *Structure and regulation of the V-ATPases*, Journal of Bioenergetics and Biomembranes **37**, 393–398 (2005).

[122] Y Y Sautin, M Lu, A Gaugler, L Zhang, and S L Gluck, *Phosphatidylinositol 3-kinase-mediated effects of glucose on vacuolar H+-ATPase assembly,*

translocation, and acidification of intracellular compartments in renal epithelial cells, Molecular Cell Biology **25**, 575–589 (2005).

[123] B Zimmermann, P Dames, B Walz, and O Baumann, *Distribution and serotonin-induced activation of vacuolar-type H+-ATPase in the salivary glands of the blowfly Calliphora vicina*, Journal of Experimental Biology **206**, 1867–1876 (2003).

[124] M Grabe, H Wang, and G Oster, *The mechanochemistry of V-ATPase proton pumps*, Biophysical Journal **78**, 2798–2813 (2000).

[125] T Murata, I Yamato, Y Kakinuma, A G Leslie, and J E Walker, *Structure of the rotor of the V-Type Na+-ATPase from Enterococcus hirae*, Science **308**, 654–659 (2005).

[126] N R Francis, G E Sosinsky, D Thomas, and D J DeRosier, *Isolation, characterization and structure of bacterial flagellar motors containing the switch complex*, Journal of Molecular Biology **235**, 1261–1270 (1994).

[127] H C Berg, *The rotary motor of bacterial flagella*, Annual Review of Biochemistry **72**, 19–54 (2003).

[128] G E Murphy, J R Leadbetter, and G J Jensen, *In situ structure of the complete Treponema primitia flagellar motor*, Nature **442**, 1062–1064 (2006).

[129] R M Berry and J P Armitage, *The Bacterial Flagella Motor*, Advances in Microbial Physiology **41**, 291–337 (1997).

[130] R M Macnab, *How bacteria assemble flagella*, Annual Review of Biochemistry **57**, 77–100 (2003).

[131] T Hirano, S Yamaguchi, K Oosawa, and S I Aizawa, *Roles of FliK and FlhB*

in determination of flagellar hook length in Salamonella typhimurium, Journal of Bacteriology **176**, 5439–49 (1994).

[132] S M Block, D F Blair, and H C Berg, *Compliance of bacterial flagella measured with optical tweezers*, Nature **338**, 514–518 (1989).

[133] S M Block, D F Blair, and H C Berg, *Compliance of bacterial polyhooks measured with optical tweezers*, Cytometry **12**, 492–496 (1991).

[134] C J Jones, R M Macnab, H Okino, and S I Aizawa, *Stoichiometric analysis of the flagellar hook-(basal-body) complex of Salmonella typhimurium*, Journal of Molecular Biology **212**, 377–87 (1990).

[135] M Homma, K Kutsukake, M Hasebe, T Iiono, and R M Macnab, *FlgB, FlgC, FlgF and FlgG. A family of structurally related proteins in the flagellar basal body of Salmonella typhimurium*, Journal of Molecular Biology **211**, 465–77 (1990).

[136] T Ueno, K Oosawa, and S Aizawa, *M ring, S ring and proximal rod of the flagellar basal body of Salmonella typhimurium are composed of subunits of single protein, FliF*, Journal of Molecular Biology **227**, 672–7 (1992).

[137] T Ueno, K Oosawa, and S Aizawa, *Domain structures of the MS ring component protein (FliF) of the flagellar basal body of Salmonella typhimurium*, Journal of Molecular Biology **236**, 546–55 (1994).

[138] S Yamaguchi, S Aizawa, M Kihara, M Isomura, C J Jones, and R M Macnab, *Genetic evidence for a switching and energy-transducing complex in the flagellar motor of Salmonella typhimurium*, Journal of Bacteriology **168**, 1172–9 (1986).

[139] S Yamaguchi, H Fujita, A Ishihara, S Aizawa, and R M Macnab, *Subdivision of*

flagellar genes of Salmonella typhimurium into regions for assembly, rotation and switching, Journal of Bacteriology **166**, 187–93 (1986).

[140] D R Thomas, N R Francis, C Xu, and D J Derosier, *The three-dimensional structure of the flagellar rotor from a clockwise-locked mutant of Salmonella enterica serovar Typhimurium*, Journal of Bacteriology **188**, 7033–5 (2006).

[141] K Oosawa, T Ueno, and S Aizawa, *Overproduction of the bacterial flagellar switch proteins and their interactions with the MS ring complex in vitro*, Journal of Bacteriology **176**, 3683–91 (1994).

[142] D L Marykwas, S A Schmidt, and H C Berg, *Interacting components of the flagellar motor of Escherichia coli revealed by the two-hybrid system in yeast*, Journal of Molecular Biology **256**, 564–76 (1996).

[143] N R Francis, V M Irikura, S Yamaguchi, D J DeRosier, and R M Macnab, *Localization of the Salmonella typhimurium flagellar switch protein FliG to the cytoplasmic M-ring face of the basal body*, Proceedings of National Academy of Science U S A **89**, 6304–8 (1992).

[144] D Thomas, Morgan D G, and D J DeRosier, *Structures of bacterial flagellar motors from two FliF-FliG gene fusion mutants*, Journal of Bacteriology **183**, 6404–12 (2001).

[145] A S Toker and R M Macnab, *Distinct regions of bacterial flagellar switch protein FliM interact with Fli, FliN and CheY*, Journal of Molecular Biology **273**, 623–34 (1997).

[146] H Tang, T F Braun, and D F Blair, *Motility protein complexes in the bacterial flagellar motor*, Journal of Molecular Biology **261**, 209–21 (1996).

[147] M Welch, K Oosawa, S Aizawa, and M Eisenbach, *Phosphorylation-dependent*

binding of a single molecule to the flagellar switch of bacteria, Proceedings of National Academy of Science U S A **90**, 8787–91 (1993).

[148] M Welch, K Oosawa, S I Aizawa, and M Eisenbach, *Effects of phosphorylation, Mg2+, and conformation of the chemotaxis CheY on its binding to the flagellar switch protein FliM*, Biochemistry **33**, 10470–6 (994).

[149] A Bren and M Eisenbach, *The N terminus of the flagellar switch protein, FliM, is the binding domain for the chemotactic response regulator, CheY*, Journal of Molecular Biology **278**, 507–14 (1998).

[150] K Sato and M Homma, *Multimeric structure of PomA, a component of the Na+-driven polar flagellar motor of vibrio alginolyticus*, Journal of Biological Chemistry **275**, 20223–8 (2000).

[151] T Yorimitsu, M Kojima, T Yakushi, and M Homma, *Multimeric structure of the PomA/PomB channel complex in the Na+-driven flagellar motor of Vibrio alginolyticus*, Journal of Biochemistry (Tokyo) **135**, 43–51 (2004).

[152] D F Blair and H C Berg, *Mutations in the MotA protein of Escherichia coli reveal domains critical for proton conduction*, Journal of Molecular Biology **173**, 4049–55 (1991).

[153] J Zhou, R T Fazzio, and D F Blair, *Membrane topology of the MotA protein of escherichia coli*, Journal of Molecular Biology **251**, 237–42 (1995).

[154] S Y Chun and J S Parkinson, *Bacterial motility: membrane topology of the Escherichia coli MotB protein*, Science **239**, 276–8 (1988).

[155] R de Mot and J Vanderleyden, *A conserved surface-exposed domain in major outer membrane proteins of pathogenic pseudomonas and branhamella species shares sequence homology with the calcium-binding repeats of the eukaryotic*

extracellular matrix protein thrombospondin, Molecular Microbiology **13**, 379–80 (1994).

[156] J Zhou, L L Sharp, H L Tang, S A Lloyd, S Billings, T F Braun, and D F Blair, *Function of protonatable residues in the flagellar motor of Escherichia coli: a critical role for Asp32 of MotB*, Journal of Bacteriology **180**, 2729–35 (1998).

[157] D C Fung and H C Berg, *Powering the flagellar motor of Escherichia coli with an external voltage source*, Nature **375**, 809–812 (1995).

[158] C V Gabel and H C Berg, *The speed of the flagellar rotary motor of Escherichia coli varies linearly with protonmotive force*, Proceedings of National Academy of Science U S A **100**, 8748–8751 (2003).

[159] M D Manson, P Tedesco, H C Berg, F M Harold, and C Van der Drift, *A protonmotive force drives bacterial flagella*, Proceedings of National Academy of Science U S A **74**, 3060–3064 (1977).

[160] M D Manson, P M Tedesco, and H C Berg, *Energetics of flagellar rotation in bacteria*, Journal of Molecular Biology **138**, 541–561 (1980).

[161] Y Sowa, H Hotta, M Homma, and A Ishijima, *Torque-speed relationship of the Na+-driven flagellar motor of Vibrio alginolyticus*, Journal of Molecular Biology **327**, 1043–1051 (2003).

[162] C J Lo, M C Leake, Pilizota T, and R M Berry, *Nonequivalence of membrane voltage and ion-gradient as driving forces for the bacterial flagellar motor at low load*, Biophysical Jorunal **93**, 294–302 (2007).

[163] C J Lo, M C Leake, and R M Berry, *Fluorescence measurement of intracellular sodium concentration in single Escherichia coli cells*, Biophysical Journal **90**, 357–365 (2006).

[164] Y Sowa, A D Rowe, M C Leake, T Yakushi, M Homma, A Ishijima, and R M Berry, *Direct observation of steps in rotation of the bacterial flagellar motor*, Nature **437**, 916–919 (2005).

[165] Y Asai, T Yakushi, I Kawagishi, and M Homma, *Ion-coupling determinants of Na+-driven and H+-driven flagellar motors*, Journal of Molecular Biology **327**, 453–463 (2003).

[166] M Meister, G Lowe, and H C Berg, *The proton flux through the bacterial flagellar motor*, Cell **49**, 643–650 (1987).

[167] J B Armstrong and J Adler, *Complementation of nonchemotactic mutants of Escherichia coli*, Genetics **61**, 61–66 (1969).

[168] M Silverman, P Matsumura, and M Simon, *The identification of the mot gene product with Escherichia coli-lambda hybrids*, Proceedings of National Academy of Science U S A **73**, 3126–3130 (1976).

[169] S M Block and H C Berg, *Successive incorporation of force-generating units in the bacterial rotary motor*, Nature **309**, 470–472 (1984).

[170] D F Blair and H C Berg, *Restoration of torque in defective flagellar motors*, Science **242**, 1678–1681 (1988).

[171] S W Reid, M C Leake, J H Chandler, C J Lo, J P Armitage, and R M Berry, *The maximum number of torque-generating units in the flagellar motor of Escherichia coli is at least 11*, Proceedings of National Academy of Science U S A **103**, 8066–8071 (2006).

[172] M C Leake, J H Chandler, G H Wadhams, F Bai, R M Berry, and J P Armitage, *Stoichiometry and turnover in single, functioning membrane protein complexes*, Nature **443**, 355–358 (2006).

[173] W S Ryu, R M Berry, and H C Berg, *Torque-generating units of the flagellar motor of Escherichia coli have a high duty ratio*, Nature **403**, 444–447 (2000).

[174] X Chen and H C Berg, *Torque-speed relationship of the flagellar rotary motor of Escherichia coli*, Biophysical Journal **78**, 1036–1041 (2000).

[175] R M Berry and H C Berg, *Torque generated by the flagellar motor of Escherichia coli while driven backward*, Biophysical Journal **76**, 580–7 (1999).

[176] H C Berg and L Turner, *Torque generated by the flagellar motor of Escherichia coli*, Biophysical Journal **65**, 2201–221 (1993).

[177] R M Berry, L Turner, and H C Berg, *Mechanical limits of bacterial flagellar motors probed by electrorotation*, Biophysical Journal **69**, 280–6 (1995).

[178] R M Berry and H C Berg, *Absence of a barrier to backwards rotation of the bacterial flagellar motor demonstrated with optical tweezers*, Proceedings of National Academy of Science U S A **94**, 14433–14437 (1997).

[179] T Pilizota, T Bilyard, F Bai, H Hosokawa, M Futai, and R M Berry, *A programmable optical angle clamp for rotary molecular motors*, Biophysical Journal **93**, 264–75 (2007).

[180] A D Samuel and H C Berg, *Fluctuation analysis of rotational speeds of the bacterial flagellar motor*, Proceedings of National Academy of Science U S A **92**, 3502–3506 (1995).

[181] A D Samuel and H C Berg, *Torque-generating units of the bacterial flagellar motor step independently*, Biophysical Journal **71**, 918–923 (1996).

[182] S M Block, J E Segall, and H C Berg, *Adaptation kinetics in bacterial chemotaxis*, Journal of Bacteriology **154**, 312–323 (1983).

[183] S Kudo, Y Magariyama, and S Aizawa, *Abrupt changes in flagellar rotation observed by laser dark-field microscopy*, Nature **346**, 677–80 (1990).

[184] B E Scharf, K A Fahrner, L Turner, and H C Berg, *Control of direction of flagellar rotation in bacterial chemotaxis*, Proceedings of National Academy of Science U S A **95**, 201–206 (1998).

[185] U Alon, L Camarena, M G Suretter, B Aguera y Arcas, Y Liu, S Leibler, and JB Stock, *Response regulator output in bacterial chemotaxis*, EMBO Journal **17**, 4238–48 (1998).

[186] P Cluzel, M Surette, and S Leibler, *An ultrasensitive bacterial motor revealed by monitoring signaling proteins in single cells*, Science **287**, 1652–1655 (2000).

[187] M Eisenbach, A Wolf, M Welch, S R Caplan, I R Lapidus, R M Macnab, H Aloni, and O Asher, *Pausing, switching and speed fluctuation of the bacterial flagellar motor and their relation to motility and chemotaxis*, Journal of Molecular Biology **211**, 551–63 (1990).

[188] T A Duke, N Le Novère, and D Bray, *Conformational spread in a ring of proteins: a stochastic approach to allostery*, Journal of Molecular Biology **308**, 541–553 (2001).

[189] D Bray and Duke T, *Conformational spread: The propagation of allosteric states in large multiprotein complexes*, Annual Review of Biophysics and Biomolecular Structure **33**, 53–73 (2004).

[190] E Korobkova, T Emonet, J M G Vilar, T S Shimizu, and P Cluzel, *From molecular noise to behavioural variability in a single bacterium*, Nature **428**, 574–8 (2004).

[191] E A Korobkova, T Emonet, H Park, and P Cluzel, *Hidden stochastic nature*

of a single bacterial motor, Physical Review Letters **96**, 058105(1)–058105(4) (2006).

[192] F Xing, Jand Bai, R Berry, and G Oster, *Torque-speed relationship of the bacterial flagellar motor*, Proceedings of the National Academy of Sciences of the U S A **103**, 1260–1265 (2006).

[193] A J Turberfield, J C Mitchell, B Yurke, A P Mills, M I Blakey, and F C Simmel, *DNA fuel for free-running nanomachines*, Physical Review Letters **90**, 118102–118102 (2003).

[194] J Bath, S J Gree, and A J Turberfield, *A free-running DNA motor powered by a nicking enzyme*, Angewandte Chemie International Edition **44**, 4358–4361 (2005).

[195] F Cozzi, A Guenzi, C A Johnson, K Mislow, Hounshell, and J F Blount, *Stereoisomerism and correlated rotation in molecular gear systems. Residual diastereomers of bis(2,3-dimethyl-9-triptycyl)methane*, Journal of the American Chemical **103**, 957–958 (1981).

[196] J Clayden and J H Pink, *Concerted rotation in a tertiary aromatic amide: To wards a simple molecular gear*, Angewandte Chemie International Edition **37**, 1937–1939 (1998).

[197] T C Bedard and J S Moore, *Design and synthesis of a 'molecular turnstile'*, Journal of the American Chemical Society **117**, 10662–10671 (1995).

[198] C A Schalley, K Beizai, and F Vogtle, *On the way to rotaxane-based molecular motors: Studies in molecular mobility and topological chirality*, Accounts of Chemical Research **34**, 465 – 476 (2001).

[199] A R Pease, J O Jeppesen, J F Stoddart, Y Luo, C P Collier, and J R Heath,

Switching devices based on interlocked molecules, Accounts of Chemical Research **34**, 433–444 (2001).

[200] A Ashkin, *Acceleration and trapping of particles by radiation pressure*, Physical Review Letters **24**, 156–159 (1970).

[201] A Ashkin and J M Dziedzic, *Optical levitation by radiation pressure*, Applied Physics Letters **19**, 283–285 (1971).

[202] A Ashkin, J M Dziedzic, J E Bjorkholm, and S Chu, *Observation of a single-beam gradient force optical trap for dielectric particles*, Optics Letters **11**, 288–290 (1986).

[203] A Ashkin, *History of optical trapping and manipulation of small-neutral particle, atoms, and molecules*, IEEE Journal on Selected Topics in Quantum Electronics **6**, 841–856 (2000).

[204] S Chu, J E Bjorkholm, A Ashkin, and A Cable, *Experimental observation of optically trapped atoms*, Physical Review Letters **57**, 314 – 317 (1986).

[205] A Ashkin, JM Dziedzic, and T Yamane, *Optical trapping and manipulation of single cells using infrared laser beams*, Nature **330**, 769 – 771 (1987).

[206] A Ashkin and J M Dziedzic, *Optical trapping and manipulation of viruses and bacteria*, Science **235**, 1517 – 1520 (1987).

[207] K Svoboda and SM Block, *Biological applications of optical forces*, Annual Review of Biophysics and Biomolecular Structure **23**, 247–85 (1994).

[208] A D Mehta, *Single-molecule biomechanics with optical methods*, Science **283**, 1689–1695 (1999).

[209] K C Neuman and S M Block, *Optical trapping*, Review of Scientific Instruments **75**, 2787–2809 (2004).

[210] J E Molloy and M J Padgett, *Lights, action: optical tweezers*, Contemporary Physics **43**, 241–258(18) (2002).

[211] T A Nieminen, H Rubinsztein-Dunlop, and N R Heckenberg, *Calculation and optical measurement of laser trapping forces on non-spherical particles*, Journal of Quantitative Spectroscopy and Radiative Transfer **70**, 627–637 (2001).

[212] J D Jacskon, **Classical Electrodynamics** (John Wiley and Sons, 1998).

[213] J P Barton and D R Alexander, *Fifth-order corrected electromagnetic field components for a fundamental Gaussian beam*, Journal of Applied Physics **66**, 2800–2802 (2006).

[214] A Doicu and T Wriedt, *Plane wave spectrum of electromagnetic beams*, Optics Communications **136**, 114–124(11) (1997).

[215] C F Bohren and D R Huffman, **Absorption and Scattering of Light by Small Particles** (John Wiley, 1998).

[216] K F Ren, G Gouesbet, and G Grehan, *Integral localized approximation in generalized Lorentz-Mie theory*, Applied Optics **37**, 4218–4225 (1998).

[217] M I Mishchenko and L D Travis, *Capabilities and limitations of a current FORTRAN implementation of the T-matrix method for randomly oriented, rotationally symmetric scatterers-computational methods*, Journal of Quantitative Spectroscopy and Radiative Transfer **60**, 309–324(16) (1998).

[218] M I Mishchenko, L D Travis, and A Macke, **T-matrix method and its applications** (Academic Press, 2000).

[219] C Rockstuhl and H P Herzig, *Rigorous diffraction theory applied to the analysis of the optical force on elliptical nano- and micro-cylinders*, Journal of Optics A Pure and Applied Optics **6**, 921–931 (2004).

[220] J L Volakis, A Chatterjee, and L C Kempel, **Finite Element Method Electromagnetics: Antennas, Microwave Circuits, and Scattering Applications** (Wiley-IEEE Press, 1998).

[221] D A White, *Numerical modeling of optical gradient traps using the vector finite element method*, Journal of Computational Physics **159**, 13–37(25) (2000).

[222] A Taflove and S C Hagness, **Computational electrodynamics: the finite-difference time-domain method** (Artech House, 2000).

[223] A G Hoekstra, M Frijlink, L Waters, and P M A Sloot, *Radiation forces in the discrete-dipole approximation*, Journal of the Optical Society of America A **18**, 1944–53 (2001).

[224] K Visscher, G J Brakenhoff, and J J Krol, *Micromanipulation by multiple optical traps created by a single fast scanning trap integrated with the bilateral confocal scanning laser microscope*, Cytometry **14**, 105 – 114 (1993).

[225] J E Molloy, J E Burns, J C Sparrow, R T Tregear, J Kendrick-Jones, and D C S White, *Single-molecule mechanics of heavy meromyosin and S1 interacting with rabbit or Drosophila actins using optical tweezers*, Biophysical Journal **68**, 298S305S (1995).

[226] H M Warrick, R M Simmons, J T Finer, T Q Uyeda, S Chu, and J A Spudich, *In vitro methods for measuring force and velocity of the actin-myosin interaction using purified proteins*, Methods in Cell Biology **39**, 1–21 (1993).

[227] M Reicherter, T Haist, E U Wagemann, and H J Tiziani, *Optical particle trapping with computer-generated holograms written on a liquid-crystal display*, Optics Letters **24**, 608–610 (1999).

[228] T A Nieminen, N R Heckenberg, and H Rubinsztein-Dunlop, *Optical measurement of microscopic torques*, Journal of Modern Optics **48**, 405–413 (2001).

[229] M E J Friese, T A Nieminen, N R Heckenberg, and H Rubinsztein-Dunlop, *Optical alignment and spinning of laser-trapped microscopic particles*, Nature **394**, 348–350 (1998).

[230] E Higurashi, R Sawada, and T Ito, *Optically induced angular alignment of trapped birefringent micro-objects by linearly polarized light*, Physical Review E **59**, 3676–3681 (1999).

[231] W Singer, T A Nieminen, U J Gibson, N R Heckenberg, and H Rubinsztein-Dunlop, *Orientation of optically trapped nonspherical birefringent particles*, Physical Review E **73**, 021911(1)–021911(5) (2006).

[232] A I Bishop, T A Nieminen, N R Heckenberg, and H Rubinsztein-Dunlop, *Optical microrheology using rotating laser-trapped particles*, Physical Review Letters **92**, 198104(1)–198104(4) (2004).

[233] A L Porta and M Wang, *Optical torque wrench: Angular trapping, rotation and torque detection of quartz microparticles*, Physical Review Letters **92**, 190801(1)–190801(4) (2004).

[234] A I Bishop, T A Nieminen, and N R Heckenberg, *Optical application and measurement of torque on microparticles of isotropic nonabsorbing material*, Physical Review A **68**, 033802(1)–033802(8) (2003).

[235] S Bayoudh, T A Nieminen, and N R Heckenberg, *Orientation of biological cells using plane-polarized Gaussina beam optical tweezers*, Journal of Modern Optics **50**, 1581–1590 (2003).

[236] R C Gauthier, M Ashman, and C P Grover, *Experimental confirmation of the optical-trapping properties of cylindrical objects*, Applied Optics **38**, 4861–4869 (1999).

[237] A I Bishop, T A Nieminen, N R Heckenberg, and H Rubinsztein-Dunlop, *Optical application and measurement of torque on microparticles of isotropic nonabsorbing material*, Physical Review A **68**, 033802(1)–033802(8) (2003).

[238] H Rubinsztein-Dunlop, T A Nieminen, M E J Friese, and N R Heckenberg, *Optical trapping of absorbing particles*, Advances in Quantum Chemistry **30**, 469–492 (1998).

[239] M E J Friese, J Enger, H Rubinsztein-Dunlop, and N R Heckenberg, *Optical angular-momentum transfer of trapped absorbing particles*, Physical Review A pages 1593–1596 (1996).

[240] M E J. Friese, J Enger, H Rubinsztein-Dunlop, and N R Heckenberg, *Optical angular-momentum transfer to trapped absorbing particles*, Physical Review A **54**, 1593–1596 (1996).

[241] H He, M E J Friese, N R Heckenberg, and H Rubinsztein-Dunlop, *Direct observation of transfer of angular momentum to absorptive particles from a laser beam with a phase singularity*, Physical Review Letters **75**, 826–829 (1995).

[242] H He, N R Heckenberg, and H Rubinsztein-Dunlop, *Optical particle trapping with higher-order doughnut beams produced using high efficiency computer generated holograms*, Journal of Modern Optics **42**, 217–223(7) (1995).

[243] H Rubinsztein-Dunlop, T A Nieminen, M E J Friese, and N R Heckenberg, *Optical trapping of absorbing particles*, Advances in Quantum Chemistry **30**, 469–492 (2003).

[244] L Paterson, M P MacDonald, J Arlt, W Sibbett, P E Bryant, and K Dholakia, *Controlled rotation of optically trapped microscopic particles*, Science **292**, 912–914 (2001).

[245] S Sato, M Ishigure, and H Inaba, *Optical trapping and rotational manipulation of microscopic particles and biological cells using higher-order mode Nd:YAG laser beams*, Electronics Letters **27**, 1831–1832 (1991).

[246] E Santamato, A Sasso, B Piccirillo, and A Vella, *Optical angular momentum transfer to transparent isotropic particles using laser beam carrying zero average angular momentum*, Optics Express. **10**, 871–878 (2002).

[247] A T O'Neil and M J Padgett, *Rotational control within optical tweezers by use of rotating aperture*, Optics Letters **27**, 743–745 (2002).

[248] P Galajda and P Ormos, *Complex micromachines produced and driven by light*, Applied Physics Letters **78**, 249–252 (2001).

[249] M Nakanishi-Matsui, S Kashiwagi, H Hosokawa, D J Cipriano, S D Dunn, Y Wada, and M Futai, *Stochastic high-speed rotation of Escherichia coli ATP synthase F1 sector: the epsilon subunit-sensitive rotation*, Journal of Biological Chemistry **281**, 4126–4131 (2006).

[250] D Spetzler, J York, D Daniel, R Fromme, D Lowry, and W Frasch, *Microsecond time scale rotation measurements of single F1-ATPase molecules*, Biochemistry **45**, 3117–3124 (2006).

[251] K Berg-Sorensen and L Oddershede, *Unintended filtering in a typical photodiode detection system for optical tweezers*, Journal of Applied Physics **93**, 3167–3176 (2003).

[252] K C Neuman, E H Chadd, G F Liou, K Bergman, and S M Block, *Charactericationof photodamage to E. coli in optical traps*, Biophysical Journal **77**, 2856–2863 (1999).

[253] E J Peterman, G A van Dijk Meindert, L C Kapitein, and C F Schmidt, *Extending the bandwidth of optical-tweezers interferometry*, Review of Scientific Instruments **74**, 3246–3249 (2003).

[254] H Omote, N Sambonmatsu, K Saito, Y Sambongi, A Iwamoto-Kihara, Y Yanagida, Y Wada, and M Futai, *The gamma-subunit rotation and torque generation in F1-ATPase from wild-type or uncoupled mutant Escherichia coli*, Proceedings of National Academy of Science U S A **96**, 7780–7784 (1999).

[255] Y Iko, Y Sambongi, M Tanabe, A Iwamoto-Kihara, K Saito, I Ueda, Y Wada, and M Futai, *ATP synthase F1 sector rotation*, Journal of Biological Chemistry **276**, 47508–47511 (2001).

[256] M M Bradford, *A rapid and sensitive method for the quantitation of microgram quantities of protein utilizing the principle of protein-dye binding*, Analytical Biochemistry **72**, 248–54 (1976).

[257] O H Lowry, N J Rosebrough, A L Farr, and R J Randall, *Protein measurement with the Folin phenol reagent*, Journal of Biological Chemistry **193**, 265–275 (1951).

[258] JB Sumner, *A method for the colorimetric determination of phosphorus*, Science **100**, 413–414 (1944).

[259] U Piran and W J Riordan, *Dissociation rate constant of the biotin-streptavidin complex*, Journal of Immunological Methods **133**, 141–3 (1990).

[260] H C Berg and L Turner, *Torque generated by the flagellar motor of Escherichia coli*, Biophysical Journal **65**, 2201–2216 (1993).

[261] J Bechhoefer, *Feedback for physicists: A tutorial essay on control*, Reviews of Modern Physics **77**, 783–836 (2005).

[262] K B Sorensen and H Flyvbjerg, *Power spectrum analysis for optical tweezers*, Review of Scientific Instruments **75**, 594–612 (2004).

[263] C Gosse and V Croquette, *Magnetic tweezers: micromanipulation and force measurement at the molecular level*, Biophysical Journal **82**, 3314–3329 (2002).

[264] K B Sorensen and H Flyvbjerg, *Power spectrum analysis for optical tweezers*, Review of Scientific Instruments **75**, 594–612 (2004).

[265] I Tolic-Norrleykke, K Berg-Sorensen, and H Flyvbjerg, *MatLab program for precision calibration of optical tweezers*, Computer Physics Communications **159**, 225–240 (2004).

[266] A Rohrbach, *Stiffness of optical traps: Quantitative agreement between experiment and electromagnetic theory*, Physical Review Letters **95**, 168102(1)–168102(4) (2005).

[267] R M Berry and H C Berg, *Torque generated by the bacterial flagellar motor close to stall*, Biophysical Journal **71**, 3501–3510 (1996).

[268] A D Rowe, **Rotation of a sodium driven flagellar motor**, D.Phil thesis, Univeristy of Oxford, Parks Road, OX1 3PU, 2005.

[269] RC Gauthier, *Theoretical investigation of the optical trapping force and torque on cylindrical micro-objects*, Journal of the Optical Society of America B **14**, 3323–3333 (1997).

[270] C Rockstuhl and H P Herzig, *Calculation of the torque on dielectric elliptical cylinders*, Journal of the Optical Society of America A **22**, 109–116 (2005).

[271] S Lata, A Reichel, R Brock, R Tampé, and J Piehler, *High-affinity adaptors for switchable recognition of histidine-tagged proteins*, Journal of the American Chemical Society **127**, 10205–10215 (2005).

[272] S Lata and J Piehler, *Stable and functional immobilization of histidine-tagged proteins via multivalent chelator headgroups on a molecular poly(ethylene glycol) brush*, Analytical Chemistry **77**, 1096–1105 (2005).

[273] J Malo, J C Mitchell, C Vénien-Bryan, J R Harris, H Wille, D J Sherratt, and A J Turberfield, *Engineering a 2D protein-DNA crystal*, Angewandte Chemie International Edition **44**, 3057–3061 (2005).

[274] J Malo, **DNA scaffolding: a method for protein structure determination**, D.Phil thesis, Univeristy of Oxford, Parks Road, OX1 3PU, 2005.

[275] A Iwamoto, H Omote, H Hanada, N Tomioka, A Itai, M Maeda, and M Futai, *Mutations in Ser174 and the glycine-rich sequence (Gly149, Gly150, and Thr 156) in the beta subunit of Escherichia coli H+-ATPase*, Journal of Biological Chemistry **266**, 6350–16355 (1991).